Exciton Dynamics in Halide Perovskite Nanocrystals: Absorption, Auger Recombination, and Energy Transfer

Andreas Singldinger

München, 2025

Exzitondynamik in Halid Perowskit Nanokristallen:

Absorption, Auger Rekombination und Energietransfer

Dissertation

zur Erlangung des Doktorgrades der Naturwissenschaften (Dr. rer. nat.)

an der Fakultät für Physik

der Ludwig-Maximilians-Universität München

vorgelegt von

Andreas Singldinger

aus Tettnang

München, 15. Oktober 2025

Promotionskommission
Erstgutachter: Prof. Dr. Alexander Urban
Zweitgutachter: Prof. Dr. Achim Hartschuh
Vorsitzender: Prof. Dr. Jörg Schreiber
Beisitzer: Prof. Dr. David Egger
Tag der mündlichen Prüfung: 28. November 2025

dedicated to my family

Publications and Conferences

Scientific Publications of Results Presented in This Work

*** denotes equal contribution**

- M. G. Greiner*, A. Singldinger*, N. A. Henke, C. Lampe, U. Leo, M. Gramlich, A. S. Urban
  Energy Transfer in Stability-Optimized Perovskite Nanocrystals
  Nano Letters 22(16): 6709-6715 (2022)

- A. Singldinger, P. Haußmann, G. Debuisschert, N. A. Henke, J. Paul, L. Luber, P. Ganswindt, A. Abfalterer, A. S. Urban
  Design Rules for Perovskite Nanocrystals: Volume-Governed Absorption Versus Shape-Controlled Auger Recombination
  Advanced Optical Materials 2501137 (2025)

- I. Amersdorffer*, A. Singldinger*, N. A. Henke, A. Abfalterer, P. Ganswindt, U. Leo, T. Hümmer, J. Noé, A. S. Urban
  Towards Correlated Single-Particle Absorption and Photoluminescence Spectroscopy of Perovskite Nanocrystals
  in preparation (2025)

Additional Publications

- A. Singldinger, M. Gramlich, C. Gruber, C. Lampe, A. S. Urban
  Nonradiative energy transfer between thickness-controlled halide perovskite nanoplatelets
  ACS Energy Letters 5(5): 1380-1385 (2020)

- M. F. Lichtenegger, J. Drewniok, A. Bornschlegl, C. Lampe, A. Singldinger, N. A. Henke, A. S. Urban
  Electron–Hole Binding Governs Carrier Transport in Halide Perovskite Nanocrystal Thin Films
  ACS Nano 16(4): 6317-6324 (2022)

- P. Ganswindt, I. Tepfenhart, A. Singldinger, A. Abfalterer, L. Spies, E. Kostyurina, B. Nickel, A. S. Urban
  Locking in Color: Stable RGB Perovskite Nanocrystal Films via UV Cross-Linking
  Advanced Optical Materials 2500166 (2025)

- C. G. Gruber*, A. Mancini*, N. A. Henke, C. Lampe, O. Henrotte, M. F. Lichtenegger, F. Gröbmeyer, A. Singldinger, Y. Li, S. A. Maier, A. S. Urban, E. Cortés
  Sizing Up Light-Emitting Nanocrystals
  submitted to **Nature Materials** (2025)

Contributions to Conferences and Workshops

- *9th International SolTech Conference* (Talk)
  Munich/Online, Germany, October 2020

- *11th International Conference on Quantum Dots (QD2020)* (Poster)
  Munich/Online, Germany, December 2020

- *MRS Spring Meeting* (Talk)
  Seattle/Online, USA, April 2021
- *2nd International e-conversion Conference* (Poster)
  Venice, Italy, October 2022
- *MRS Spring Meeting* (Talk)
  Hawai'i, USA, May 2022
- *11th International SolTech Conference* (Poster)
  Munich, Germany, October 2022

Zusammenfassung

Um Bleihalogenid-Perowskit-Nanokristalle effizient in optoelektronische Bauteile zu integrieren, ist ein tiefes Verständnis darüber erforderlich, wie ihre optischen Eigenschaften durch Form und Umgebung beeinflusst werden. Diese Arbeit nähert sich dieser Fragestellung aus drei unterschiedlichen, aber komplementären Perspektiven: der Untersuchung von Ensembles, der gezielten Analyse einzelner Nanokristalle und der Bestimmung der Eigenschaften von verkapselten Nanokristallen.

Im ersten Teil wird anhand von transienter Absorptionsspektroskopie untersucht, welchen Einfluss Form und Größe auf zentrale Eigenschaften wie den Absorptionsquerschnitt und die Exzitondynamik von $CsPbBr_3$-Nanokristallen haben. Es zeigt sich ein universelles Skalierungsverhalten des Absorptionsquerschnitts in Abhängigkeit vom Volumen, wobei die Kristallform keinen Einfluss nimmt. Auch die Auger-Rekombination von Biexzitonen folgt einem linearen Trend aber nur innerhalb der starken Quanteneinschränkung der Nanokristalle. In schwach quanteneingeschränkten Nanokristallen zeigt sich eine Sättigung, die vor allem von der am stärksten eingeschränkten Dimension der Nanokristalle bestimmt wird.

Der zweite Teil stellt eine neue Methodik zur Untersuchung einzelner Nanokristalle vor, bei der die Absorption ortsaufgelöst an wenigen Kristallen detektiert werden kann. Durch gezielte Probenpräparation und die Kombination von Raster- und Transmissionselektronenmikroskopie lässt sich mithilfe ultrasensitiver Extinktionsspektroskopie der Absorptionsquerschnitt einzelner Nanokristalle direkt bestimmen. Dieser stimmt mit den Werten überein, die zuvor indirekt in Ensemble-Messungen ermittelt wurden. Das unterstreicht das Potenzial der neuen Methodik und markiert einen ersten Schritt zu ihrer Etablierung sowie zu zukünftigen Tieftemperatur-Absorptionsmessungen, mit denen sich beispielsweise die Feinstruktur des Exzitonspektrums einzelner Kristalle auflösen lässt.

Im dritten Teil wird untersucht, wie sich die Stabilität und die Fähigkeit zur Energieaufnahme von $MAPbBr_3$-Nanokristallen durch Verkapselung in Polymermizellen mit variabler Dicke gezielt steuern lassen. Dickere Hüllen erhöhen die Langzeitstabilität signifikant, während gleichzeitig die Effizienz der Energieübertragung über FRET zu den verkapselten Kristallen abnimmt. Eine Balance zwischen Schutz und Funktionalität zu finden ist zentral für den Einsatz in realen Bauteilen. Belastungstests unter Temperatur und UV-Licht geben zudem Einblicke in relevante Nanokristall-Degradierungssmechanismen.

Insgesamt zeigt diese Arbeit, wie strukturelle Kontrolle und neue Messmethoden benutzt werden können, um sowohl grundlegende Einsichten in das Verhalten von Exzitonen zu gewinnen als auch konkrete Designrichtlinien für stabile, leistungsfähige Nanokristall-basierte Bauelemente abzuleiten.

Abstract

Advancing the integration of lead halide perovskite nanocrystals into optoelectronic devices requires a detailed understanding of how structural parameters and the local environment affect their fundamental optical properties. This thesis contributes to that goal through three interconnected studies focusing on ensemble absorption and exciton behavior, single-particle characterization, and device-relevant encapsulation.

First, transient absorption spectroscopy (TAS) is used to investigate how shape and size influence the absorption cross-section and exciton dynamics in $CsPbBr_3$ nanocrystal dispersions. A universal volume-scaling law for the absorption cross-section is established, independent of nanocrystal shape. Alongside this, the biexciton Auger lifetime also follows a volume-scaling behavior, with saturation observed in the weak confinement regime. This saturation depends predominantly on the most confined dimension and is, therefore, different for different nanocrystal shapes.

Second, cavity-enhanced extinction spectroscopy (CEES) is introduced as a novel technique to quantify absorption not via ensemble measurements but at the single-nanocrystal level. A specialized sample preparation method, combined with subsequent scanning electron and atomic force microscopy correlation, allows CEES to bridge ensemble and single-particle absorption studies without relying on photoluminescence. The extracted absorption cross-section matches TAS-derived values, confirming both the approach and its potential. The approach holds promise for future cryogenic studies of excitonic fine structure.

Third, the influence of polymer encapsulation on nanocrystal stability and energy transfer is examined using $MAPbBr_3$ nanocrystals in micellar shells of tunable thickness. Shell thickness is used to simultaneously tune FRET efficiency and environmental stability. Thicker shells improve long-term stability but reduce energy transfer efficiency, highlighting a trade-off between protection and performance. Temperature tests and irradiation with ultraviolet light further reveal the distinct degradation pathways relevant to real-world applications.

Overall, this work demonstrates how morphological control and tailored measurement strategies can be leveraged to guide the design of nanocrystals for specific optoelectronic applications. The presented results and techniques contribute to a deeper understanding of exciton behavior and demonstrate how advanced measurement approaches can access nanocrystal properties beyond the scope of conventional ensemble or emission-based techniques. In parallel, the findings support the practical development of stable, high-performance nanocrystal-based devices.

Table of Contents

1

Introduction

Over the past decades, the continuous miniaturization of functional components, most notably transistors and processors, has fundamentally shaped materials science and technology. This development, initially driven by the demand for faster and more efficient computing, has enabled the rise of compact devices such as smartphones and laptops. Today, with the skyrocketing advancement of artificial intelligence, the need for small, powerful, yet cost-effective hardware is more urgent than ever. Miniaturization has not only advanced consumer electronics but also opened up entirely new physical regimes, where materials at the nanoscale reveal behaviors fundamentally different from their bulk counterparts. One of the most striking examples is quantum confinement, which allows for precise control over optical and electronic properties, such as bandgap tuning, in semiconductor nanocrystals. These effects are not merely of academic interest; they underpin real-world technologies ranging from biomedical imaging and drug delivery to display technologies, such as liquid-crystal display (LCD) panels and quantum dot displays (QLED) for TVs. The importance was confirmed again in 2023 when the Nobel Prize in Chemistry was awarded to Louis E. Brus, Alexei I. Ekimov, and Moungi G. Bawendi for the discovery and synthesis of colloidal quantum dots.[1–4] Since the discovery in the early 1980s, a wide range of nanomaterials have been explored, but none have sparked as much attention in such a short time as metal halide perovskites and especially lead halide perovskites. They gained momentum after Kojima et al. showcased the use of lead halide perovskites as visible-light sensitizers in solar cells in 2009, triggering a surge of interest and significant efficiency improvements over the following years.[5,6]

As the term perovskite is broadly used for any compound adopting the same ABX_3 crystal structure, research quickly branched out into various compositions and dimensionalities. A milestone was reached in early 2014 when the first successful synthesis of colloidal lead halide perovskite nanocrystals combined the favorable optoelectronic properties of perovskites with the size-tunable characteristics of quantum dots.[7,8] At this point, the phrase *"... in recent years, halide perovskite nanocrystals have emerged as promising candidates for ..."* has probably opened thousands of research articles. It is overused and yet not undeserved. Since their discovery less than fifteen years ago, perovskite nanocrystals have demonstrated remarkable properties, including high photoluminescence quantum yields, defect tolerance, tunable bandgaps across the visible spectrum, absorption cross-sections that surpass those of traditional semiconductors, and, more recently, potential application in quantum information technology.[9–11] Combined with a facile room-temperature synthesis, the hype surrounding this material is plausible. However, anyone who has spent more than a few months in a lab working with lead halide perovskite nanocrystals knows it is not all smooth sailing. There were certainly days I stood in the laser lab, wondering whether the measurement anomaly was caused by the setup or by the perovskite sample. In hindsight, it was the perovskite 80% of the time. These anomalies stem from several intrinsic and extrinsic factors, including instability under oxygen and moisture, surface traps resulting from ligand desorption, and photodegradation, all of which complicate the reproducibility and reliability of measurements.[12,13] And yet, perovskite-based devices now rival or even outperform traditional technologies in solar cell and light-emitting diode efficiency. More recently, the field has shifted its focus from pushing performance limits to addressing stability and scalability—challenges that are relevant when transitioning from lab-scale demonstrations to real-world applications.[14,15]

This thesis focuses on lead halide perovskite nanocrystals and bridges the gap between fundamental questions on exciton behavior and practical guidelines for integrating nanocrystals into optoelectronic devices, such as light-emitting diodes and photodetectors. Chapter 2 provides the necessary background in semiconductor physics, light-matter interaction, and the specific properties of lead halide perovskites to understand all results presented. Chapter 3 describes the custom-built setups and experimental methods used to acquire and analyze the gathered data. In Chapter 4 through Chapter 6, various properties of lead halide perovskite nanocrystals, including light absorption and exciton dynamics, stability, and energy transfer into encapsulated nanocrystals, are explored. More specifically, the first part of this work investigates how nanocrystal shape and size affect their absorption cross-sections and exciton dynamics at the ensemble level. The second part then focuses on absorption measurements of individual nanocubes using cavity-enhanced extinction spectroscopy. These experiments aim to go beyond traditional single-crystal photoluminescence studies by directly probing absorption in individual nanocubes. In the final part of the thesis, the perspective becomes more application-oriented. Here, the stability and energy transfer efficiency of polymer-encapsulated nanocrystals as a function of shell thickness is examined. The goal is to enhance the long-term stability without entirely blocking charge injection – a tradeoff that is essential when aiming to integrate nanocrystals into real devices.

Although the individual chapters of this thesis address different aspects of lead halide perovskite nanocrystals, ranging from fundamental exciton dynamics and single-nanocrystal absorption to issues of stability and device integration, they share a common objective: to advance the comprehensive understanding of nanocrystal–light interactions and assess their suitability for optoelectronic applications.

2

Fundamentals

The core of this thesis is built around the optical properties of lead halide perovskite nanocrystals. To establish the necessary foundation, first, the structural properties of crystalline solids, with a particular focus on the perovskite lattice and its characteristic defects, are discussed in this chapter. Building on this, the principles of electronic band formation are introduced, leading to a detailed understanding of semiconductors and the specific band structure of lead halide perovskites. Afterward, light-matter interactions are explored, from fundamental photon absorption to charge carrier relaxation, exciton formation, and exciton recombination pathways. The unique effects of quantum confinement in nanocrystals are discussed alongside methods to tune their morphology and strategies to enhance their stability. Finally, energy transfer mechanisms between nanocrystals are briefly outlined, providing the theoretical background necessary for interpreting the experimental results presented later.

2.1 Crystal Structures of Solids

The physical properties of solid materials are determined by the arrangement of their constituent atoms. In crystalline solids, atoms are organized in a repeating three-dimensional (3D) lattice defined by translational symmetry. This section introduces the basic concepts of lattice periodicity and unit cells and outlines the perovskite crystal structure, as all results presented in this work focus on that material.

2.1.1 Periodic Order in Crystalline Materials

To understand the fundamental concepts presented in this thesis, it is first necessary to understand the elemental composition of solid materials. All properties of a solid, such as electrical and thermal conductivity and hardness, originate from the atoms (or, in some cases, molecules) that constitute the material and their specific structure. This directly introduces the two main components of a solid: the structure or lattice and the material itself, i.e., the atoms. A crystal is defined as the periodic repetition of the smallest possible unit cell (primitive unit cell), which enables the formation of an extended structure through translational symmetry along distinct axes. This translation $\mathbf{R}$ is defined by a linear combination ($n_i \in \mathbb{Z}$) of the primitive translation vectors $\mathbf{a}_i$, which span a coordinate system determined by the lattice's symmetry:

$$\mathbf{R} = n_1\mathbf{a}_1 + n_2\mathbf{a}_2 + n_3\mathbf{a}_3 \tag{2.1}$$

A distinction should be made between a primitive unit cell, which contains only one lattice point and represents the smallest repeating volume, and a conventional unit cell, which may contain multiple lattice points and is chosen for its symmetry and ease of visualization. Figure 2.1 a illustrates these components separately (lattice points and primitive translation vectors $\mathbf{a}_i$) and in an extended form (atomic basis periodically at lattice points) in two dimensions.

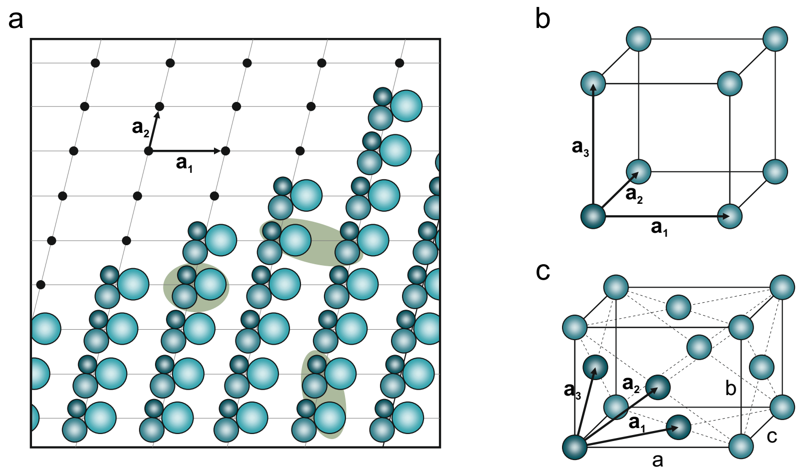

Figure 2.1: Types of Crystal Lattices. a) 2D lattice (black dots) with primitive translation vectors $\mathbf{a}_1$ and $\mathbf{a}_2$. Atoms at the lattice points form the crystal structure, and several possible atomic bases are highlighted in green. **b)** Schematic representation of a simple cubic lattice. **c)** Schematic representation of an orthorhombic ($|a| \neq |b| \neq |c|$) face-centered lattice. The spheres represent lattice points, with the darker sphere(s) indicating the lattice point(s) associated with the corresponding primitive unit cell. Adapted from Reference [16].

It should be noted that there are different possibilities of lattices and corresponding atomic bases, ultimately leading to various different crystal structures. Examples of the simple cubic lattice with a single-atom basis and the face-centered orthorhombic lattice are depicted in Figure 2.1 b-c. The interactions between atoms within the lattice can be of various natures. Crystals can be composed of atoms bonded through covalent, ionic, metallic, or van der Waals interactions.

2.1.2 Perovskite Crystal Structure

Although the first discovered mineral with the perovskite structure was $CaTiO_3$, the term perovskite today is most commonly associated with lead halide perovskites. The perovskite structure is characterized by the ABX_3 formula, typically comprising a monovalent A-cation, a divalent B-cation, and three monovalent X-anions. The bonding is predominantly ionic. This involves charged ions: the A and B cations tend to donate electrons to the X anions, creating electrostatic attraction. The prominent and most famous perovskites are those based on lead and halides, as the term lead halide perovskite implies. Lead acts as the B-cation, while the X-anion can be bromide, iodide, or chloride. The A-cation offers some versatility, often being cesium, though small organic molecules also suffice. Common examples include methylammonium (MA) and formamidinium (FA), which resulted in the designation of these materials as organic-inorganic perovskites. The atomic composition influences the crystal structure, for instance, $CsPbBr_3$, the composition primarily focused on in this thesis, exists in an orthorhombic phase at room temperature (RT). This phase arises because the cesium cation does not fully occupy the space within the octahedral framework, causing the octahedra to tilt. As the temperature increases, the structure transitions from orthorhombic to tetragonal at approximately 88 °C and then to cubic at around 130 °C. All experimental measurements in this study were conducted at or below RT, meaning that the orthorhombic phase of $CsPbBr_3$ was present. Examples of the perovskite crystal structure are depicted in Figure 2.2. For completeness, it should be noted that $MAPbBr_3$, which is also used in this thesis, exhibits similar phase transitions but at different temperatures. At −36 °C it transitions from cubic to tetragonal and at −128 °C to the orthorhombic phase.[17]

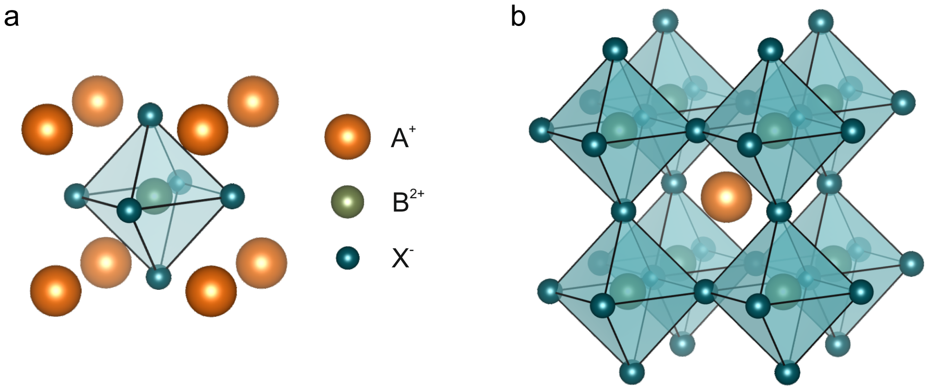

Figure 2.2: Perovskite Crystal Structure. a) Perovskite unit cell with A-cations sitting at each corner of the cell, the B-cation occupies the center, and the X-anions are located at the face-centered positions. **b)** A different illustration of the perovskite structure where the A-cation is surrounded by 8 corner-sharing octahedra spanned by the X-anions, each with a B-cation at their center.

2.2 Electronic Structure of Solids

The electronic structure of a solid determines many of its physical properties, including conductivity, optical absorption, and carrier dynamics. In contrast to isolated atoms, where electrons occupy discrete energy levels, the close packing of atoms in a crystal leads to the formation of continuous energy bands. This section introduces the fundamental concepts of electronic band formation and explains how the band structure and the Fermi level define the material class. It also highlights how the electronic structure of lead halide perovskites differs from that of conventional semiconductors. Finally, the role of defects, both in general and specifically in lead halide perovskites, is discussed.

2.2.1 Electronic Band Formation

A basic understanding of how atomic orbitals interact in a periodic lattice is provided by the tight-binding model, which assumes electrons are primarily localized around their parent atoms but can tunnel to neighboring atoms. When multiple atoms come together to form a solid, their individual orbitals overlap, and these discrete levels broaden into energy bands. They create a continuous energy band if the separation between energy levels is small enough. If the opposite is true and no electronic states exist in certain regions, so-called band gaps form. Combined with the occupation of the energy states, these are essential in distinguishing insulators, semiconductors, and metals. This approach intuitively explains why electronic bands exist. However, to understand the behavior of charge carriers in a crystal, the periodic nature of the lattice has to be considered. For that purpose, the time-independent single electron Schrödinger equation is modified to comprise a periodic potential $V(\mathbf{r}) = V(\mathbf{r} + \mathbf{R})$:[18,19]

$$\left(\frac{\mathbf{p}^2}{2m_\mathrm{e}} + V(\mathbf{r})\right)\psi_{\mathrm{n},\mathbf{k}}(\mathbf{r}) = E_\mathrm{n}(\mathbf{k})\,\psi_{\mathrm{n},\mathbf{k}}(\mathbf{r}) \tag{2.2}$$

with $\mathbf{p} = -i\hbar\nabla$ being the momentum operator and m_e the electron mass. Solving this equation yields the so-called dispersion relation $E_\mathrm{n}(\mathbf{k})$, describing the energy of electrons as a function of their momentum. The solution takes the form of Bloch functions:

$$\psi_{\mathrm{n},\mathbf{k}}(\mathbf{r}) = e^{i\mathbf{kr}} \cdot u_{\mathrm{n},\mathbf{k}}(\mathbf{r}) \tag{2.3}$$

where $u_{\mathrm{n},\mathbf{k}}(\mathbf{r})$ has the periodicity of the crystal lattice. This means that electrons in a crystal behave like free fermions modulated by the periodic potential. Each wave vector $\mathbf{k}$ corresponds to an allowed energy state, and for each $\mathbf{k}$, multiple solutions labeled by n (the band index) describe the different energy bands. Since the potential $V(\mathbf{r})$ is periodic, it is suitable to analyze the problem in reciprocal space (k-space), where the periodicity of the crystal lattice is expressed in terms of wave vectors. If a crystal lattice in real space is defined by the primitive lattice vectors $\mathbf{a}_i$, then a corresponding reciprocal lattice exists in k-space, described by the primitive reciprocal lattice vectors $\mathbf{b}_i$, which are obtained through a Fourier transformation of the real-space lattice. Importantly, the electron wave functions $\psi_{\mathrm{n},\mathbf{k}}(\mathbf{r})$ and their corresponding energies $E_n(\mathbf{k})$ remain unchanged when the wave vector $\mathbf{k}$ is shifted by a reciprocal lattice vector $\mathbf{G}$, where $\mathbf{G} = m_1\mathbf{b}_1 + m_2\mathbf{b}_2 + m_3\mathbf{b}_3$. This periodicity implies that all physically distinct electron states can be fully represented within the 'primitive unit cell' of the reciprocal lattice, better known as the first Brillouin zone, making it the fundamental domain for analyzing the electronic band structure. In the Brillouin zone, high-symmetry points, so-called critical points, and their connections are labeled with distinct letters (like Γ, R, Δ, X, M, etc.). Given the complexity of visualizing a band as a function of the wave vector, band structure plots typically show $E_\mathrm{n}(\mathbf{k})$ values for $\mathbf{k}$ along lines connecting these symmetry points, which capture the most important features of the band structure. While the band structure provides information about electron energy dispersion, it is also essential to consider the density of states (DOS), which describes the number of electronic states available at each energy level. It is defined as:

$$D(E) = \frac{1}{V} \sum_{\mathrm{n},\mathbf{k}} \delta(E - E_\mathrm{n}(\mathbf{k})) \tag{2.4}$$

where V is the volume of the crystal. The DOS plays a crucial role in determining a material's electronic properties. Peaks in the DOS indicate energies with many electronic states, often corresponding to flatter bands (low dispersion). In contrast, regions with zero DOS correspond to band gaps. The DOS influences electrical conductivity, heat capacity, and other material properties by dictating how electrons populate states under external influences such as temperature and doping. In current scientific research, various computational techniques are available for calculating the band structure of solids along their high-symmetry axes. Density functional theory (DFT) is probably the most recognized method. Due to various additional packages for specific tasks, DFT can provide highly accurate predictions of band structures, band gaps, and the DOS.

2.2.2 Direct and Indirect Semiconductors

Having established the fundamental understanding of electronic states in solids, the focus now lies on main types of solids distinguishable by their electronic properties: insulators, semiconductors, and metals. The classification is determined by the position of the so-called Fermi level E_F within the electronic band structure. The Fermi level is defined as the maximum energy that electrons can occupy at $T = 0\,\mathrm{K}$, a consequence of the Pauli exclusion principle, which states that each energy state can be occupied by a maximum of two electrons with opposite spins. The material is classified as a metal if the Fermi level lies within an energy band. If it is located in a band gap, the width of this gap (called band gap energy E_G) dictates whether the material behaves as an insulator ($E_\mathrm{G} \geq 4\,\mathrm{eV}$) or as a semiconductor ($E_\mathrm{G} < 4\,\mathrm{eV}$). The band directly below the Fermi level is called the valence band (VB), while the band immediately above it is known as the conduction band (CB). In metals, the partial occupancy of electronic states enables free charge carrier movement, resulting in high conductivity even at very low temperatures. At $T = 0\,\mathrm{K}$, semiconductors and insulators show no difference in conductivity since charge carriers do not occupy states with higher energy. When temperature is considered, the occupation probability switches according to Fermi-Dirac statistics:

$$f(E,T) = \frac{1}{\exp\left(\frac{E-E_\mathrm{F}}{k_\mathrm{B}T}\right) + 1} \tag{2.5}$$

with k_B being the Boltzmann constant. Only then can thermal excitation in semiconductors promote electrons across the band gap, allowing controlled conductivity, while in insulators, the large band gap still prevents significant charge carrier movement, leading to negligible conductivity. When an electron is promoted from the fully occupied VB to the CB, it leaves behind an unoccupied state, commonly referred to as a hole. Holes, similar to electrons, contribute to electrical conductivity. The perovskites examined in this thesis are all classified as semiconductors. Within semiconductors, a further distinction is made between direct and indirect semiconductors based on the positions of the valence band maximum (VBM) and conduction band minimum (CBM) in k-space. If the VBM and CBM are located at the same point in k-space, the semiconductor is classified as direct, whereas if they are positioned at different locations, it is considered indirect (see Figure 2.3).

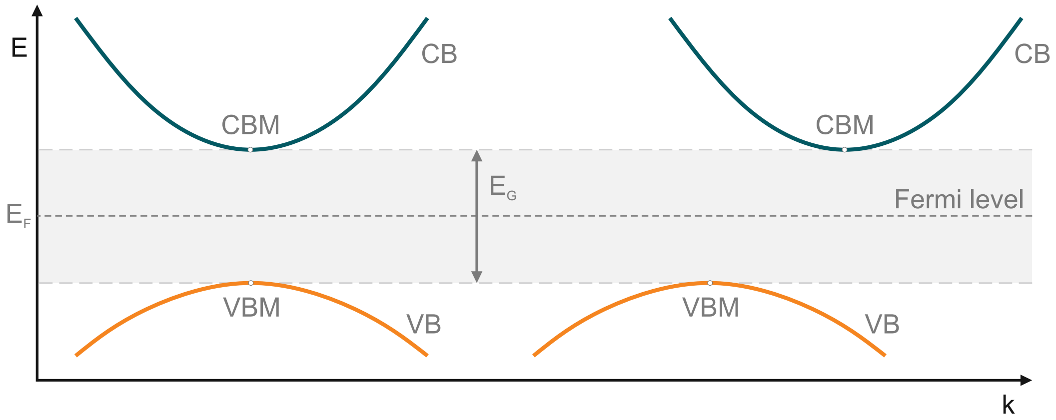

Figure 2.3: Direct and Indirect Band Gap of a Semiconductor. VBs and CBs of direct and indirect semiconductors. The VBM and the CBM are at the same position (left) for direct and at different positions for indirect semiconductors (right). The Fermi level is positioned in the center of the band gap.

Additionally, the motion of charge carriers in a crystal lattice is influenced by the periodic potential of the lattice itself. This effect is commonly accounted for by using an adjusted mass known as the effective mass $m^*_{\mathrm{e/h}}$, which is mathematically described by the curvature of the dispersion relation:

$$\frac{1}{m^*_{\mathrm{e/h}}} = \frac{1}{\hbar^2} \left| \frac{\mathrm{d}^2 E_{\mathrm{CB/VB}}(\mathbf{k})}{\mathrm{d}\mathbf{k}^2} \right| \tag{2.6}$$

Near band extrema, electrons, and holes behave similarly to free charge carriers, exhibiting a quadratic dispersion relation. However, the influence of the crystal lattice is incorporated into their modified effective mass.

2.2.3 Electronic Structure of Perovskites

When applying this analysis to perovskites, their electronic band structure can be determined. Perovskites are direct semiconductors with a band gap located either at the R-point (cubic phase) or at the Γ-point (tetragonal and orthorhombic phase).[20,21] However, their general band structure differs significantly from conventional direct semiconductors such as GaAs. A simplified comparison of conventional and perovskite semiconductor band structures is shown in Figure 2.4 a. In conventional semiconductors, the VB primarily comprises bonding states, while antibonding states mainly form the CB. For perovskite, the band structure originates from the hybridization of the atomic orbitals of the B-site (Pb in this thesis) and X-site ions (halides in this thesis). The VBM mainly arises from the antibonding interaction between Pb 6s and halide p-orbitals (Cl 3p, Br 4p, or I 5p, depending on the halide compound). The CBM is predominantly formed by the antibonding Pb 6p orbitals.[22,23] Unlike conventional semiconductors, whose band gap increases as temperature decreases, this unique electronic structure leads to the opposite behavior.[24–26] Because the halide p-orbitals significantly contribute to the VBM, altering the halide composition allows for band gap tuning. By replacing Cl, Br, or I in the perovskite structure (e.g., $APbCl_3$ to $APbBr_3$ to $APbI_3$), the band gap can be adjusted across a wide range of energies. This tunability is a key advantage of perovskites for optoelectronic applications. Although the A-site cation does not directly form the electronic states near the band edges, it affects the band gap by modifying the Pb-X-Pb bond angles in the crystal structure. Larger cations induce greater tilting of these bonds, influencing the overall electronic properties.[27–29]

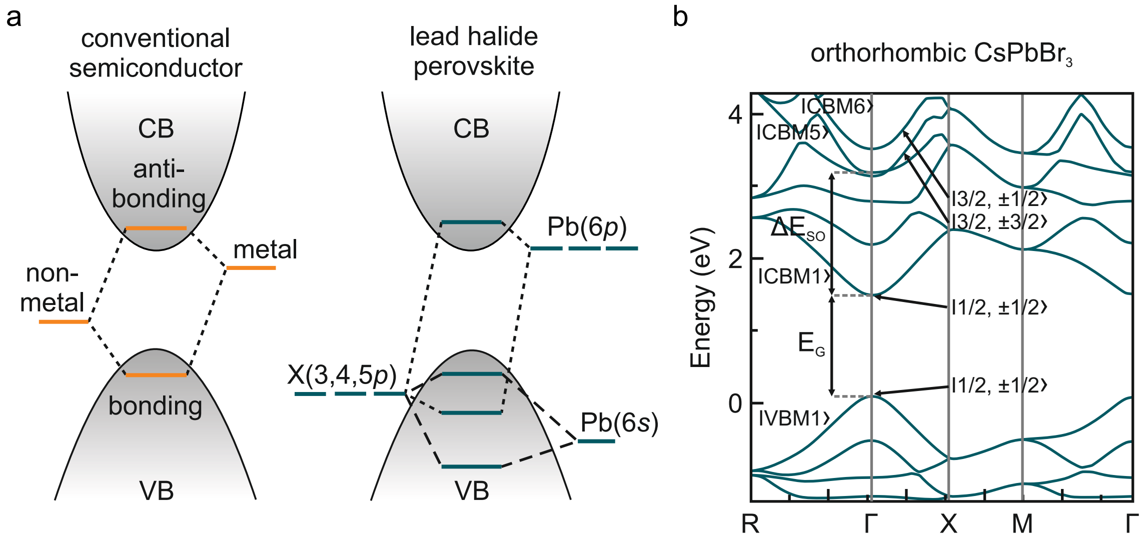

Figure 2.4: Electronic Band Structures. a) Schematics of the origin of the electronic band structure of conventional semiconductors (like GaAs, left) and lead halide perovskites (right). Adapted from Reference [30]. **b)** DFT calculation of the electronic band structure of orthorhombic $CsPbBr_3$. $|CBM1\rangle$ corresponds to the split-off band whereas $|CBM5\rangle$ and $|CBM6\rangle$ are the heavy- and light electron bands respectively. Adapted from Reference [21].

In conventional semiconductors like GaAs, for example, the VBM, located at the Γ-point, consists of three degenerate bands due to the p_x, p_y, and p_z symmetry of the atomic p-orbitals. These bands are generally called heavy-hole, light-hole, and split-off band due to their band curvature and consequent effective mass, and each is twofold degenerate since each band accommodates two spin states. Therefore, without considering spin-orbit coupling, the total degeneracy at the Γ-point is sixfold (three bands, two spins). The inclusion of spin-orbit coupling lifts this degeneracy by separating the split-off band (twofold) from the heavy and light-hole bands (fourfold). A key difference for materials containing heavy elements, such as lead-based perovskites like $CsPbBr_3$, is that this strong p-orbital contribution appears in the CB instead of the VB. As a result, the CBM is initially triply degenerate (sixfold when including spin), forming heavy and light electron bands along with a split-off band analogous to the VB structure in conventional semiconductors. The situation is further complicated by the influence of crystal phase, symmetry breaking, and lattice strain. These effects can lead to unit cell doubling, which in turn causes Brillouin zone folding and effectively doubles the originally triply degenerate CBM, resulting in six active Bloch states for the CBM ($|CBM1-6\rangle$) and two for the VBM ($|VBM1-2\rangle$)).[21,31] Although these states are described as the CBM, it is important to note that the term now encompasses multiple sub-bands due to the aforementioned degeneracy lifting. The actual CBM is defined by the lowest-energy split-off band ($|CBM1\rangle$), while the heavy and light electron bands are pushed to significantly higher energies ($|CBM5\rangle$ and $|CBM6\rangle$) (see Figure 2.4 b). Similarly, the VBM is also affected by spin-orbit coupling, reducing its degeneracy. As a result, both the CBM and VBM in $CsPbBr_3$ are only twofold degenerate, with spin being the only remaining degeneracy.

2.2.4 Defects in Solids

Until now, it was assumed that crystal lattices are flawless, with every atom precisely at its theoretical position. In reality, atoms within a crystal can be displaced from their intended locations, introducing imperfections known as defects. These so-called defects significantly influence many properties of crystals. The types of defects that can occur and the impact they have, specifically in ionic crystals like lead halide perovskites, will be discussed in the following.

General:

In general, defects can be categorized into point defects, such as vacancies, interstitials, and antisites, and extended defects, like dislocations and grain boundaries. Point defects are localized disorders at the atomic scale and influence electronic and optical properties, whereas extended defects, which span multiple unit cells, mainly affect mechanical and transport characteristics. A vacancy refers to a missing atom at a regular lattice point, which can occur when an atom is displaced to the surface. An interstitial is a crystal atom or an impurity that occupies a position between regular lattice points, causing significant lattice distortion and usually requiring high formation energy. Antisites arise in crystals composed of two or more elements and refer to atoms occupying incorrect lattice positions, such as a cation on an anion site and vice versa. Extended defects include dislocations, often conceptualized as 1D lines of lattice mismatch (e.g., an extra atomic row terminating within the crystal), and grain boundaries, which are planar defects occurring in polycrystalline materials between crystallites of different orientations. Among these, point defects are particularly relevant in optoelectronic performance, as they can alter the electronic structure and introduce localized states within the band gap, also referred to as trap states. Whether these states lie energetically within the CB, the VB, or the band gap depends on the nature of the defect. Trap states located near the band edges—known as shallow traps—do not impact charge carrier transport strongly, as charge carriers can escape thermally. In contrast, deep traps, situated further inside the band gap, can capture carriers for extended periods, acting as non-radiative recombination centers and significantly affecting device performance. The types and concentrations of defects in a given crystal depend on a combination of factors, including its atomic composition, bonding character, synthesis method, and crystal size. Finally, it is worth noting that defects can also be extrinsic, arising from foreign atoms or impurities unintentionally incorporated during crystal growth. Because this work focuses primarily on intrinsic point defects, extrinsic effects are not discussed here.[16]

Lead Halide Perovskites - $CsPbBr_3$

One of the most prominent features of lead halide perovskites is their so-called defect tolerance. In contrast to many conventional semiconductors, these materials can exhibit relatively high defect concentrations without a corresponding decrease in optical or electronic performance. Using first-principle DFT calculations, it is possible to model not only the band structure of a crystalline solid but also the electronic states associated with defects. Since this work focuses on optical properties, the discussion here is limited to point defects, and extended defects are not considered. Figure 2.5 a shows a schematic representation of the $CsPbBr_3$ perovskite structure, illustrating the three main types of point defects—vacancies, interstitials, and antisites. Among the twelve distinct point defects possible in this material, nine are found to introduce shallow trap states.[32] These states enable fast carrier exchange with the bands and are not expected to trap carriers over long timescales. Only three defects, namely the lead interstitial (Pb_i) and the antisites Pb_{Br} and Br_{Pb}, are predicted to create deep traps. However, these defects also possess high formation energies, suggesting they are statistically unlikely to form under typical growth conditions. Figure 2.5 b also illustrates how these defect states alter the electronic structure described earlier in Subsection 2.2.3. The VBM in $CsPbBr_3$ arises from antibonding interactions between Pb-6s and Br-4p orbitals, while the CBM is derived primarily from Pb-6p orbitals with minimal Br contribution. Because there is little bonding–antibonding overlap across the band gap, defect-induced levels tend to fall outside the gap, leading to shallow rather than deep mid-gap traps. This material property is widely accepted as the fundamental reason for the material's defect tolerance.

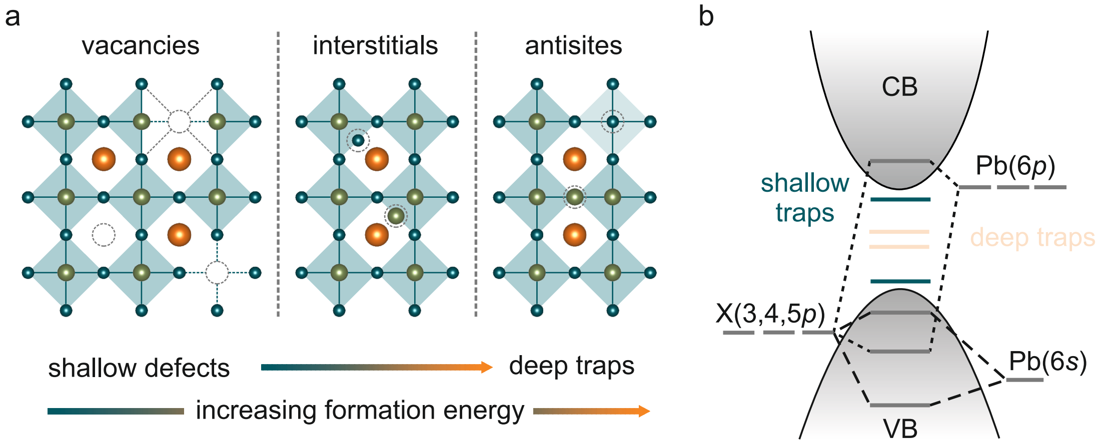

Figure 2.5: Defects in Lead Halide Perovskites. a) Overview over different point defects in a lead halide perovskite crystal lattice. Adapted from Reference [33] **b)** Schematics of the electronic band structure of lead halide perovskites and the energetic positions of shallow and deep trap states introduced by specific point defects. Adapted from Reference [30].

2.3 Fundamentals of Photon Absorption

Having established a fundamental understanding of the electronic structure of semiconductors, first, the quantum mechanical description of absorption is explained, with excitation probabilities determined by Fermi's Golden Rule. Next, the macroscopic description of light attenuation is presented by introducing the absorption coefficient and the Lambert-Beer law. Finally, the single-particle absorption cross-section is introduced to bridge the microscopic and macroscopic worlds.

2.3.1 Absorption in Semiconductors

Charge carriers in a semiconductor can be excited via different mechanisms, including optical excitation, where a photon provides the necessary energy, impact ionization, where a high-energy carrier transfers energy to another carrier, and electrical excitation, where an external electric field facilitates carrier transitions. Since the primary excitation mechanism utilized in this thesis is optical, it will be assumed that electrons are excited from the VB to the CB via photon absorption. The probability of such excitation events is governed by quantum mechanical selection rules and can be described using Fermi's Golden Rule:

$$\Gamma_{\mathrm{i}\rightarrow\mathrm{f}} = \frac{2\pi}{\hbar} \cdot |\langle f|H'|i\rangle|^2 \cdot D_{\mathrm{j}}(\hbar\omega) \tag{2.7}$$

where $\Gamma_{\mathrm{i}\rightarrow\mathrm{f}}$ is the quantum mechanical transition rate for the excitation of an electron from an initial state in the VB $|i\rangle$ to a final state in the CB $|f\rangle$ by absorption of a photon with angular frequency ω, $|\langle f|H'|i\rangle|^2$ or the so-called matrix element is the external perturbation caused by the electromagnetic wave on the electron and $D_{\mathrm{j}}(\hbar\omega)$ is the joint DOS evaluated at the photon energy. It is important to note that, unlike the DOS mentioned in Equation 2.4, the joint DOS does not account for all possible states. Instead, it describes the density of paired states—specifically pairs of occupied states in the VB and unoccupied states in the CB—representing all possible transitions between an initial and a final state. Since photons carry negligible momentum, these optical transitions are illustrated by a vertical line in an electronic band structure. Fermi's Golden Rule provides a way to calculate the probability of an electronic transition when a photon of suitable energy interacts with a semiconductor. However, in an actual semiconductor crystal, absorption does not originate from a single transition but from many collective events occurring throughout the material. Therefore, it indirectly defines the shape of the absorption spectrum, while the so-called absorption coefficient determines the amount of absorbed light.

2.3.2 Absorption Coefficient and the Lambert-Beer Law

Generally, macroscopic light attenuation or extinction in a medium occurs due to two processes: scattering and absorption. In most cases discussed in this work, scattering is negligible and will, therefore, not be considered here. Whenever scattering becomes relevant, it will be explicitly addressed. To mathematically describe the attenuation of light traveling through an absorbing material, the following differential equation can be used:[34,35]

$$\frac{dI}{dx} = -\alpha I \tag{2.8}$$

with α being the absorption coefficient. The solution to this equation is the Lambert-Beer law:

$$I(x) = I_0 e^{-\alpha x} \tag{2.9}$$

where I_0 is the light intensity at $x = 0$. The solution is more commonly written in its logarithmic form:

$$\ln\left(\frac{I_0}{I}\right) = \alpha x \tag{2.10}$$

Another way to quantify the absorption is with the so-called optical density (OD) or absorbance (A) defined as:

$$A = \log\left(\frac{I_0}{I(l)}\right) = \frac{\alpha l}{\ln(10)} \propto \alpha l \tag{2.11}$$

where l is the length of the absorbing medium and $I(l)$ the intensity of the transmitted light. In general, the absorption strength of a material is described by the absorption coefficient α (in units of cm^{-1}). Due to the electronic band structure in semiconductors, light absorption strongly depends on the photon energy. Figure 2.6 a shows the electronic band structure of the organic-inorganic perovskite $\mathrm{MAPbI_3}$. Depending on the energy of the photon, charge carriers are generated at different positions in the bands. Photons with energies below the band gap cannot promote electrons from the VB to the CB and are, therefore, not absorbed under normal conditions. As a result, the absorption spectrum of a semiconductor is directly governed by its electronic structure, with the absorption onset typically located at the band gap energy (see Figure 2.6 b). The absorption coefficient is further influenced by the shape of the bands. Flatter bands result in a higher DOS, which increases the probability of optical transitions and thus enhances absorption. While below-bandgap absorption is generally forbidden, it can occur at sufficiently high photon flux densities through nonlinear optical processes such as two-photon or multiphoton absorption, where two or more lower-energy photons are absorbed simultaneously to overcome the band gap. In contrast, when a single high-energy photon carries more than twice the band gap energy, it can generate multiple electron–hole pairs through a process known as carrier multiplication, although the probability of this process occurring is typically very low.[36,37]

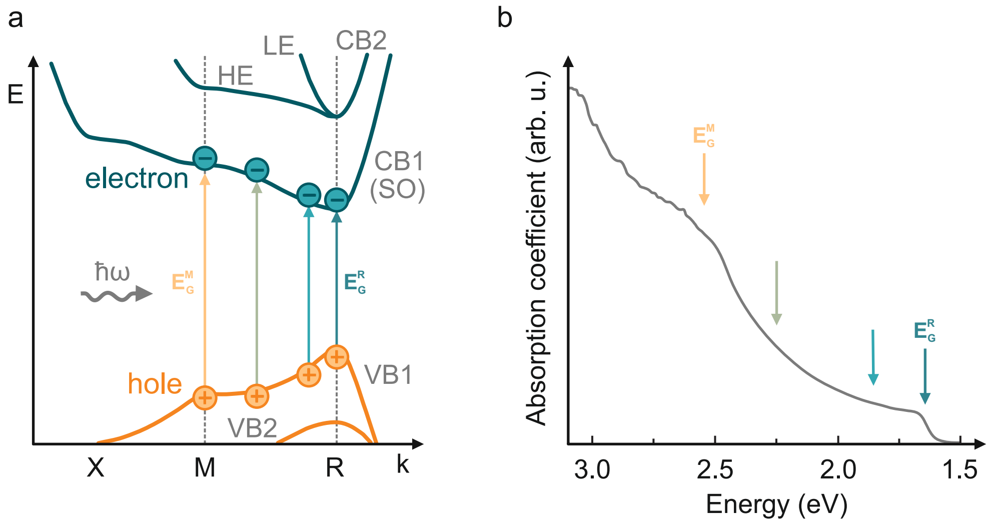

Figure 2.6: Band Structure and Absorption Spectrum of Cubic $\mathrm{MAPbI_3}$. a) Electronic band structure of cubic $\mathrm{MAPbI_3}$ from DFT calculations. There are two VBs and two CBs. The lower-lying CB1 is the split-off (SO) band, whereas the higher-lying CB2 consists of the light electron (LE) and the heavy electron (HE) band. Colored arrows show possibilities for optical absorption. **b)** Optical absorption spectrum of $\mathrm{MAPbI_3}$. The colored arrows correspond to the same positions of absorption at different positions in k-space. The absorption onset corresponds to the band gap at the *R*-point. Adapted from Reference [20].

Instead of a continuous absorbing medium as previously assumed, the absorption coefficient α can also be described for a transparent material containing many separated absorbing particles, such as molecules or small crystals. In this case, α can be expressed in two equivalent ways. By the molar extinction coefficient ϵ (in units of $\mathrm{L\,mol^{-1}\,cm^{-1}}$) typically defined using a decadic logarithm, with the relation: $\alpha = \epsilon c \ln(10)$ where c is the molar concentration ($\mathrm{mol\,L^{-1}}$). Or, α can also be linked directly to the number density n (in cm^{-3}) and the absorption cross-section σ_{abs} (in cm^2) of each individual particle via:[35,38]

$$\alpha = \sigma_{\mathrm{abs}}\, n = \sigma_{\mathrm{abs}} \frac{N_A c}{10^3} \tag{2.12}$$

Here, the number density n is related to the molar concentration c by $n = \frac{N_A c}{10^3}$ where N_A is Avogadro's number and the factor 10^3 accounts for the conversion from liters to cubic centimeters.

2.4 Carrier Dynamics After Excitation

The previous chapter described how photons with energies above the band gap are absorbed by the material, resulting in the generation of free charge carriers. This section focuses on the subsequent carrier dynamics. Following excitation, the carriers typically possess excess kinetic energy and are not yet in thermal equilibrium. The excited electrons and holes redistribute energy through thermalization, dissipate heat to the lattice via phonon emission, and eventually form bound electron-hole pairs stabilized by Coulomb attraction. The section concludes with an overview of recombination pathways, through which the electron-hole pairs return to their ground state, either by emitting a photon or through non-radiative processes.

2.4.1 Charge Carrier Relaxation

All results presented in this thesis are based on photogenerated charge carriers, which are excited far into the CB. Although most of the experimental observations and subsequent analysis focus on interband transitions—i.e., transitions from the VB to the CB—a brief discussion of the immediate post-excitation carrier dynamics is included here, with a particular focus on lead halide perovskites. A schematic overview of the described processes is shown in Figure 2.7, where Figure 2.7 a shows the evolution of carrier distributions in the VBs and CBs, and Figure 2.7 b illustrates the same dynamics in the simplified so-called one-particle picture. Prior to excitation ($t < 0\,\mathrm{s}$), the system is assumed to be in thermal equilibrium with no electrons in the CB (0). At $t = 0\,\mathrm{s}$, a spectrally narrow (few meV) and ultrashort laser pulse (femtosecond to picosecond pulse width) with photon energy well above the band gap ($\hbar\omega \gg E_\mathrm{G}$) initiates an interband absorption process (1). This results in the generation of electron-hole pairs with significant excess energy. Due to the narrow spectral width of the excitation pulse, the initial carrier energy distribution is sharply peaked. Within the first few hundred femtoseconds, carrier–carrier scattering dominates the dynamics, redistributing energy and momentum among the carriers (2). This process, known as carrier thermalization, drives the system toward a quasi-equilibrium state described by a Fermi-Dirac distribution. Once thermalization is complete, the carriers can be described by an effective carrier temperature. The system then undergoes carrier cooling, transferring excess energy to the crystal lattice through phonon emission (3). Phonons are quasiparticles and can be described as quantized modes of lattice vibrations that mediate energy exchange between charge carriers and the crystal lattice. They are typically categorized as either acoustic phonons or optical phonons. Acoustic phonons correspond to in-phase atomic oscillations of unit cells and propagate sound. Optical phonons involve out-of-phase motion between atoms within the unit cell and can induce an oscillating dipole moment. They typically carry higher energy than acoustic phonons.[38] Carrier cooling in lead halide perovskites is pump fluence dependent and occurs on timescales of approximately $1 - 10\,\mathrm{ps}$.[39,40] The type of emitted phonons depends on the carrier energy. Hot carriers will preferably emit optical phonons to lose their energy quickly. For example, optical phonon energies in lead halide perovskites range from $10 - 20\,\mathrm{meV}$.[24,41,42] Moreover, the interaction between charge carriers and optical phonons is strongly enhanced in highly polar materials such as lead halide perovskites. This coupling is described by the Fröhlich interaction, which originates from macroscopic electric fields associated with longitudinal optical phonons.[25,43] Once carrier energy falls below the optical phonon threshold, further emission of these high-energy phonons is no longer possible. Cooling then proceeds more slowly via the emission of lower-energy acoustic phonons until the carriers accumulate near the band edges. The final process in this sequence is the recombination of electrons and holes, which will be discussed in the following section (4).

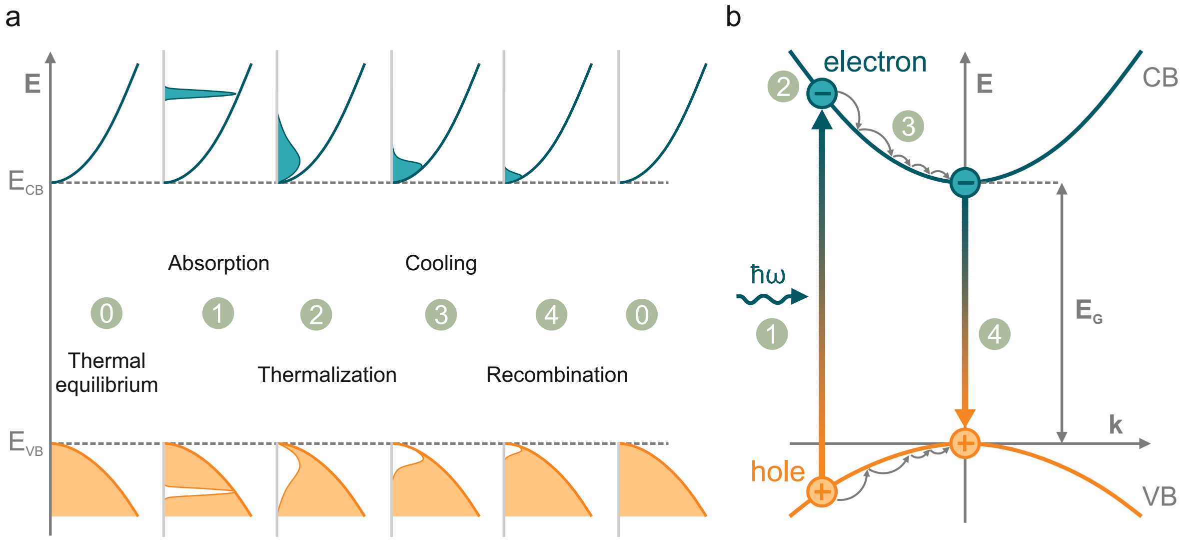

Figure 2.7: Charge Carrier Relaxation after Excitation. **a)** Schematic illustration of hot carrier dynamics in a semiconductor. After photon absorption, charge carriers are generated in non-equilibrium energy distributions. Through carrier-carrier interactions, they thermalize into Fermi-Dirac distributions characterized by an elevated temperature. Subsequently, the carriers cool down towards the lattice temperature via carrier-phonon interactions before eventually recombining. **b)** Representation of the corresponding hot carrier dynamics in the one-particle picture.

2.4.2 Excitons

With the charge carriers now relaxed to the band edges, it becomes necessary to consider the possibility of bound electron-hole complexes. Due to their opposite charges, a Coulomb attraction acts between them, potentially leading to the formation of a bound, charge-neutral electron-hole pair, a so-called exciton. Since excitons consist of two fermions, they behave as composite bosons. Depending on the spatial separation between the electron and the hole, excitons are classified as Frenkel or Wannier-Mott excitons. Frenkel excitons are strongly bound, with binding energies reaching up to 1 eV. As a result, they are localized and do not extend beyond a single unit cell. This type of exciton is predominantly found in organic semiconductors. In contrast, Wannier-Mott excitons are weakly bound, and their spatial separation can reach multiple unit cells. The resulting binding energies are much lower since the atoms between the electron and hole contribute to charge screening. This type of exciton is found in lead halide perovskites and will be discussed in detail. The energy levels of excitons can be described similarly to those of the hydrogen atom. The main difference is that an exciton can move freely within the crystal with a center-of-mass momentum given by $\mathbf{K} = \mathbf{k}_\mathrm{e} + \mathbf{k}_\mathrm{h}$. To solve the Schrödinger equation for excitons, both the reduced mass of the electron-hole system:[38]

$$\mu_\mathrm{X} = \left(\frac{1}{m_\mathrm{e}^*} + \frac{1}{m_\mathrm{h}^*} \right) \tag{2.13}$$

and the effective exciton mass $M_\mathrm{X} = m_\mathrm{e}^* + m_\mathrm{h}^*$ are introduced. This leads to the following exciton eigenenergies:

$$E_{\mathrm{n},\mathbf{K}} = E_\mathrm{G} - E_\mathrm{n} + \frac{\hbar^2 \mathbf{K}^2}{2M_\mathrm{X}} \tag{2.14}$$

where E_G denotes the band gap energy, $E_\mathrm{n} = R_\mathrm{y}^* \frac{1}{n^2}$ is the Coulomb interaction energy as derived from the hydrogen model, and the third term describes the center-of-mass motion of the exciton. The index n labels different energy levels where $n = 1$ defines the exciton binding energy E_B. This also happens to be the modified Rydberg energy of the hydrogen atom, taking into account the reduced exciton mass μ_X and the dielectric screening of the surrounding medium, given by $\epsilon = \epsilon_0 \epsilon_\mathrm{r}$:[35]

$$E_\mathrm{B} = E_{\mathrm{n}=1} = R_\mathrm{y}^* = \frac{\mu_\mathrm{X} e^4}{2\hbar^2 \left(4\pi\epsilon\right)^2} \tag{2.15}$$

To complete the analogy with the hydrogen model, the spatial extent of the exciton can be described by an excitonic Bohr radius, which is given by:

$$a_\mathrm{B} = \frac{4\,\pi\epsilon\hbar^2}{\mu_\mathrm{X} e^2} \tag{2.16}$$

The exciton Bohr radius a_B is generally much larger than the atomic Bohr radius due to the weaker Coulomb interaction in the screened medium and the lower reduced mass. To form stable excitons in a solid-state material, the exciton binding energy must typically exceed the available thermal energy $E_\mathrm{th} = k_\mathrm{B}T$. At RT (293 K), this energy is approximately 25 meV. While this condition is often used as a rule of thumb, it is not strictly required. As described by the Saha equation excitons and free charge carriers can coexist even when the thermal energy is comparable to or slightly larger than the binding energy, with the ratio between the two populations governed by thermodynamic equilibrium.[44,45] Generally, excitons form after photogenerated charge carriers have relaxed to the vicinity of the band edges. This relaxation is typically described within the one-particle picture, where electrons and holes are treated as independent particles in their respective conduction and VBs (see Figure 2.7 b). The energy loss of the relaxation process occurs via carrier-carrier interaction and phonon emission until thermal equilibrium near the band extrema is reached. To visualize this and the following recombination processes, a transition to the two-particle picture is necessary, where exciton energy levels are defined by the excitonic dispersion relation (see Figure 2.8 a). The VBs and CBs are no longer treated separately in this representation. Instead, excitons are described as discrete parabolic energy levels below the continuum of free electron-hole pairs. Photon absorption at energies well above the band gap ($E_\mathrm{ph} = \hbar\omega \gg E_\mathrm{G}$) creates unbound electron-hole pairs, which may subsequently bind to form excitons. In contrast, resonant excitation with photon energies matching the energy of the lowest bound exciton level (1s) can directly create excitons but only at the intersection between the photon dispersion relation ($E(k) = \hbar ck$) and the exciton dispersion relation, to satisfy momentum conservation. An absorption spectrum of a semiconductor with clearly highlighted exciton features in the form of absorption below the band gap can be seen in Figure 2.8 b. Since this work focuses on exciton dynamics, all recombination processes will be explained within the two-particle picture.

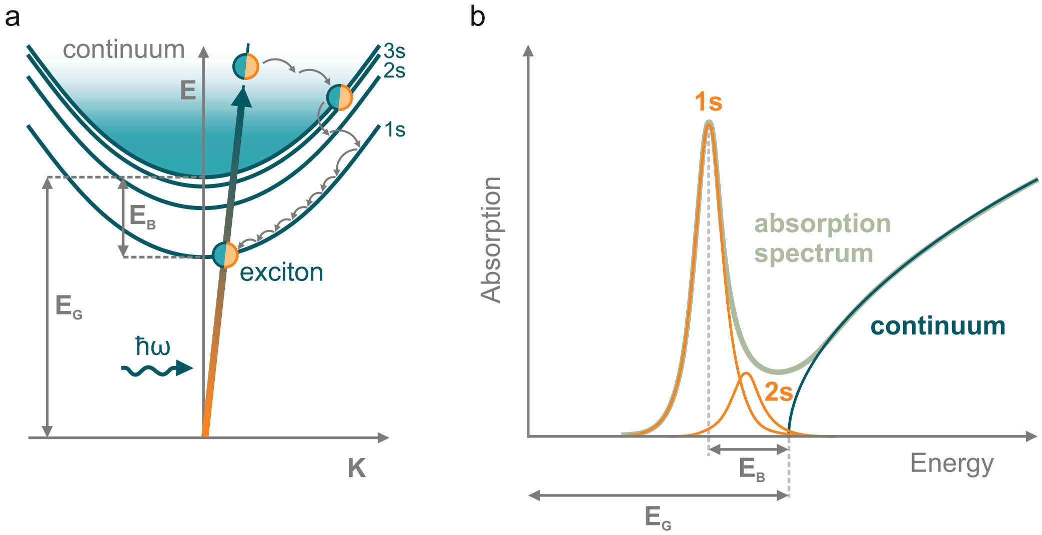

Figure 2.8: Two-Particle Picture and Exciton Absorption Spectrum. a) Photon absorption, free charge carrier generation, and subsequent exciton formation illustrated in the two-particle picture. A photon with energy exceeding the band gap first creates an electron-hole pair in the continuum. After relaxation, the carriers form a bound exciton, which then relaxes further toward the band edge through the emission of phonons. **b)** Absorption spectrum exhibiting strongly enhanced exciton features.

2.4.3 Recombination Mechanisms

After thermalization and cooling to the band edge, excitons eventually return to the ground state through radiative or non-radiative recombination. These recombination processes define the efficiency and dynamics of light emission in semiconductor materials.

Photoluminescence and Photoluminescence Quantum Yield

When an exciton recombines radiatively, its energy is released in the form of a photon. In the case of prior optical excitation, this process is referred to as photoluminescence (PL). Alternatively, if excitons are generated electrically or thermally, the corresponding radiative processes are electroluminescence and thermoluminescence. For PL, the emitted photon energy is typically close to the band gap energy but reduced by the exciton binding energy ($E_G - E_B$). Figure 2.9 illustrates the radiative recombination in the two-particle picture, where it becomes clear that radiative recombination is only allowed for excitons located on the so-called light cone, defined by the intersection of the exciton and photon dispersion relations. This restriction can be circumvented by involving, for example, a phonon that can satisfy energy and momentum conservation. In contrast, non-radiative recombination describes processes where the exciton energy is dissipated, often via phonon emission. A quantitative measure for the ratio between radiative and non-radiative recombination processes in a semiconductor is the PL quantum yield (PLQY). It quantifies how efficiently excitons emit photons:

$$\mathrm{PLQY} = \frac{k_\mathrm{r}}{k_\mathrm{r} + k_\mathrm{nr}} \tag{2.17}$$

A high PLQY indicates that most excitons recombine radiatively, which is crucial for optoelectronic applications.

Exciton Rate Equation

The total number of excitons n_X decreases over time as recombination proceeds. This behavior can be modeled using a rate equation that accounts for both monomolecular (single-exciton) and bimolecular (two-exciton) decay pathways:

$$\frac{dn_\mathrm{X}(t)}{dt} = -k_\mathrm{r}\, n_\mathrm{X}(t) - k_\mathrm{nr}\, n_\mathrm{X}(t) - k_\mathrm{Auger}\, n_\mathrm{X}(t)^2 \tag{2.18}$$

Here, $k_\mathrm{r} = 1/\tau_\mathrm{r}$ and $k_\mathrm{nr} = 1/\tau_\mathrm{nr}$ denote the monomolecular radiative and non-radiative recombination rates, respectively. The third term, k_Auger, accounts for bimolecular Auger recombination, also called exciton–exciton annihilation.

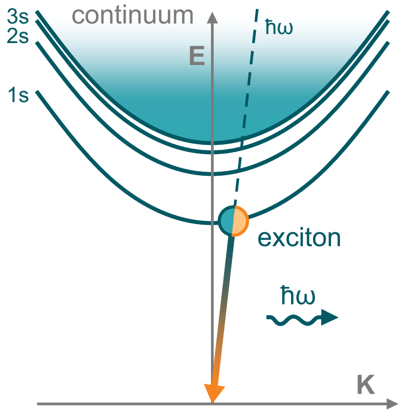

Figure 2.9: Radiative Recombination in the Two-Particle Picture. Radiative recombination of an exciton without the involvement of an additional particle is only possible at the intersection between the photon dispersion relation (dashed line) and the exciton energy levels (1s, 2s, ...). The origin corresponds to the exciton ground state.

Trap-Assisted Recombination

Monomolecular processes include both radiative and non-radiative trapping of an exciton in either shallow or deep trap states. In these processes, one charge carrier (either the electron or the hole) is captured by a localized defect state as schematically illustrated in Figure 2.10 a. Radiative recombination from a trap leads to the emission of a red-shifted photon, while non-radiative recombination involves phonon emission and results in energy loss without light emission. The likelihood of trap-assisted recombination depends on trap depth and density.

Auger Recombination and Biexcitons

The bimolecular term in the rate equation arises from exciton–exciton interactions. In the so-called biexciton Auger process, one exciton recombines and transfers its energy non-radiatively to a second exciton, which is excited into the continuum. The latter is effectively ionized into a free electron and hole, which subsequently cool and may form a new exciton (see Figure 2.10 b). Since biexciton Auger recombination probability scales quadratically with exciton density, it becomes increasingly relevant under high excitation powers or high exciton densities. This process is often discussed in the context of biexciton formation, where two excitons form a bound state analogous to a hydrogen molecule. While Auger processes do not necessarily require a stable biexciton to form, the probability of an Auger process closely correlates to the amount of biexcitons.

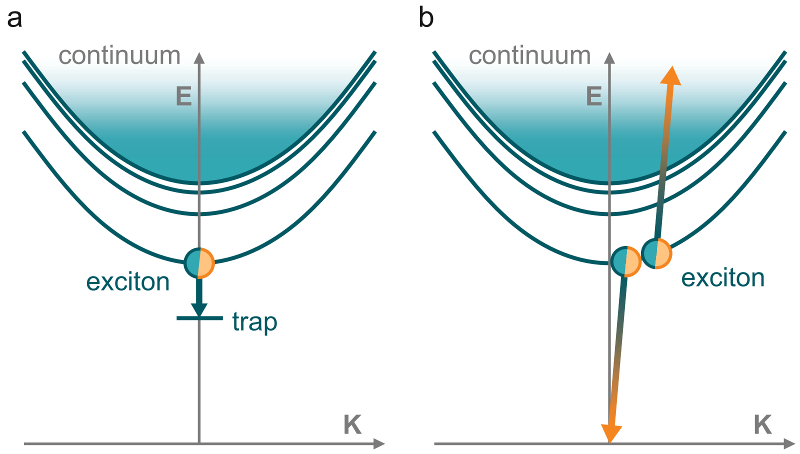

Figure 2.10: Non-Radiative Recombination Processes of Excitons. a) A trap state within the band gap, originating from a structural defect, can capture an electron or a hole. This trap-assisted recombination process reduces charge carrier mobility. **b)** Bimolecular recombination occurs via an Auger-like process involving two excitons, where one exciton recombines non-radiatively and transfers its energy to the other. The second exciton is thereby promoted into the continuum.

Trions

Another important quasiparticle is the trion or charged exciton. Trions form when an exciton binds to an additional free charge carrier. These charged species can be negative (X^-, two electrons + one hole) or positive (X^+, two holes + one electron). Trions are more likely to form in environments with excess free carriers (e.g., doped materials) or when excitons are long-lived or trapped in shallow states, which prevent their immediate recombination and facilitate interaction with other free carriers.

2.5 Transition from Bulk to Nanocrystals

Until this point, all processes from light absorption to recombination were discussed, assuming macroscopic or so-called bulk crystals. However, all experimental results presented in this work were obtained using nanocrystals, whose dimensions typically range from a few to a few hundred nanometers. In the following, the differences between bulk and nanocrystals are discussed, using lead halide perovskite nanocrystals as an example.

2.5.1 Perovskite Nanocrystals

In general, nanocrystals keep the same crystal structure as their bulk counterparts. The transition from bulk to nanoscale involves precise control over the crystal nucleation and growth processes. The basic principle for size control is the use of surface-active molecules in solution (called ligands or surfactants) to halt crystal growth at the desired crystal size. These molecules are designed in a way that they selectively bind to crystal facets, allowing them to not only determine particle size but also their shape and dimensionality. Once the crystal size approaches the exciton Bohr radius, quantum confinement effects emerge that significantly alter the electronic structure. A detailed description of the synthesis procedures used in this work is provided in Section 3.1.

2.5.2 Quantum Confinement Effect

Quantum confinement describes the effect of spatially restricting a quantum particle, which leads to quantization of its energy levels. In the case of semiconductor nanocrystals, this can be visualized using the particle-in-a-box model, where the allowed energy levels of a charge carrier become discrete and increase in energy as the size of the box, i.e., the nanocrystal size decreases. The strength of quantum confinement depends on the material-dependent exciton Bohr radius a_B, which depends on the dielectric constant ϵ and the effective masses of the electron and hole ($m^*_{\mathrm{e/h}}$). Depending on the nanocrystal size, literature often refers to terms like weak (crystal size > a_B) and strong confinement (crystal size < a_B). However, the boundary between both confinement regimes is not precisely defined and instead represents a smooth, continuous transition. The effects of quantum confinement on an exciton are increased band gap energy as well as an increase in the exciton binding energy. Furthermore, the separation of the discrete excitonic states becomes larger. These effects are illustrated in Figure 2.11.

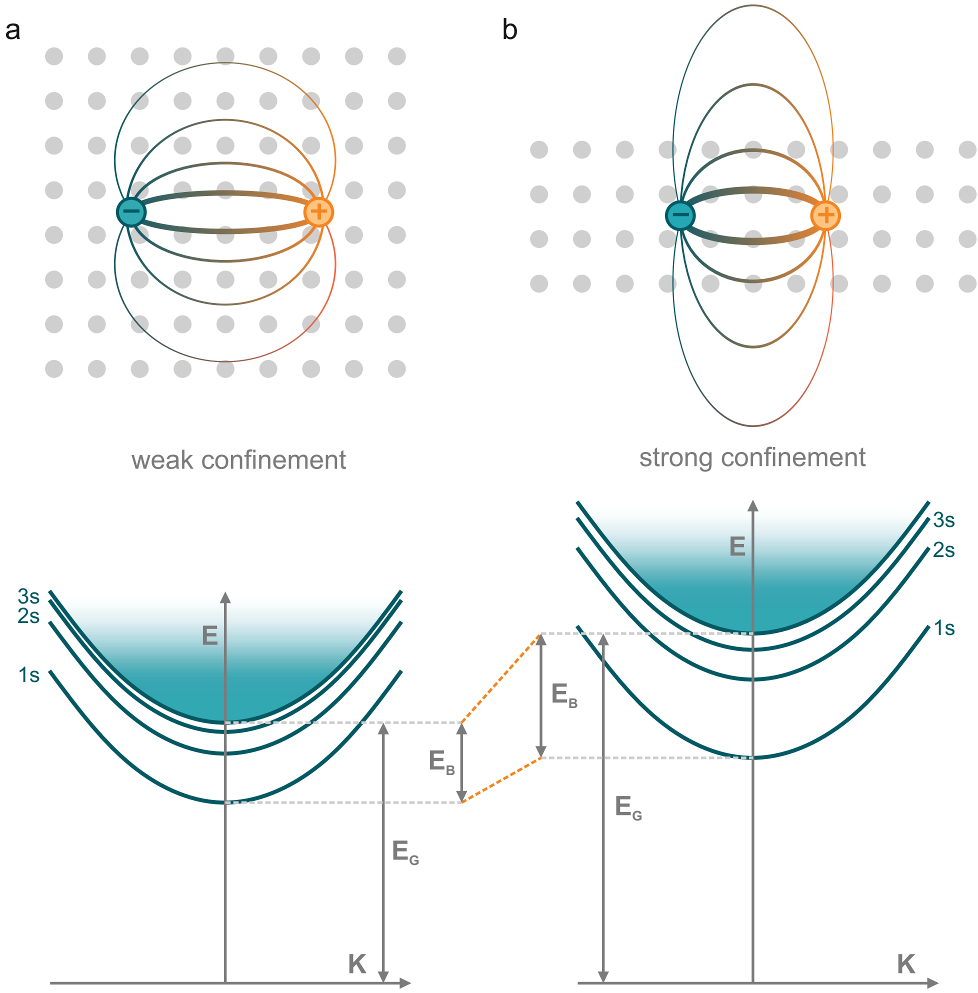

Figure 2.11: Quantum Confined Exciton. Schematic of an exciton with electric field lines between the electron and the hole in a crystal with weak (a) and strong (b) confinement. The dielectric screening decreases the exciton binding energy in the weakly confined crystal. The exciton dispersion relations with the corresponding exciton binding (E_B) and band gap energies (E_G) are shown below.

This spatial compression of the exciton has a pronounced influence not only on emission but also on absorption properties. While excitonic effects are already present in bulk, quantum confinement enhances these features' visibility and energy separation, particularly under strong confinement conditions. Additionally, the dielectric environment of a nanocrystal plays an increasingly important role. In bulk crystals, the surrounding medium contributes to strong dielectric screening, reducing the Coulomb interaction between electrons and holes. In confined systems, however, field lines can extend outside the crystal, effectively reducing the screening and further increasing the exciton binding energy. This effect is particularly pronounced in low-dimensional systems.[46–48]

2.5.3 Broadening of Optical Transitions

In the context of colloidal semiconductor nanocrystals, optical transitions such as absorption and PL are directly affected by the interplay between quantum confinement and various broadening mechanisms. Ideally, one would expect the PL emission to occur at a well-defined energy corresponding to the band gap, resulting in an extremely sharp spectral line. In reality, however, the absorption and PL spectra of semiconductor nanocrystals are broadened. These broadening mechanisms can be classified into homogeneous and inhomogeneous broadening. Figure 2.12 schematically shows the effects of both broadening mechanisms on a PL spectrum. Homogeneous broadening affects all nanocrystals equally and is typically temperature-dependent, while inhomogeneous broadening arises from structural or environmental differences between nanocrystals. At low temperatures, homogeneous contributions become minimal, making inhomogeneous broadening the dominant effect, especially in nanocrystal ensembles, where a specific size distribution is common.

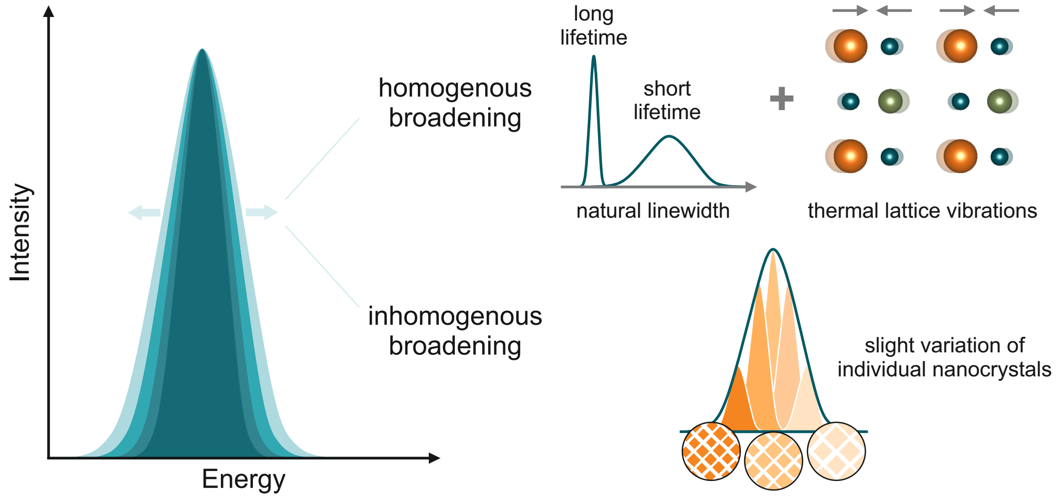

Figure 2.12: Homogenous and Inhomogenous Broadening. Schematic illustration of the broadening mechanisms responsible for the PL linewidth in a nanocrystal ensemble. Adapted from Reference [49]

Homogenous Broadening

Homogeneous broadening arises from intrinsic processes that similarly affect all nanocrystals. Even at absolute zero ($T = 0\,\mathrm{K}$), for example, the PL spectrum of an ideal emitter is not infinitely narrow. This minimal linewidth is known as the natural linewidth, which originates from the finite lifetime of spontaneous emission and is based on the Heisenberg uncertainty principle. This principle implies that the shorter the lifetime of the emitter, the greater the uncertainty in its energy, resulting in a larger PL peak width. Since the probability of spontaneous emission can be described by a time-dependent exponential decay, the corresponding PL lineshape, which is obtained via Fourier transformation, takes the form of a Lorentzian. Once temperature becomes non-zero, phonons arise due to thermal lattice vibrations. The interaction of phonons with charge carriers or excitons leads to slight shifts in the electronic band structure. These interactions introduce spectral broadening that affects all nanocrystals uniformly. As a result, homogeneous broadening increases with temperature and dominates in systems with strong charge carrier- or exciton–phonon coupling.

Inhomogenous Broadening

Inhomogeneous broadening refers to the widening of an emission or absorption line due to microscopic differences between individual nanocrystals. While an ideal, perfectly uniform crystal would not show signs of inhomogeneous broadening, real systems consist of slightly non-identical nanocrystals, each contributing a slightly different emission energy. When these individual spectra are added up, the result is a broadened ensemble spectrum. In the context of nanocrystals, inhomogeneous broadening is primarily caused by variations in size, shape, surface defects, or slight variations of the dielectric surrounding. As these factors affect the band structure and exciton confinement energy, each nanocrystal emits at a slightly different energy. The resulting ensemble PL spectrum is thus the sum of many slightly shifted emission peaks. Because these deviations tend to follow a normal distribution, this leads to a Gaussian lineshape, whose width reflects the degree of heterogeneity within the nanocrystal ensemble.

2.5.4 Tunable Morphology

Beyond size control, colloidal nanocrystals also allow precise tuning of their morphology. This refers to the number of spatial dimensions in which quantum confinement occurs, enabling the design of applications with tailored electronic and optical properties. Morphological control thus complements quantum size effects and expands the tunability of nanocrystal-based systems beyond what is possible in bulk semiconductors. Reducing a 3D bulk crystal along one axis leads to a 2D nanoplatelet or nanosheet, where confinement is strongest in the thickness direction. In such confined structures, the thickness is often measured in so-called monolayers (MLs), corresponding to the height of one unit cell. Further confinement in two directions results in 1D nanorods or nanowires, and fully confined systems with all three dimensions reduced are called 0D quantum dots.[50–53] Each morphology exhibits specific properties due to its confinement characteristics. 2D nanoplatelets, for example, show high exciton binding energies and efficient in-plane energy transfer, making them attractive for applications based on energy transfer or light-emitting devices.[54–56] 1D nanorods offer directional charge carrier mobility and polarized emission due to their anisotropic shape.[57–59] The synthesis of nanocrystals with defined shape and dimensionality, especially in the case of lead halide perovskites, is a complex and fast process, often completed within a few seconds. While factors like ligand concentration, precursor ratios, and temperature are considered the primary parameters for morphology control, recent studies suggest that the antisolvent properties, particularly its dipole moment and hydrogen bonding ability, play a more decisive role in directing the formation of nanorods or nanoplatelets.[9,60,61] The morphology not only determines the physical geometry of the nanocrystals but also crucially impacts their electronic structure and optical behavior, particularly through its influence on the DOS. As discussed in Subsection 2.2.1, the DOS determines how many electronic states are available for absorption at a given energy. In 3D crystals, the DOS increases with the square root of energy, $D(E) \propto \sqrt{E}$. In 2D systems, the DOS becomes a step function, remaining constant within each subband. In 1D systems, it has an inverse square root dependence on the energy, $D(E) \propto \frac{1}{\sqrt{E}}$ and in

0D quantum dots, the DOS reduces to a series of discrete δ-functions corresponding to quantized energy levels.[38] These dimensionality-induced changes in the DOS lead to pronounced modifications in the absorption spectrum. In strongly confined systems, the increased exciton binding energy causes excitonic resonances to appear below the continuum edge (compare Figure 2.8 b), which sharpens the absorption onset and makes it size- and morphology-dependent. Later sections will revisit this concept in the context of absorption cross-sections and morphology-dependent spectral properties.

2.5.5 Stability of Nanocrystals

Nanocrystals differ from their bulk counterparts not only in their optical and electronic properties but also in their chemical and structural stability. As discussed in Subsection 2.2.4, in bulk crystals, intrinsic defects such as halide or lead vacancies can form throughout the crystal lattice. In nanocrystals, defect formation is fundamentally different. One of the main reasons for this is their much higher surface-to-volume ratio, which increases the proportion of undercoordinated surface atoms. These sites are energetically less stable and more reactive, making the surface of nanocrystals vulnerable to degradation and defect formation. To stabilize the surface and control growth, organic ligands are typically used during synthesis. In the case of lead halide perovskites, the most commonly used ligands, oleic acid and oleylamine, bind only weakly to the nanocrystal surface. As a result, ligand binding becomes dynamic, leading to frequent desorption and reattachment.[62,63] Although ligands, in the first place, protect the nanocrystal surface, the dynamic binding can still expose the surface, facilitating aggregation and degradation.[12,62] Furthermore, defect formation in nanocrystals is closely linked to the chemical environment, particularly the dynamic equilibrium between the nanocrystal and its surrounding ligands and solvent molecules. For example, instead of a single-site Pb^{2+} vacancy, nanocrystals tend to release $PbBr_2$ pairs into solution. These surface defects are often harmless and create only shallow trap states. However, if surface passivation is incomplete and large amounts of ligands are removed, deeper traps can appear, strongly reducing the PLQY.[64]

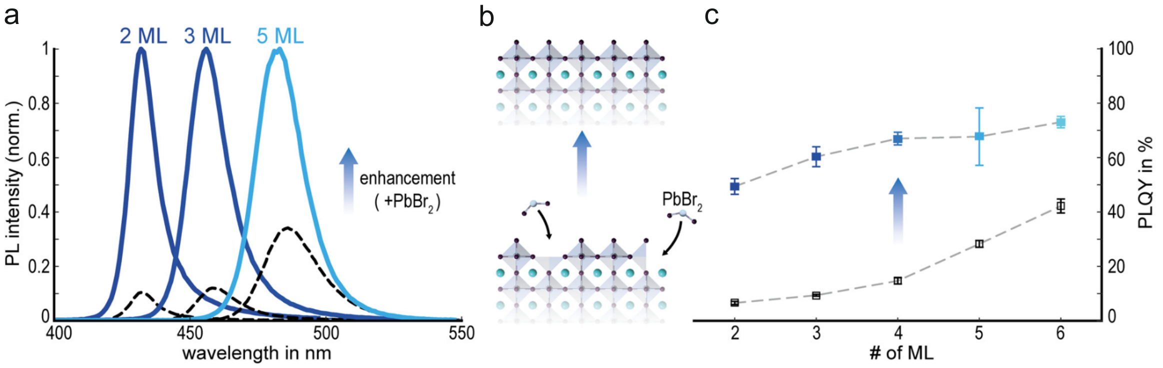

Figure 2.13: Nanoplatelet Surface Trap Repair Through Enhancement. **a)** PL spectra of $CsPbBr_3$ nanoplatelets with different thicknesses before (black dashed lines) and after adding $PbBr_2$ enhancement solution (colored lines). **b)** Schematic of how additional $PbBr_2$ repairs surface defects. **c)** Comparison of the PLQY of initial (gray) and enhanced (colored) $CsPbBr_3$ nanoplatelets with different thicknesses. Through surface repair, the PLQY is strongly increased. Adapted from Reference [47].

Postsynthetic Surface Trap Repair

A practical approach to improve the emission and stability of perovskite nanocrystals is the postsynthetic repair of surface defects.[65] Bohn et al. demonstrated that adding a $PbBr_2$-ligand solution to colloidal $CsPbBr_3$ nanoplatelets leads to a significant increase in PLQY – up to 73% for blue-emitting nanoplatelets.[47] The enhancement is attributed to the filling of the above-mentioned Br and Pb vacancies and passivation of undercoordinated surface atoms (see Figure 2.13). This treatment preserves morphology and thickness but transforms non-emissive subensembles into highly luminescent nanocrystals. The improvement correlates strongly with the surface-to-volume ratio, which means that thinner nanoplatelets are repaired more, indicating that surface defects are the limiting factor in thinner, more strongly confined nanoplatelets.

Encapsulated Nanocrystals

In addition to passivation via ligands or postsynthetic surface trap repair, physical encapsulation methods of nanocrystals like matrix embedding, core-shell structures, or polymer encapsulation offer an effective alternative to enhance the stability of nanocrystals against environmental stress.[66–69] In this work, polymer encapsulation was used to encapsulate lead halide perovskite nanocrystals. Figure 2.14 schematically depicts this encapsulation process with a diblock copolymer of two chemically distinct polymer segments. When dissolved in a polar solvent, the polymer molecules spontaneously self-assemble into micelles once their concentration exceeds a threshold known as the critical micelle concentration (CMC). At this point, the solvent-compatible block forms the outer shell of the micelle, while the solvent-incompatible block aggregates to create the micelle core. In the system used in this work, the diblock copolymer polystyrene-b-poly(2-vinylpyridine) (PS-*b*-P2VP) is employed. The PS segment interacts favorably with the solvent (toluene) and constitutes the micelle shell, while the P2VP segment forms the inner core. These micelles serve as confined nanoreactors within which perovskite nanocrystals can nucleate and grow under controlled conditions. Adjusting the monomer number of both polymer blocks allows both core size and shell thickness to be tuned, allowing high versatility for many different use cases.

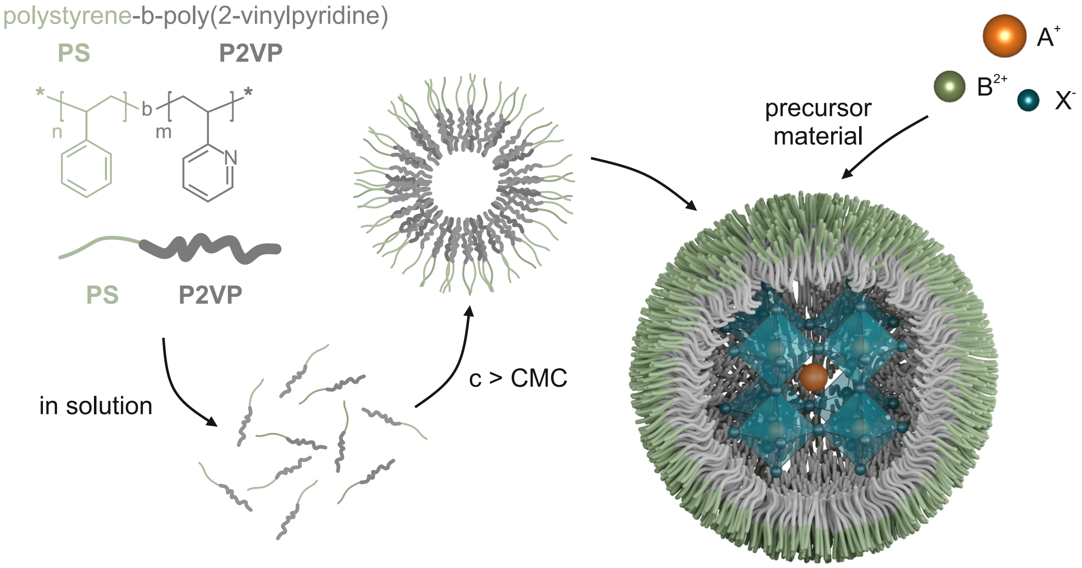

Figure 2.14: Micellization Process. Chemical structure of the PS-*b*-P2VP diblock-copolymer and schematic illustration of the micellization process. Once the polymer concentration exceeds the CMC, micelles form, into which the precursor material diffuses and subsequently crystallizes.

2.6 Energy Transfer in Nanocrystal Ensembles

Energy transfer describes many different processes, including the propagation of electromagnetic radiation, heat conduction, and the transmission of kinetic energy during particle collisions. Despite this wide range of transfer mechanisms, these processes share a common structure: they require a donor, which releases energy, and an acceptor, which receives it. Between nanocrystals, energy transfer is mainly restricted by the physical separation due to insulating shells such as ligand layers or encapsulating polymers. As a result, energy transfer via direct collisions or charge carrier transport, as observed in bulk crystals or metals, is suppressed. In principle, radiative energy transfer can occur via photon emission and reabsorption, but this process is only efficient at high particle concentrations. Instead, the dominant mechanism in nanocrystal ensembles is a non-radiative dipole-dipole interaction, commonly referred to as Förster resonance energy transfer (FRET). Since this work focuses on energy transfer between nanocrystals, FRET is explained in detail below. Other mechanisms such as Dexter transfer, carrier tunneling, or radiative reabsorption are only relevant under different distance and particle concentration and are therefore not discussed further.[70,71]

2.6.1 Förster Resonance Energy Transfer

FRET is a non-radiative dipole-dipole interaction between an excited donor and a ground-state acceptor.[72] While initially observed between organic dye molecules, FRET has been widely demonstrated in semiconductor nanocrystals, including CdSe and $CsPbBr_3$.[55,56,73,74] One of the essential prerequisites for FRET is a spectral overlap between the emission spectrum of the donor and the absorption spectrum of the acceptor (see Figure 2.15 a). Once this condition is fulfilled, the exciton energy of the donor nanocrystal can be transferred non-radiatively to a nearby acceptor nanocrystal. To describe this process quantitatively, the decay rate of an excited donor k_D, previously defined as the sum of radiative and intrinsic non-radiative components (see Subsection 2.4.3), must be expanded by an additional third term:

$$k_\mathrm{D} = k_\mathrm{r} + k_\mathrm{nr} + k_\mathrm{FRET} \tag{2.19}$$

Here, k_FRET describes the non-radiative FRET to an acceptor. This rate itself can be expressed as:

$$k_\mathrm{FRET} = \frac{9c^4\kappa^2}{8\pi n^4 \tau_\mathrm{D}} \frac{1}{r^6} \int_0^\infty \frac{f_\mathrm{D}(\omega)\sigma_\mathrm{A}(\omega)}{\omega^4} d\omega \tag{2.20}$$

This equation includes the spectral overlap integral (where f_D is the integral-normalized PL spectrum of the donor and σ_A the absorption cross-section of the acceptor), the refractive index of the medium n, the donor PL lifetime τ_D, the dipole orientation factor κ^2, and the donor-acceptor separation r. In practice, this equation is often simplified by introducing the Förster radius R_0, which is defined as the distance at which the FRET efficiency reaches 50%. The rate can then be rewritten as:

$$k_\mathrm{FRET} = \frac{1}{\tau_\mathrm{D}} \left(\frac{R_0}{r}\right)^6 . \tag{2.21}$$

The Förster radius typically lies between $2-10\,\mathrm{nm}$ for typical donor-acceptor systems, so FRET is the predominant energy transfer mechanism at these distances (see Figure 2.15 b). Note, however, that the distance dependence of the FRET rate follows a $1/r^6$ scaling only for a point-like acceptor. If the acceptors are distributed over a 2D plane, the dependence decreases to $k_{\mathrm{FRET}} \propto 1/r^4$ and for a 3D bulk distribution it is equal to $k_{\mathrm{FRET}} \propto 1/r^3$.[75]

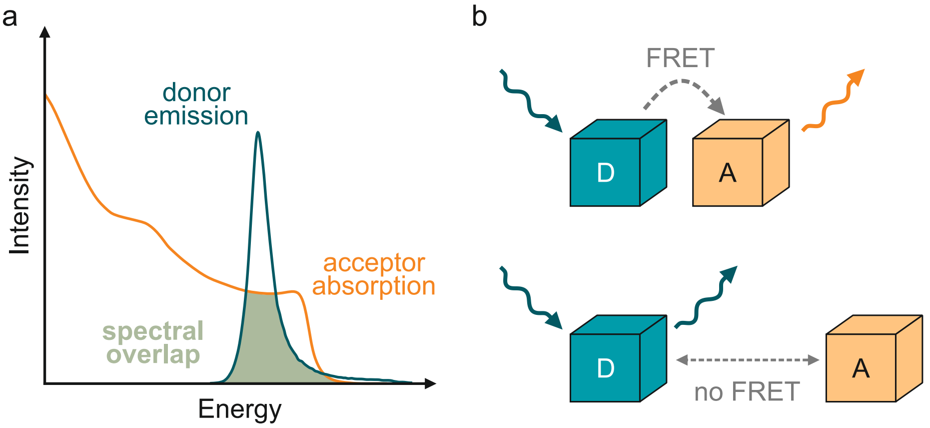

Figure 2.15: Spectral Overlap and FRET. a) Emission spectrum of a donor and absorption spectrum of an acceptor illustrating the spectral overlap required for FRET. **b)** Schematic representation of the distance dependence of FRET. If the donor-acceptor separation exceeds a critical distance, energy transfer cannot occur.

In typical experiments, the Förster radius is not determined directly. Instead, FRET is commonly detected and compared via its efficiency, representing the fraction of donor excitations that lead to FRET. It can be defined either via the decay rates or, equivalently, via the measured donor PL lifetimes:

$$\eta_{\mathrm{FRET}} = \frac{k_{\mathrm{FRET}}}{k_{\mathrm{r}} + k_{\mathrm{nr}} + k_{\mathrm{FRET}}} = 1 - \frac{\tau_{\mathrm{DA}}}{\tau_{\mathrm{D}}} \tag{2.22}$$

where τ_{DA} is the donor PL lifetime in presence of acceptors. This expression provides both a theoretical framework and an experimentally accessible parameter, making it the most common figure of merit when evaluating FRET in nanocrystal systems.

3

Materials and Methods

Having established the fundamental principles in the previous chapter, this chapter introduces the materials and methods employed throughout this thesis. Nanocrystals were synthesized via three distinct routes, each chosen to access specific sizes and morphologies relevant for the optical investigations. Morphological characterization was carried out using electron and atomic force microscopy, providing detailed structural information on the synthesized nanocrystals. Various experimental setups were used to investigate the optical properties of these materials. A commercial spectrofluorometer enabled steady-state photoluminescence studies, while a micro-photoluminescence setup based on a pulsed white light laser allowed for spatially and temperature-resolved measurements. Ultrafast spectroscopic techniques such as transient absorption and fluorescence upconversion spectroscopy were employed to probe dynamic processes on femtosecond timescales. Additionally, cavity-enhanced extinction spectroscopy, used within the framework of a collaboration, is introduced as a specialized method to measure absorption with extremely high sensitivity.

3.1 Nanocrystal Synthesis

The synthesis of nanocrystals marks the first step in tailoring their physical and optical properties. As subtle changes in size, shape, or surface chemistry can drastically alter their behavior, choosing the appropriate synthetic route is essential. The most important approaches used for nanocrystals investigated in this work will be explained in the following. This includes ligand-assisted reprecipitation (LARP), synthesis via hot-injection, and synthesis of nanocrystals inside diblock copolymer micelle nanoreactors. Each method has its advantages and limitations, and was chosen to produce specific types of nanocrystals. All methods are generally based on mixing precursor solutions, which typically consist of salts (e.g., cesium carbonate, lead(II) bromide, or methylammonium bromide) dissolved in a solvent (hexane or toluene) and optionally stabilizing ligands (oleic acid and oleylamine). In essence, salts and ligands are driven to form nanocrystals, and if needed, the reaction is quenched once the desired nanocrystal size is reached. A subsequent purification step, such as centrifugation or filtering, is usually performed to isolate the nanocrystals. This helps to remove unwanted residues like excess ligands, unreacted precursors, and residual solvent. By varying the precursor volumes and ratios, or in the case of the LARP method, the type of antisolvent, the morphology, and size of the nanocrystals can be tuned. Detailed information is provided in the specific synthesis description for each nanocrystal type. All nanocrystals used for this thesis were kindly synthesized by my colleagues Carola Lampe, Nina A. Henke, Patrick Ganswindt, Anna Abfalterer, and Jonathan Paul. The chemicals used are listed in Table 3.1.

Table 3.1: Chemicals Required for the Syntheses. All chemicals were purchased from the reference supplier and used as received. If the chemical formula of a compound is too long to be written down conveniently here, it is omitted.

Material	Chemical Formula	Purity	Supplier
cesium carbonate	Cs_2CO_3	99.9%	Sigma-Aldrich / VWR Chemicals
lead(II) bromide	$PbBr_2$	$\geq$ 98%	Sigma-Aldrich / VWR Chemicals
methylammonium bromide	CH_3NH_3Br	98%	Ossila
polystyrene-b-poly(2-vinylpyridine)	PS-*b*-P2VP	-	Polymer Source Inc
oleic acid (OA)	$C_{18}H_{34}O_2$	technical grade, 90%	Thermo Scientific
oleylamine (OLA)	$C_{18}H_{35}NH_2$	technical grade, 70%	Sigma-Aldrich / VWR Chemicals
toluene	C_7H_8	99.9%	VWR Chemicals
n-hexane	C_6H_{14}	97%	VWR Chemicals
methanol	CH_3OH	$\geq$ 99.8%	Sigma-Aldrich
ethanol	C_2H_5OH	99.5%	Sigma-Aldrich
isopropanol	C_3H_8O	for analysis	Merck
n-butanol	$C_4H_{10}O$	99%	Sigma-Aldrich
cyclopentanone	C_5H_8O	for synthesis	Merck
methyl acetate	CH_3COOCH_3	99%, for synthesis	Merck
acetone	CH_3COCH_3	for HPLC, $\geq$ 99.9%	VWR Chemicals
1-octadecene	$C_{18}H_{36}$	for synthesis	Sigma-Aldrich

Hot-Injection

The hot-injection method is one of the most widely used techniques for synthesizing nanocrystals.[4,7,76] As the name suggests, it is carried out at high temperatures and in an inert atmosphere. A precursor-ligand mixture is prepared in a solvent, while a high-boiling-point solvent combined with ligands is heated to a specific temperature. As the name suggests, the precursor-ligand solution is rapidly injected into the hot solvent under constant stirring. This triggers nucleation, which can be further controlled by adjusting the reaction temperature or duration. To stop the reaction, the mixture can be cooled, for instance, by immersion in a water bath. The nanocrystals are separated from the reaction mixture and purified by centrifugation. The hot-injection method results in nanocrystals with high homogeneity and allows for precise control of nanocrystal characteristics by varying the reaction parameters, such as temperature.

Ligand-Assisted Repricipitation

In contrast to the hot-injection method, the LARP method can be performed at RT and requires less specialized equipment. The LARP method relies on solvent polarity instead of temperature to induce nucleation.[77,78] Precursor salts and ligands are dissolved in a solvent to form a homogenous mixture. The nucleation is triggered by adding a polar antisolvent, causing the nanocrystals to precipitate instantly, hence the name. The resulting nanocrystals are purified through centrifugation. Instead of triggering the nucleation via polarity differences, it is also possible to use ultrasonic waves locally produced by a tip-sonicator.[79] These high-energy waves create localized pressure and temperature changes that initiate crystallization. As before, the final purification step is centrifugation. Furthermore, it is also possible to grow nanocrystals without ligands via a diblock copolymer templated synthesis.[80] As described in Section 2.5.5, the polymer is dissolved in a nonpolar solvent, and micelles are formed due to the polymer's structure. The precursor salts diffuse into the cores, and due to an altered solubility, spontaneous crystallization takes place. The polymer shells additionally stabilize the resulting nanocrystals against degradation.[69]

$PbBr_2$ Enhancement Solution

As explained in Section 2.5.5, the surface treatment of nanocrystals is a common post-synthetic improvement step. When referring to an enhancement solution, this denotes a mixture of $PbBr_2$ and ligands (OLA, OA). As demonstrated in a previous study by Bohn et al., adding an enhancement solution to nanocrystals post-synthesis significantly reduces surface defects. This, in turn, enhances their optical properties.[47]

3.1.1 $CsPbBr_3$ Nanocubes

The $CsPbBr_3$ nanocubes were synthesized via the hot-injection method following the protocol of Bodnarchuk et al.[81] and the tip-sonication method following the work by Tong et al.[79] For nanocrystals synthesized by hot-injection, $PbBr_2$ (0.220 g) was suspended in 1-octadecene (ODE) (20 mL) and heated to 100 °C under vacuum (approximately 0.17 mbar) with a stirring speed of 1100 rpm. The indicated temperature was measured using a thermocouple inside a thermocouple glass adapter that reached into the reaction mixture. The thermocouple glass adapter was filled with 150 µL ODE. Once the reaction mixture reached 100 °C, it was dried under vacuum for 15 min. The atmosphere was then switched to nitrogen, and the temperature increased to 110 °C. Dried OLA (2.0 mL) and dried OA (2.0 mL) were injected into the reaction mixture. Once the $PbBr_2$ was fully dissolved, the solution was heated to 180 °C. The clear cesium oleate solution (2.8 mL, 100 °C) was injected into the solution inside the reaction flask. After 15 s, the reaction mixture was cooled using a water-ice bath, with stirring discontinued during cooling. Once cooled, the flask was disconnected from the Schlenk line, and

5 mL of the crude solution was transferred in air into a centrifuge tube. The tube was centrifuged at 11 000 rpm for 5 min (centrifuge: Rotina 380R from *Hettich*). The supernatant was discarded, and the precipitate was gently rinsed with 1.0 mL of toluene, after which the toluene was discarded. The precipitate was redispersed in either toluene or hexane (0.30 mL) and centrifuged at 11 000 rpm for 5 min. The supernatants were transferred into glass vials and diluted with the same solvent as used before (0.30 mL). For nanocrystals synthesized by tip-sonication ODE (10 mL) was thoroughly mixed with OLA (0.5 mL) and OA (0.5 mL), then Cs_2CO_3 (0.1 mmol, 32.58 mg) and $PbBr_2$ (0.3 mmol, 110.1 mg) were added. The reaction mixture was immediately subjected to tip-sonication (90% amplitude for 8 min, followed by 95% amplitude for 2 min, Sonopuls HD 2070 with a Sonopuls MS73 titanium probe, *Bandelin*). The resulting crude nanocrystal dispersion was then centrifuged at 10 614 g for 10 min, and the supernatant was discarded to remove the remaining unreacted precursor material. The yellow precipitate, containing $CsPbBr_3$ material, was redispersed in toluene (5 mL) and centrifuged at 524 g for 10 min a second time to separate both $CsPbBr_3$ bulk material and larger nanocrystals. The precipitate was discarded, and the supernatant, containing cube-shaped $CsPbBr_3$ nanocrystals, was retained. To this, 50 µL of $PbBr_2$-enhancement solution (0.01 M) was added to repair surface defects and improve the stability and PLQY of the $CsPbBr_3$ nanocrystals.

3.1.2 $CsPbBr_3$ Nanorods, Nanoplatelets, and Small Nanocubes

Nanorods, nanoplatelets, and small nanocubes were synthesized via the LARP approach. During the period of this thesis, the general understanding of the synthesis of anisotropic nanocrystals changed. This means that especially nanoplatelets and nanorods were synthesized following different protocols depending on the time of the respective project. From being based on the synthesis protocol used by Bohn et al., where the ratio of the two precursor solutions was primarily thought to be responsible for the thickness of the resulting nanoplatelets, the general understanding changed with the results of the work of Frank and Henke et al. The antisolvent was found to play a more important role in determining the outcome of the size and shape of the nanocrystals.[47,61,82] While for the work on energy transfer Chapter 6, nanocrystals were synthesized based on the method of Bohn et al., all nanocrystals used for the absorption cross-section study (Chapter 4) were synthesized, with the aid of the newly acquired understanding from Frank and Henke et al. As the following section only provides an overview of the synthesis procedure and parameters, the reader is advised to consult the respective references on which the synthesis is based.

Cs – OA precursor solutions with concentrations of 0.02 M, 0.07 M, 0.08 M, and 0.10 M were prepared by dissolving 0.10 mmol, 0.35 mmol, 0.40 mmol, and 0.50 mmol of Cs_2CO_3 (corresponding to 32.58 mg, 114.0 mg, 130.3 mg, and 162.9 mg, respectively) in 10 mL of OA. This mixture was stirred continuously at 85 °C on a hotplate for 2 – 3 h until a clear solution was obtained. For the $PbBr_2$ precursor solution at 0.01 M, 0.1 mmol of $PbBr_2$ (36.7 mg) was dissolved in 10 mL of toluene along with 100 µL of OLA and 100 µL of OA. This solution was stirred continuously at 85 °C on a hotplate for 2 – 3 h until it became clear. The $PbBr_2$ enhancement solution, at 0.01 M, was prepared by dissolving 0.1 mmol of $PbBr_2$ (36.7 mg) in 10 mL of n-hexane, with the addition of each 100 µL of OLA and OA. The solution was stirred at 85 °C for 2 – 3 h on a hotplate until it became clear. For the synthesis, a glass vial was charged with the $PbBr_2$ precursor solution and stirred vigorously at RT. The Cs – OA precursor solution was added at $t = 0$ s followed by the injection of the antisolvent at $t = 10 - 15$ s. The reaction mixture was stirred at RT until it became opaque and nanocrystal precipitation was observed. The vial was then removed from the stirring plate. Purification of nanoplatelets and nanorods involved transferring the reaction mixture to a 15 mL Falcon tube. Centrifugation was performed at 4000 rpm (2097 g) for 3 min, and the supernatant was discarded. The precipitate was redispersed in 2 mL of n-hexane, and 25 µL of the enhancement solution was added to improve colloidal stability and enhance the PLQY.[47] For the purification of small nanocubes, the reaction mixture was centrifuged at 4000 rpm (2097 g) for 3 min, and the precipitate was discarded while retaining the supernatant. Small nanocubes were precipitated from the supernatant by adding methyl acetate in a 1:2 volume ratio of nanocrystal to methyl acetate. The mixture was centrifuged at 4000 rpm (2097 g) for 3 min, and the precipitate was redispersed in 2 mL of n-hexane. To enhance colloidal stability and PLQY, 25 µL of the enhancement solution was added.

3.1.3 Encapsulated Nanocrystals

The synthesis for encapsulated nanocrystals is based on the work of Hintermayer et al.[69] For the work presented here, they were synthesized using different diblock copolymers. These polymers consist of two different parts: a PS and a P2VP part. The PS part comprises the shell, and the P2VP part creates the core of the micelles. The micellization process is described in Section 2.5.5. For the typical synthesis 1.56×10^{-6}mol of PS-*b*-P2VP was dissolved in 5 mL toluene at RT and stirred overnight. Then 6.4×10^{-5}mol of MABr precursor was added to the polymer solution and stirred for at least 5 h. In the next step 6.4×10^{-5}mol of $PbBr_2$ was added and stirred for at least 24 h. For purification, the mixture was transferred into a 15 mL Falcon tube and centrifuged at 5000 rpm (3277 g) for 10 min (Rotina 380R, *Hettich*). The supernatant was collected and centrifuged again at 12 000 rpm (18 873 g) for 20 min.

3.2 Sample Preparation

Nanocrystals are typically stored as a colloidal dispersion after synthesis. Depending on the nanocrystal property of interest, it is advantageous to measure nanocrystals either in dispersion or prepare them as a dry thin film on a substrate. Nanocrystals in dispersion have large interparticle distances, limiting interactions between individual nanocrystals. Furthermore, the long-term stability of the nanocrystals increases due to reduced exposition to air. The solvent, for example, facilitates heat dissipation, reducing the likelihood of laser-induced degradation. Depositing nanocrystals onto a substrate offers characterization that is impossible in dispersion. As the solvent evaporates, nanocrystals self-assemble into structured arrangements, allowing for interparticle interactions such as energy transfer. However, the increased surface exposure also makes the nanocrystals more susceptible to environmental stress, rendering them more volatile. Measurements on thin films further enable experiments at very low temperatures, which would be considerably more complex in dispersion.

For nanocrystal measurements in dispersion, the pure or diluted sample is prepared in a cuvette with a specific path length (2 mm or 10 mm). For thin film measurements, nanocrystals must first be deposited onto a substrate using one of three different techniques: drop casting, spin coating, or dip coating. For drop casting, a defined volume of nanocrystal dispersion is applied to a substrate and left to dry, resulting in thick but inhomogeneous films. Spin coating involves the rapid rotation of the substrate using a spin coater (WS-650MZ-23NPPB, *Laurell Technologies*) while the nanocrystal dispersion is applied during (dynamic) or prior (static) to spinning, producing thinner and more homogeneous films. Finally, for dip coating, the substrate is immersed in the nanocrystal dispersion and then pulled out at a controlled angle and constant velocity. This process leads to the formation of a thin film on the substrate surface due to the adhesion of nanocrystals to the substrate. A drawback of this method is that the coating forms on both sides of the substrate.

For thin film measurements, the choice of substrate is crucial. Usual types include 10 × 10 mm silicon substrates with a 300 nm oxide layer (*Siegert Wafer*), preventing charge carrier injection into the substrate (from hereon referred to as silicon substrates) and silicon dioxide, quartz or sapphire glass substrates (*Thermo Fisher Scientific*), which offer transparency and, in the case of sapphire, decreased absorbance of ultraviolet (UV) light and strongly increased chemical resistivity. To ensure cleanliness, all substrates were subjected to a four-step cleaning procedure consisting of immersion in solvents within an ultrasonic bath for 10 min per step. The substrates were sequentially cleaned in Hellmanex solution (diluted with milliQ water by a factor of 200), distilled water, acetone, and isopropanol. Afterward, they were stored in isopropanol until further use. Immediately prior to film deposition, they were treated in a plasma cleaner (Femto, *Diener electronic*) for 10 min to remove any remaining organic residues. Since sapphire substrates are costly, they were not discarded after use but subjected to an extended cleaning procedure. In addition to the standard solvent-based ultrasonic cleaning steps, the already used sapphire substrates were manually wiped with acetone to remove residual nanocrystals. Subsequently, they were submerged in 5% sulfuric acid for at least 24 h to dissolve the remaining nanocrystals and ligand residues, ensuring their reusability.

3.3 Morphological Characterization

Besides a quick check of the PL with a UV lamp, one of the first characterization methods after the synthesis is mostly morphological characterization via electron or atomic force microscopy (AFM). These imaging methods give information about the shape and the size of the nanocrystals. Both methods are explained in the following.

3.3.1 Electron Microscopy

For this study, both transmission electron microscopy (TEM) and scanning electron microscopy (SEM) were employed to analyze nanocrystals, as both techniques utilize accelerated electrons for imaging but offer distinct advantages. TEM, which was performed using a JEOL JEM-1100 operated at an acceleration voltage of 80 kV, provides high resolution and is suited for size measurements, such as determining nanocrystal side lengths (Figure 3.1 a). However, the nanocrystals must be prepared on specialized TEM grids made from copper coated with a thin layer of formvar and carbon (FF400-CU, *Electron Microscopy Sciences*). Unfortunately, the use of these specialized substrates makes further spectroscopic characterization very difficult. In contrast, SEM does not require electron transmission and can be performed directly on the above-mentioned standard silicon substrates (Figure 3.1 b). This allows further investigation of the same sample areas with complementary characterization techniques. SEM imaging was carried out using a SEM Ultra Plus from *ZEISS* with an acceleration voltage of 3 kV.

3.3.2 Atomic Force Microscopy

AFM can also be employed when morphological information is required, as it offers a non-destructive alternative to electron microscopy techniques. Unlike TEM and SEM, where the electron beam can potentially alter or degrade the sample, AFM relies on mechanical surface probing and thus preserves the material (Figure 3.1 c). Additionally, AFM imaging can be performed directly on standard silicon substrates. AFM imaging was conducted using a JPK NanoWizard ULTRA Speed 2 from *Bruker* in tapping dry mode, with *Bruker* TESPA-V2 AFM tips. Further parameters, such as gain, speed, and scanning resolution, were adjusted as needed to optimize image quality. AFM is more complicated to set up and takes longer than SEM and TEM. Therefore, TEM and SEM were used as the preferred imaging methods.

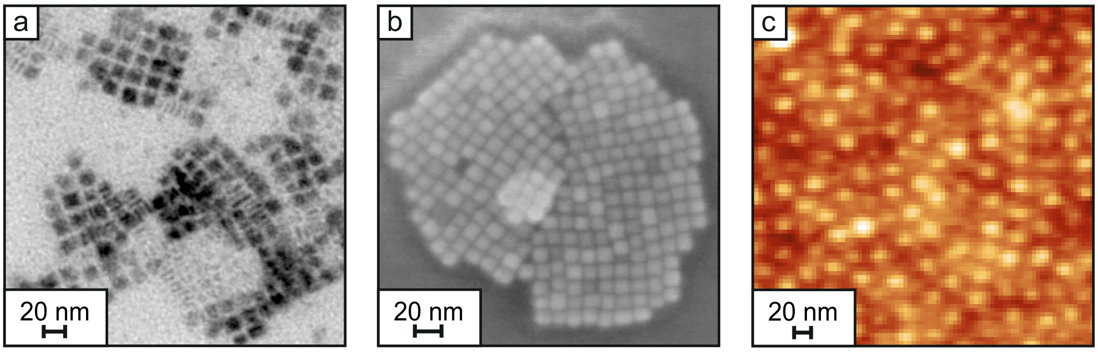

Figure 3.1: Examples Images of TEM, SEM, and AFM. a) Example TEM image of $CsPbBr_3$ nanoplatelets. **b)** Example SEM image of $CsPbBr_3$ nanocubes. **c)** Example AFM image of $MAPbBr_3$ encapsulated nanocrystals.

3.4 Optical Characterization

Apart from the morphological analysis of the nanocrystals, the optical properties are also fundamental. The two most basic but important characterization methods are linear absorption and steady-state PL measurements. A commercial FluoroMax-4Plus spectrometer equipped with a xenon arc lamp and an F-3031 transmission accessory (*HORIBA Scientific*) was used as a general and fast way to analyze these two properties. This setup allows for dispersion as well as thin film measurements.

3.4.1 Linear Absorption

Linear absorption measurements can determine the wavelength-dependent optical density $OD(\lambda)$ or absorbance $A(\lambda)$ of nanocrystal dispersions. Here, $A(\lambda)$ is obtained by measuring the transmitted light intensity $I(\lambda)$ relative to the incident light intensity $I_0(\lambda)$, using a solvent-filled cuvette as a reference. The relation between $A(\lambda)$ and transmittance $T(\lambda)$ is given by:

$$T(\lambda) = \frac{I(\lambda)}{I_0(\lambda)}, \quad A(\lambda) = OD(\lambda) = -\log_{10}(T(\lambda)) \tag{3.1}$$

When measuring absorption spectra, it is important to ensure that the OD remains below a threshold to avoid reabsorption effects. Reabsorption occurs when photons emitted by the sample are re-absorbed before exiting. The term “linear absorption” consequently refers to the regime where A scales linearly with concentration and path length (see Equation 2.11 and Equation 2.12), which is only valid when reabsorption and other higher-order effects are negligible. To ensure reliable measurements, the *OD* in the relevant spectral region was consistently kept between 0.1 and 1 throughout all experiments conducted in this work.

3.4.2 Steady-State Photoluminescence

In addition to absorption measurements, steady-state PL is another tool for assessing the quality of nanocrystals. As explained in Subsection 2.5.2, quantum confinement significantly influences the bandgap. This directly affects the PL emission maximum. Therefore, nanocrystals show characteristic PL peak positions depending on their quantum confinement. If a PL spectrum displays multiple peaks or a primary peak with a shoulder, it often indicates poor size homogeneity within the sample. Typically, the PL intensity in a spectrometer is measured in terms of constant wavelength intervals. However, since the relationship between energy and wavelength is nonlinear, converting the PL spectrum from wavelength to energy requires knowledge of the Jacobian conversion of scales, explained in detail below.

Jacobian Conversion of Scales

The relation between the wavelength and energy of a photon is given by:

$$E_{\mathrm{ph}} = \frac{hc}{\lambda} \tag{3.2}$$

where h is the Planck's constant, c is the speed of light and λ is the wavelength of the photon. Due to the energy conservation law, the intensities are connected as follows:

$$I(E)dE = I(\lambda)d\lambda \tag{3.3}$$

Combining these expressions results in:

$$I(E) = I(\lambda)\frac{d\lambda}{dE} = I(\lambda)\frac{d}{dE}\left(\frac{hc}{E}\right) = -I(\lambda)\frac{hc}{E^2} \tag{3.4}$$

Here, the negative sign indicates the direction of integration. The factor $\frac{hc}{E^2}$ shows the nonlinear relationship of both intensities, which must be considered when switching from units of wavelength to units of energy. For a detailed explanation see Reference [83].

3.5 Temperature-Dependent Photoluminescence Microscopy

For PL microscopy, two different self-built setups are used, which are structurally similar, with the primary distinction being that, for one, the sample is positioned inside of a closed-cycle helium cryostat (attoDRY800, *attocube*), allowing it to be cooled down to 9 K. They are from now on referred to as RT and cryogenic micro-PL setup. Compared to the commercial spectrofluorometer described earlier, these setups offer spatial resolution and precise temperature control. A schematic representation of the cryogenic micro-PL setup is shown in Figure 3.2. The setup consists of two main areas: the excitation section, where the fiber-coupled laser entering the setup is expanded and directed onto the sample, and the emission section, where the PL signal is guided to either the spectrometer or the Single-Photon Avalanche Diode (SPAD, MPD-SPAD-100 from *Micro Photon Devices* for the RT micro-PL setup and SPCM-AQRH from *Excelitas Technologies* for the cryogenic micro-PL setup). All optical and mechanical components, including lenses, mirrors, and mounts, were purchased from *Thorlabs*, while dichroic mirrors and optical filters were obtained from *Semrock* or *Chroma Technology*. The RT micro-PL setup features two interchangeable objectives with different magnifications (20x and 100x, Plan-Apochromat 20x/0.8, *ZEISS* and CFI-TU-Plan-Apo-Epi 100x, *Nikon*), whereas the cryogenic micro-PL setup utilizes a vacuum objective (EC Epiplan-Neofluar 100x/0.9 NA DIC Vac M27, *ZEISS*) mounted inside the cryostat. The objective focuses the laser beam to a diffraction-limited Gaussian profile on the sample. A three-axis translation stage allows precise positioning of the sample. The RT micro-PL setup uses a Q-521 Q-Motion from *Physik Instrumente*. The cryogenic micro-PL setup has a piezo-controlled stage (*attocube*), allowing movement at low temperatures. A thermal bridge between the cryostat's cold plate and the sample holder facilitates cooling to 9 K, while an integrated heater can raise the temperature to 300 K.

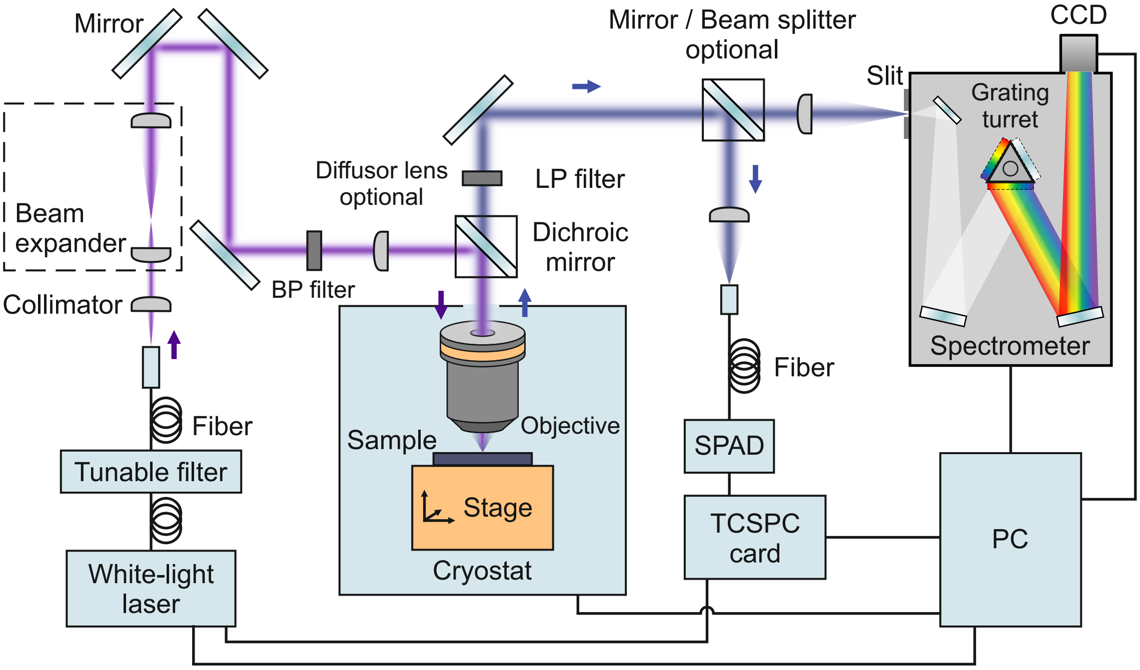

Figure 3.2: Micro-PL Setup. Schematic of the cryogenic micro-PL setup, which also applies to the RT micro-PL setup when the cryostat is omitted. The main optical components, like mirrors and lenses, bandpass (BP) and longpass (LP) filters, as well as measurement instruments are shown, with the laser path indicated in purple and the PL signal path in blue.

3.5.1 White Light Laser

The excitation source is a pulsed white light laser (SuperK FIANIUM FIU-15, *NKT Photonics*) with a pulse duration below 200 ps and a tunable repetition rate between 0.3 MHz and 77 MHz. A SuperK VARIA tunable filter (*NKT Photonics*) allows selecting output wavelengths between 400 nm and 840 nm with a spectral bandwidth adjustable between 10 nm and 100 nm. The laser is fiber-coupled, enabling its use in both the RT and the cryogenic micro-PL setup. The white light is generated inside a specially designed photonic crystal fiber (PCF). The fiber consists of a pure silica core surrounded by a regular hexagonal array of air holes. By engineering the size and spacing of these air holes, the refractive index profile along the radial axis can be tuned to ensure that only the fundamental Gaussian mode is guided over a broad spectral range, maintaining excellent beam quality. The small core diameter strongly confines the pump light of the seed laser (78 MHz), resulting in increased optical intensity and thus converting the fiber core into a highly nonlinear medium. This leads to the generation of a pulsed broadband supercontinuum that appears as white light at the fiber output. After exiting the tunable filter, the beam is collimated and expanded. A motorized continuous neutral density filter wheel (NDM4, *Thorlabs*) attenuates the laser intensity by reflecting a tunable beam fraction from complete transmission (0 OD) to 4 OD. A power diode (S120C, *Thorlabs*) ensures precise control over the excitation power. The beam is then directed toward an interchangeable dichroic mirror, which reflects it onto the objective, focusing the laser onto the sample. The sample is mounted on a three-axis stage and, in the cryogenic micro-PL setup, is housed inside the closed-cycle helium cryostat. Before reaching the dichroic mirror, sufficient space is available for wavelength tailoring via optical filters such shortpass or bandpass filters. It is further possible to alter the excitation beam spot size by inserting a so-called diffusor lens in front of the sample. This results in a non-collimated beam entering the objective, hence increasing the illuminated area on the sample.

3.5.2 Steady-State Photoluminescence

After excitation, the PL signal is collected by the same objective, while residual laser light is filtered using a longpass filter. For steady-state PL measurements, the emitted light is directed toward the spectrometer (HRS-500-MS, *Teledyne Princeton Instruments*), which is identical for both the RT and cryogenic micro-PL setup. The PL is then focused onto the entrance slit of the spectrometer. Both spectrometers are equipped with a grating turret featuring three positions: one with a mirror that directs the signal to a charge-coupled devive (CCD, PIXIS 400BR eXcelon, *Teledyne Princeton Instruments*) to generate a PL image of the sample, and two with diffraction gratings. The gratings differ between both setups, offering different spectral resolutions with 150 mm^{-1} and 300 mm^{-1} for the RT micro-PL setup and 150 mm^{-1} for the cryogenic micro-PL setup, all blazed at 500 nm and an additional holographic grating with 1800 mm^{-1} for the cryogenic micro-PL setup.

3.5.3 Time-Resolved Photoluminescence

While steady-state PL microscopy provides spatial and spectral information about the PL of the sample, it does not capture the time-dependent dynamics of the PL. For that, time-resolved PL (TRPL) measurements are performed. TRPL allows for the determination of charge carrier lifetimes by recording the decay of PL intensity over time following excitation. In both the RT and the cryogenic micro-PL setup, TRPL is measured using the time-correlated single photon counting (TCSPC) method, which is based on the detection of single photons emitted by a sample in response to a pulsed excitation source. Instead of guiding the PL signal into the spectrometer, it is coupled into a fiber-connected SPAD (MPD-SPAD-100, *Micro Photon Devices*) that detects individual emitted photons and records their arrival times. This, paired with the pulsed white light laser, which sends a reference signal with each pulse, can be used as a stopwatch. The laser serves as the start signal, while the detection of a photon by the SPAD acts as the stop signal. The information is processed with a TCSPC card (TimeHarp 260, *PicoQuant*), allowing the measurement of the time difference between the laser pulse and the detected photon (see Figure 3.3). This process is repeated millions of times to build a statistical distribution, ultimately forming the PL decay curve.

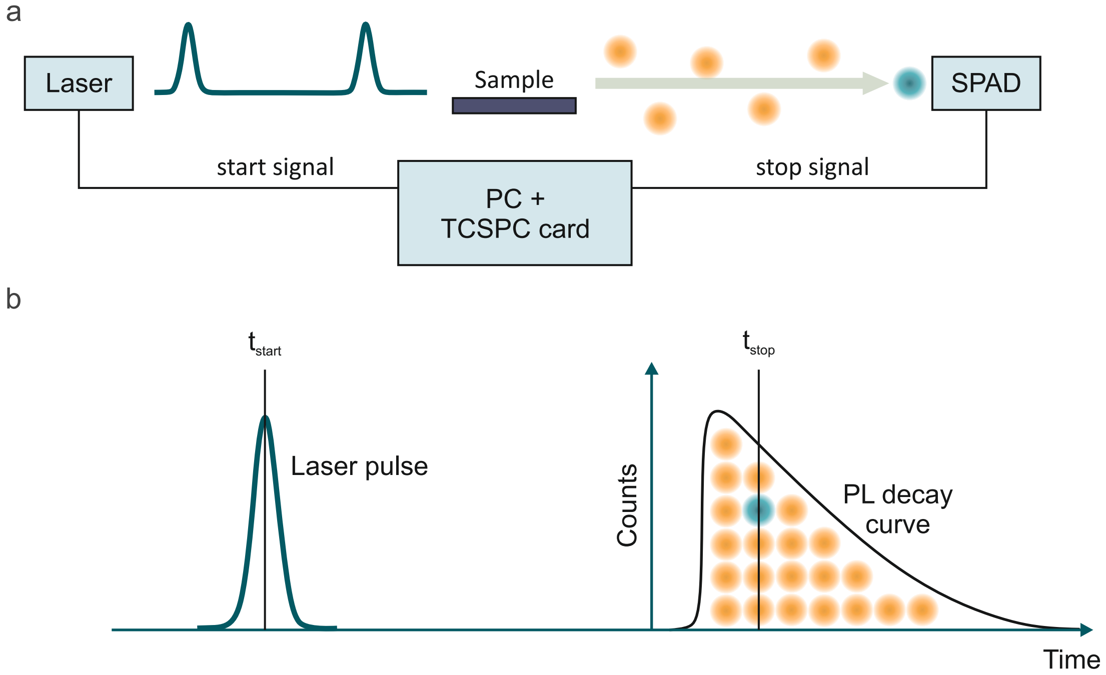

Figure 3.3: Time-Resolved Single Photon Counting. a) Schematic representation of a photon detection event in a TCSPC setup. **b)** Illustration of how each detected photon contributes to building the time-resolved PL decay curve.

A crucial aspect of this method is ensuring that the number of detected photons remains low to avoid the so-called photon pile-up effect. In this process, too many photons arrive at the SPAD in quick succession, which consequently underestimates the number of photons and artificially shortens the PL decay time. A rule of thumb is that the photon count rate on the SPAD should be below 1% of the laser repetition rate, which can be achieved by attenuating the PL signal with a motorized neutral density filter wheel. Since no diffraction grating separates the PL signal spectrally, the recorded data represents the total integrated PL as a function of time. However, if PL peaks are well separated, optical filters can be used to isolate specific spectral regions. The temporal resolution of this technique is primarily determined by the instrument response function (IRF), which is influenced by the finite pulse width of the laser and the time required to convert a detected photon into an electrical signal. The IRF can be experimentally determined by performing TCSPC on the excitation source itself. At the excitation wavelength used in all measurements, the time after the IRF intensity decays to 1/e of its maximum was measured to be below 300 ps. Since the PL decay times measured with these setups are in the nanosecond regime in this study, the IRF does not significantly affect the results.

3.6 Temperature-Dependent Ultrafast Spectroscopy

The previous chapter discussed TRPL spectroscopy measured via TCSPC. While TCSPC provides high temporal resolution down to a few hundred picoseconds, it is inherently limited by the detection electronics, preventing the resolution of ultrafast processes occurring on even faster timescales. To overcome this temporal limitation, an ultrafast spectroscopy system from *Light Conversion* was acquired, which is schematically depicted in Figure 3.4. The heart of it is a 40 W femtosecond laser

(Carbide CB3), which generates ultrashort pulses that are immediately split into two beams after exiting the laser. One beam is directed into an optical parametric amplifier (OPA, Orpheus-HP) to produce a laser beam with tunable excitation wavelength (pump beam), while the other is used for white light generation (WLG, white light or probe beam). A motorized delay stage allows precise control over the temporal delay between the pump beam from the OPA and the probe beam at the sample position. The sample is positioned on a three-axis piezo-controlled stage inside a closed-cycle cryostat (attoDRY800, *attocube*), enabling measurements from 4 K to 300 K. Detailed documentation for the setup, including comprehensive manuals that explain both the theoretical foundations and the practical operation of the setup, is available from *Light Conversion*.[84,85] The manuals can be downloaded via the *Light Conversion* website with a registered user account.

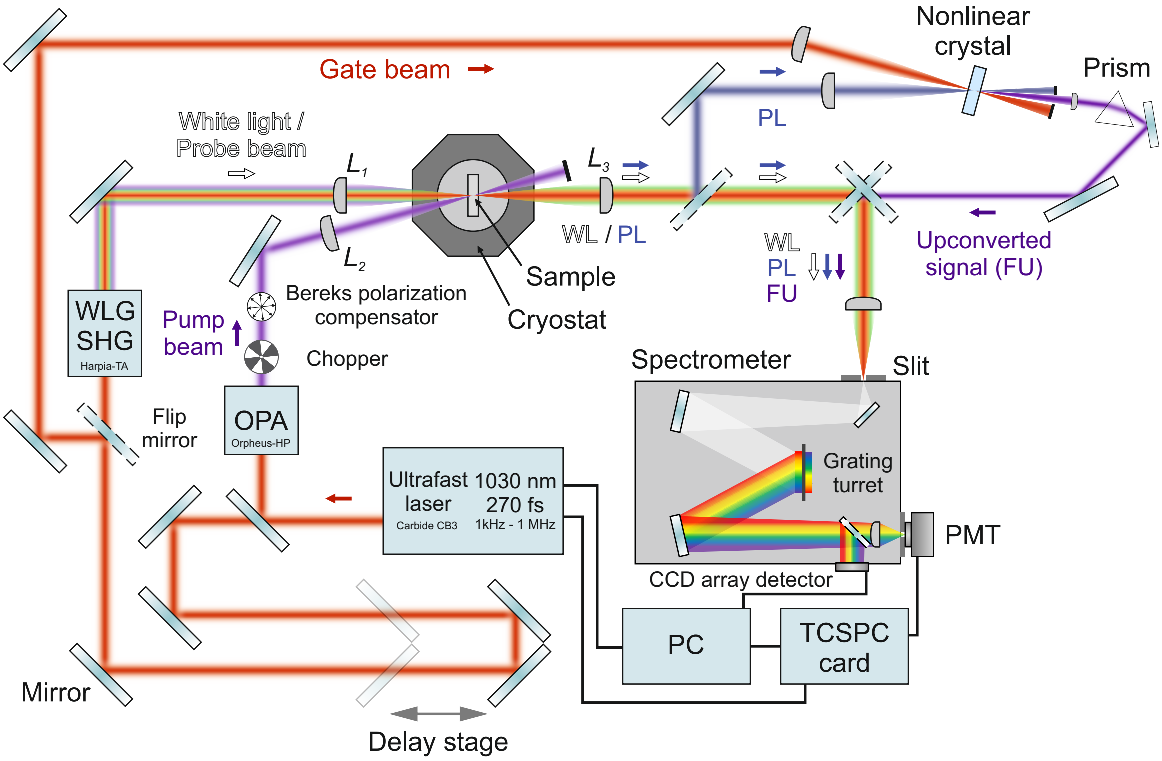

Figure 3.4: Ultrafast Spectroscopy Setup. Schematic of the ultrafast spectroscopy setup. The main setup components are depicted and labeled. The inital laser beam is shown in red, the generated pump beam and the upconverted signal in purple, the PL in blue and the white light has rainbow colors.

This setup offers multiple measurement options: the white light beam alone can be used for linear absorption measurements, similar to those performed with the commercial spectrofluorometer. Alternatively, the pump beam can be used for sample excitation, with the resulting PL directed into the spectrometer for steady-state PL measurements. The white light beam can also be temporally and spatially overlapped with the pump beam at the sample position to perform pump-probe or transient absorption spectroscopy (TAS). Additionally, fluorescence upconversion spectroscopy (FLUPS) can be measured by overlapping the PL signal with the original femtosecond beam (gate beam) in a nonlinear crystal. A spectrometer (Kymera 193i from *Andor*) equipped with two different gratings (300 mm^{-1} grating blazed at 300 nm and 150 mm^{-1} grating blazed at 500 nm), a photomultiplier tube (PMT, PMC-150-4 from *Becker & Hickl GmbH*), and a CCD array detector are used for signal detection. Optical components such as lenses, optomechanics were purchased from *Thorlabs* and adapters were custom-designed and fabricated using 3D printing.

3.6.1 Femtosecond Laser System

The laser system used for all operations in the ultrafast spectroscopy setup is a water-cooled Carbide CB3 femtosecond laser system from *Light Conversion*. The complete system is enclosed in a temperature-controlled housing, which guarantees stable and reliable functionality. The system is based on a technique called chirped pulse amplification. This technique involves temporal stretching of a femtosecond pulse outside the cavity with the active medium to reduce the energy density. The stretched pulse is then strongly pumped inside the cavity. After exiting the cavity, the laser pulse is temporally compressed again, which results in ultra-high laser intensities with femtosecond pulse length. The components used for chirped pulse amplification are a Kerr lens mode-locked oscillator, a regenerative amplifier, and a stretcher-compressor (S-C) unit, which all together enables the amplification of femtosecond laser pulses. The first part is the generation of femtosecond pulses in the oscillator. A Yb:KGW (ytterbium-doped potassium gadolinium tungstate) active medium is directly pumped with a diode. The semitransparent mirror of the cavity allows the generated femtosecond pulses to leave the cavity. The maximum gain bandwidth is around 1030 nm. Afterward, the pulses are guided into the stretcher of the S-C unit. Temporal broadening takes place to reduce the pulse energy density for the amplification step. The regenerative amplifier increases the pulse energy up to 40 µJ with the help of Pockels cells, which act as a high-speed switch. One Pockels cell injects the stretched seed laser into the cavity while another ejects the amplified pulse. This enables a tunable repitition rate ranging from 1 kHz to 1 MHz. As a last step, the outcoming pulses are guided into the compressor of the S-C unit. Here the pulse length can be modified between 270 fs and 10 ps. The result is a software-controllable super stable laser system with 40 µJ pulse energy, up to 40 W output power and, wide-range pulse length and repetition rate tunability. A detaild description of the laser system can be found in the Carbide CB3 manual.[86]

3.6.2 Optical Parametric Amplifier

Another essential part of the measurement setup is the OPA Orpheus-HP. Although an OPA itself is not capable of generating light, once a seed laser is used, it is possible to get pulsed emission over a large range of wavelengths from 320 nm up to $\approx$ 3 µm. For that, many different processes have to take place inside the OPA, such as WLG, second-harmonic generation (SHG), and parametric amplification (PA). The Orpheus-HP is a two-stage OPA, which means that the white light continuum amplification takes place in two stages, the pre-amplification, where stable and sufficiently bright seed pulses for the second stage are generated, and the power amplification, where the pulse is even further amplified and the useful idler beam is generated. Figure 3.5 shows a schematic of the inside of the OPA divided into differently colored areas. After the beam has exited the Carbide CB3 it is guided into the OPA (red area). The events that follow are listed chronologically and explained below:

1. White-light continuum generation (white)
2. SHG (green)
3. First amplification stage (pre-amplifier) (blue)
4. Second amplification stage (power amplifier) (purple)
5. Wavelength separation (pink)

6. SHG of the signal or idler (SHS/SHI) (orange)
7. Wavelength separation (pink)

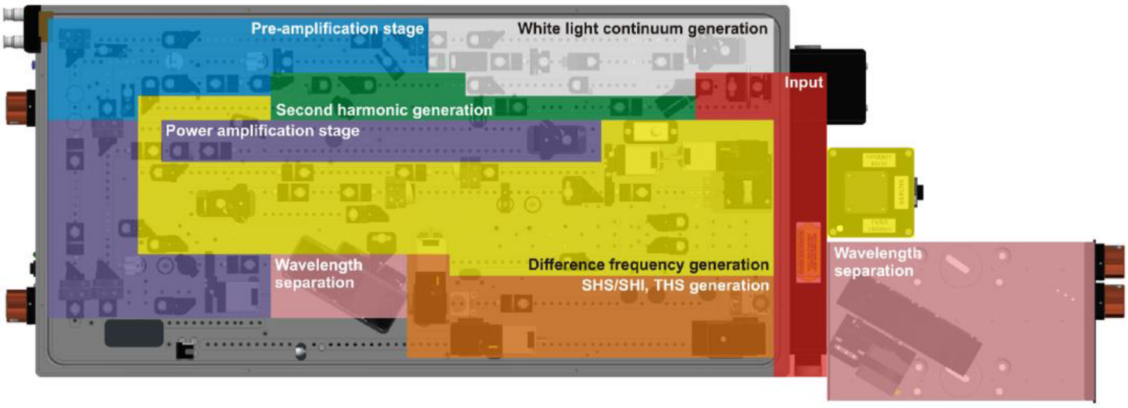

Figure 3.5: Layout of the Subunits in the Orpheus-HP OPA. Schematic of the detailed layout of the OPA. The colored regions highlight the different stages where various nonlinear processes take place, ultimately enabling the broad wavelength coverage of the system. Image taken from Reference [85]

After entering the OPA, the input beam, originating from the Carbide CB3 (1030 nm), is immediately split into two separate beams: a minor part responsible for WLG (white area) and a major part undergoing SHG (green area). In the SHG stage, the fundamental input beam is frequency-doubled in a sapphire crystal, producing a narrowband green beam at 515 nm. This SHG process, illustrated in Figure 3.6 a, involves the conversion of two photons from the initial beam into one photon at the doubled frequency. SHG is a specific case of sum-frequency generation (SFG), where both input photons have the same frequency. General SFG, depicted in Figure 3.6 b, involves two photons with the resulting photon having their summed frequency. The same process is also possible as difference frequency generation, but this process is not further explained here since the version of the OPA used in this setup is not equipped with the needed optics. The resulting pulse from SHG acts as the pump pulse for the subsequent PA. Simultaneously, the remaining part of the input beam is focused into another sapphire crystal, which acts as a nonlinear medium, and white light is created with spectral coverage from 630 nm to 1030 nm. Generally, WLG occurs when high laser intensity is achieved in a nonlinear optical medium, and the spectrum and the stability of the generated white light strongly depend on the intensity and the wavelength of the initial beam. In the PA stage, this white light serves as the signal. Due to dispersion, a temporal delay develops within the white light pulse, where shorter wavelengths are delayed with respect to longer ones. This intrinsic chirp allows selective temporal overlap with the pump pulse. A delay line in the SH beam path enables the selection of the spectral region to be overlapped and, thus, amplified. In the pre-amplification stage (blue area), the white light signal and the 515 nm pump pulse are overlapped non-collinearly in a nonlinear crystal. PA occurs, during which a pump photon splits into an amplified signal photon and a lower-energy idler photon (see Figure 3.6 c). Considering energy and momentum conservation, the following applies to the pump photon energy:

$$\omega_\mathrm{p} = \omega_\mathrm{s} + \omega_\mathrm{i} \tag{3.5}$$

where ω_p is the frequency of the pump photon, ω_s the frequency of the signal photon and ω_i the frequency of the newly generated idler photon. Since the alignment of the beams is non-collinear, residual pump and idler photons can be blocked, and the signal beam can be guided toward the next area. Compared to the pre-amplification stage, which aims to produce stable and sufficiently bright signal pulses, the power amplification stage focuses on further amplification. Basically, PA is also used here, with the difference being the collinear geometry. This allows for both the amplified signal (between 630 nm and 1030 nm) and the generated idler (between 1030 nm and 3137 nm) beams to leave the crystal at the same position and in the same direction. In the next step, the signal and idler beam are separated by a wavelength separator. A wavelength separator consists of two dichroic mirrors for specific wavelength regions, which are also sensitive to beam polarization.

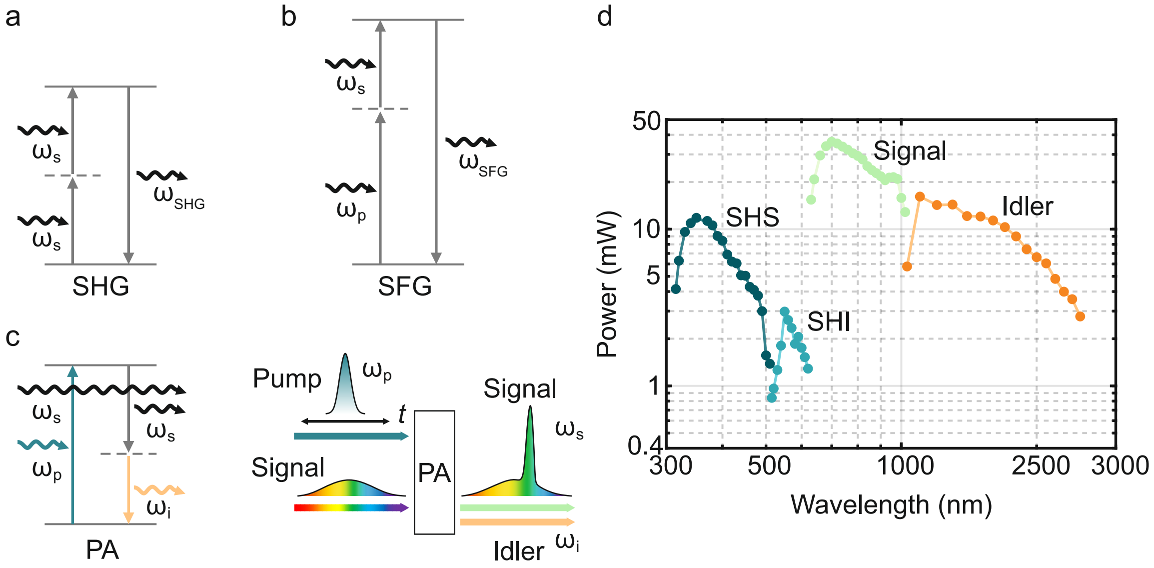

Figure 3.6: Nonlinear Processes and OPA Output Wavelengths. Multiple nonlinear processes are utilized to achieve a broad range of wavelengths from a monochromatic laser. The most important processes are schematically represented in the diagrams: **a)** SHG, **b)** SFG, and **c)** PA (energy diagram (left), schematic (right)). **d)** Tuning curves of the OPA, which can be operated in four different modes to achieve this wavelength coverage.

Once separated, it is possible to use SHG on either the signal or idler beam (SHS/SHI) to tune the available wavelength regions further. A second wavelength separator is used afterward to filter the beams. Figure 3.6 d shows the possible output wavelengths and intensities achievable with the OPA. There, it becomes evident that the output intensity strongly depends on the white light coverage and the efficiency of the amplification process. Since the output beam from the OPA is generally used for exciting or pumping the sample, it is defined as the pump beam from hereon. More detailed information on optical components and beam guiding can be found in the Orpheus-HP manual.[85]

3.6.3 Setup Improvements

Since this setup, unlike our other custom-built setups, was not initially tailored to our measurement and sample preparation methods, it was modified and optimized throughout the course of this work. Most of the setup is enclosed within boxes, each originally designed for a particular measurement method. Due to the tight space inside these boxes, the potential for setup modifications is limited. Therefore, the following section focuses primarily on the area surrounding the external cryostat and is divided into the excitation path, covering the beam path up to the sample position, and the detection path, which includes all optical elements after the sample. Figure 3.7 a shows the setup before any modification. Furthermore, the detection beam path has to be prepared according to the type of optical method selected to be measured. Absorption-based methods, such as linear absorption spectroscopy and TAS, which rely on probing the sample with broadband white light, require the white light collimating lens. PL-based methods, including steady-state PL, TCSPC, and FLUPS, require the PL collecting lens to collimate the PL emitted by the sample.

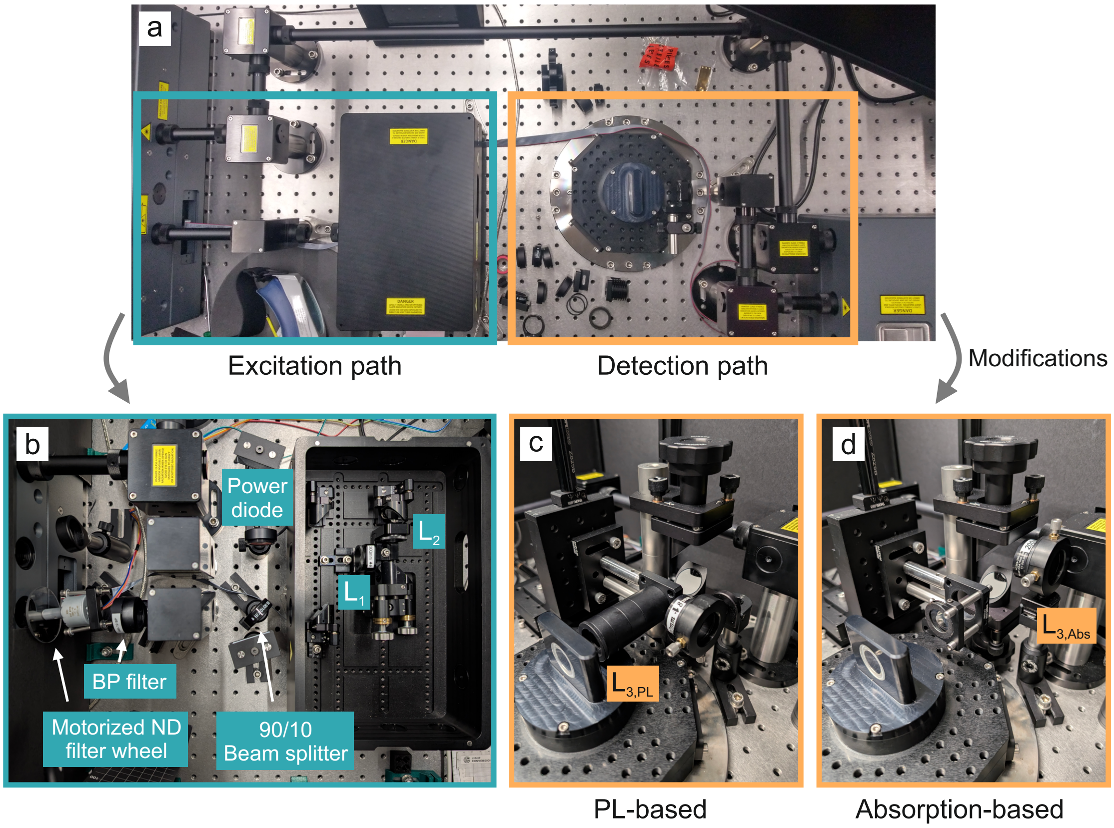

Figure 3.7: Ultrafast Spectroscopy Setup Improvements. Photographs of the ultrafast spectroscopy setup sample area before **(a)** and after improvements **(b-d)**. In the excitation path, a motorized neutral density filter wheel and a power photodiode were added. In the detection path, a motorized three-axis stage and an open periscope were installed. The PL-based detection path is used for techniques such as steady-state PL, TCSPC, and FLUPS, while the absorption-based detection path is used for linear absorption and TAS.

Excitation Path

Figure 3.7 b shows the modified excitation path. A custom-built, motorized neutral density filter wheel and a mount for integrating additional optical filters were implemented in the excitation path. Combined with a beam splitter and a photodiode to measure the laser power, this configuration enables precise control over the excitation beam. For PL-based methods like steady-state PL, TCSPC, or FLUPS, the position of the lens that focuses the pump beam onto the sample can be adjusted. This enables tuning of the beam spot size and thereby control over the laser fluence at the sample position. Similarly, the focusing lens is interchangeable in absorption-based measurements. This allows the position of the white light focus to be adjusted depending on the measurement type: for TAS, the white light is focused at the sample position, whereas for linear absorption, it can be focused in front of the sample to illuminate a larger area and improve signal averaging.

Sample Holder and Detection Path

On the detection side, several components were redesigned to improve PL collection. A three-axis motorized translation stage was installed to align the PL collection lens (L3), allowing for fast and accurate spatial optimization of the lens position of the captured PL signal. The periscope guiding the light toward the spectrometer was rebuilt using larger mirrors to ensure that the entire signal is transmitted to the spectrometer. The PL collection lens can be easily removed when switching between PL and absorption-based methods. A flip-mounted lens is inserted instead to collimate the white light after traversing the sample (see Figure 3.7 c,d). Several 3D-printed sample holders were designed, and existing holders were modified to accommodate different sample types and experimental conditions. For RT measurements, two custom holders, one for cuvettes and one for substrates, allow for quick sample insertion and removal. This eliminates the need for conductive silver paste for the original sample holder, which was specifically designed for cryogenic measurements. The conductive silver paste ensures optimal thermal coupling to the holder. Furthermore, a cage system was installed in front of the spectrometer, providing an easy way to focus the PL signal onto the entrance slit of the spectrometer.

Automation
Another improvement was the partial automation of the setup. Custom-written software integrates control over the laser, detectors, filter wheels, and cryostat via their respective application programming interfaces (APIs). This enables fully automated temperature ramps and power-dependent measurement series. For more technical details, refer to the master thesis by Patrick Haußmann.[87]

3.6.4 Linear Absorption and Steady-State Photoluminescence

While the ultrafast spectroscopy system from *Light Conversion* was not initially designed for linear absorption and steady-state PL measurements, these methods were enabled by modifying the setup and circumventing software restrictions. As a result, the data obtained can be compared to that collected using the commercial spectrofluorometer or the micro-PL setup, mentioned in Subsection 3.4.1 and Section 3.5, respectively. For steady-state PL, the pump beam is used as an excitation source, and the emitted PL is subsequently directed toward the spectrometer and detected by the CCD array. The pulsed white light is used for linear absorption measurements. However, slight differences exist between absorption measurements performed with this system and those using, for example, the commercial spectrofluorometer. The most important one arises from the pulsed nature of the white light, introducing intensity fluctuations and, therefore, possible variations in the absorption spectrum over time. The sample holder was modified to have space for two 5×10 mm substrates to mitigate this issue. This made it possible to mount a reference substrate alongside the sample, allowing both to be measured in close succession under nearly identical white light conditions. Another challenge is the small focus area of the white light beam at the sample position, which enhances local inhomogeneities in thin-film measurements. This issue can be addressed by adjusting the positions of lenses L2 and L3 (see Figure 3.4), thereby increasing the spot size and obtaining a more spatially averaged absorption spectrum. Similarly, for PL measurements, the excitation spot size can be tuned by modifying the position of lens L1. These additional adjustments make linear absorption and PL measurements in this setup more complex than in the other setups. Nonetheless, its unique advantage is the possibility of measuring temperature-dependent absorption. To achieve this, both a sample and a reference substrate must be placed inside the cryostat. A spectrum for the sample and the reference must then be recorded to calculate the absorption spectrum.

3.6.5 Transient Absorption Spectroscopy

In addition to steady-state measurements, the setup also enables time-resolved techniques such as TAS. Since TAS is an indirect optical measurement method, it is possible to achieve femtosecond resolution as it is solely determined by the duration of the ultrafast laser pulses rather than by electronic signal processing. Generally, two laser pulses spatially overlap at the sample position: a pump pulse and a probe pulse. The pump pulse is a narrow-band, high-intensity beam with photon energy above the sample's bandgap and is responsible for exciting charge carriers into the CB. The probe pulse is a broad white light continuum that measures the sample's absorption with and without the presence of excited charge carriers. By varying the time delay between the pump and probe pulse, absorption changes of the sample at specific times after excitation can be recorded. Similar to the WLG in the OPA explained earlier (see Subsection 3.6.2), the femtosecond pulses with a wavelength of 1030 nm from the Carbide CB3 laser are focused onto a sapphire crystal. WLG is a very sensitive process, meaning that to create a stable white light, the focus, intensity, and diameter of the laser beam hitting the crystal must be tweaked iteratively. This can be done with an aperture and a neutral-density filter wheel positioned before the crystal. The setup allows for the generation of two distinct white light spectra: one covering the visible (VIS) to near-infrared region, produced using the fundamental 1030 nm laser pulse, and another extending into the UV range, which is generated by first frequency-doubling the 1030 nm laser via SHG in a beta barium borate (BBO) crystal to produce 515 nm light before WLG in the sapphire crystal. Both white light spectra are shown in Figure 3.8. Although an optical filter is installed behind the sapphire crystal to filter out residual SHG radiation, it is clearly visible in the corresponding white light spectrum.

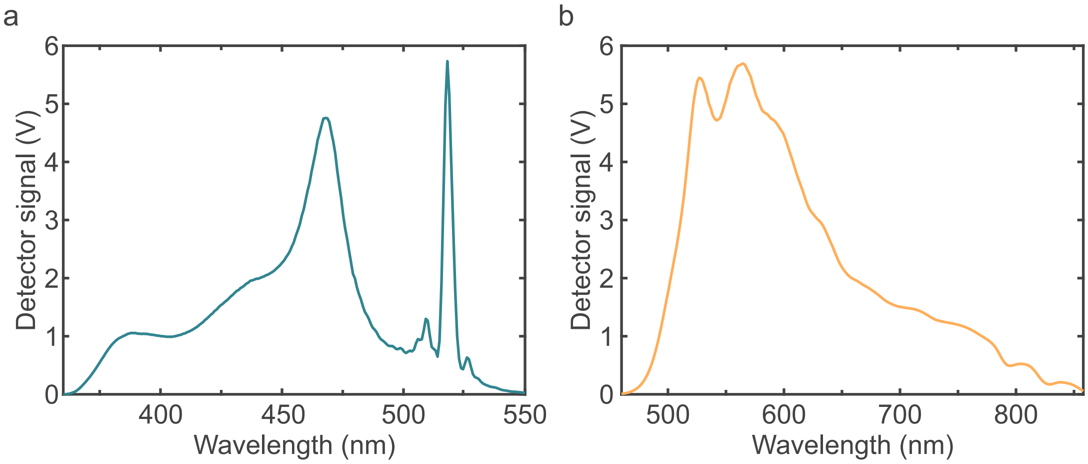

Figure 3.8: White Light Spectra for TAS. White light spectra generated in a sapphire crystal and detected with the spectrometer in the ultrafast spectroscopy setup. The spectrum generated with the frequency-doubled 515 nm beam is shown in **(a)** and the white light generated with the fundamental 1030 nm beam is depicted in **b)**.

After generation, the white light is collimated by a mirror and directed toward the sample position. Before the wavelength-tunable pump pulse reaches the sample, it passes through a Berek polarization compensator, which enables full adjustment of its polarization. This device allows precise tuning of any polarization (linear, elliptical, or circular) into any other, effectively acting as a universal wave plate. The Berek compensator features two degrees of freedom: rotating both axes simultaneously rotates the internal birefringent crystal, while rotating only one axis effectively tilts it, enabling fine control of the output polarization. After the compensator, the beam passes through a 10-slot optical chopper, which operates at frequencies between 25 Hz and 750 Hz, typically set to 100 Hz. This modulates the pump pulse by partially or fully blocking it in a controlled sequence. A photodiode detects this modulation, allowing the system to determine whether a given probe pulse has interacted with an excited or unexcited sample. This information is crucial for distinguishing between the transmitted probe pulse intensity in the absence of excitation, $I_{\text{not pumped}}(\lambda)$, and the transmitted intensity when the sample has been excited, $I_{\text{pumped}}(\lambda)$. According to Equation 3.1 the change in absorbance of the sample $\Delta A(\lambda)$ can be calculated for each time delay t_i:

$$\begin{aligned}
\Delta A(\lambda, t_i) &= A_{\text{pumped}}(\lambda, t_i) - A_{\text{not pumped}}(\lambda, t_i) && (3.6)\\
&= log_{10}\left(\frac{I_0(\lambda, t_i)}{I_{\text{pumped}}(\lambda, t_i)}\right) - log_{10}\left(\frac{I_0(\lambda, t_i)}{I_{\text{not pumped}}(\lambda, t_i)}\right) && (3.7)\\
&= -log_{10}\left(\frac{I_{\text{pumped}}(\lambda, t_i)}{I_{\text{not pumped}}(\lambda, t_i)}\right) && (3.8)
\end{aligned}$$

Such a 2D data set is also called a transient absorption spectrum. Due to the pulsed nature of the laser in combination with the chopper, several thousand spectra can be acquired every second for each fixed delay stage position. Based on the photodiode signal, the recorded spectra are sorted into pumped and not pumped categories. By averaging multiple spectra within each category, mean pumped and not pumped spectra are obtained, and $\Delta A(\lambda, t_i)$ can be calculated following Equation 3.6. An interesting aspect of this approach is that the initial probe intensity I_0, which represents the intensity measured through a reference sample, cancels out in the calculation. As a result, no separate reference measurement is required since the transient absorption signal is solely based on the relative difference between the pumped and not pumped spectra. Alternatively, the transient absorption signal $\Delta A(\lambda, t_i)$ can be expressed in terms of the relative change in transmittance $\Delta T(\lambda, t_i)/T_0(\lambda, t_i)$. Since A is related to transmittance via Equation 3.6, the change in relative transmittance can be rewritten as:

$$\frac{\Delta T}{T_0}(\lambda, t_i) = \frac{T(\lambda, t_i) - T_0(\lambda, t_i)}{T_0(\lambda, t_i)} = \frac{\frac{I_{\text{pumped}}(\lambda, t_i)}{I_0(\lambda, t_i)} - \frac{I_{\text{not pumped}}(\lambda, t_i)}{I_0(\lambda, t_i)}}{\frac{I_{\text{not pumped}}(\lambda, t_i)}{I_0(\lambda, t_i)}} = \frac{I_{\text{pumped}}(\lambda, t_i)}{I_{\text{not pumped}}(\lambda, t_i)} - 1 = 10^{-\Delta A(\lambda, t_i)} - 1 \tag{3.9}$$

For successful TAS measurements, it is essential to ensure spatial overlap between the pump and probe beams at the sample position. Additionally, the pump beam must have a diameter at least two to five times larger than the probe beam to ensure uniform excitation across the entire probed region, preventing intensity variations due to inhomogeneous pumping. The pump pulse is blocked after interaction with the sample to minimize unwanted background signal. The white light is collimated and guided toward the spectrometer, where it is focused on the 200 µm slit. After being separated spectrally via a grating, it is detected by a CCD array and converted to a spectrum. In addition to the spatial overlap, temporal overlap is necessary. The temporal overlap is varied via a motorized delay stage with a retroreflector. This changes the path length of the probe pulse, thereby allowing for probing at different times after excitation. The step size of the delay stage is below 1 fs, which means the temporal resolution is limited not by the delay stage but by the laser pulse width. With the current setup configuration, the maximum possible delay between the pump and probe pulse is 3 ns. For the investigation of charge carrier dynamics slower than that, a different method has to be used. Exact information on how the setup acquires and evaluates data in detail can be found in the manual.[84]

Fluence Calculation for Transient Absorption Spectroscopy

For fluence-dependent measurements, calculating the exact fluence, defined as the energy per unit area delivered to a target, is essential. In TAS measurements, this is more complex than simply measuring the beam diameter and the laser power with a photodiode. It requires knowledge of the laser repetition rate, the diameters of both laser beams (the pump and the probe), and the power of the pump beam. Since only the pump beam contributes to the excitation of charge carriers, the relevant parameter is the portion of the pump beam that spatially overlaps with the probe beam. To calculate this, the power of the pump beam is initially measured directly at the sample position using a photodiode power sensor (S120VC C-Series, *Thorlabs*). A second photodiode is placed before the sample, where a small fraction of the beam is split off via a beamsplitter. After calibrating the two sensors against each other, the beamsplitter photodiode can be used as a reference to monitor the fluence in real-time during measurements, eliminating the need to place the power sensor directly at the sample position. The beam diameter was determined by directly imaging the beams on a CCD camera (MU130, *AmScope*) at the sample position (see Figure 3.9 a). Here, both beams were approximated as Gaussian beams, and the intensity profile can be described as:

$$I(r) = I_0 \exp\left(\frac{-2r^2}{w_0^2}\right) \tag{3.10}$$

with I_0 being the peak intensity of the beam, r the radius where the intensity is measured, and w_0 the Gaussian beam waist (defined such that $I(w_0) = I_0 \times 1/\exp(2)$). The beam waist can then be extracted from the beam image on the CCD. With the pixel size of the CCD, direct conversion of the measured diameter from pixels to a physical length is possible (see Figure 3.9 b).

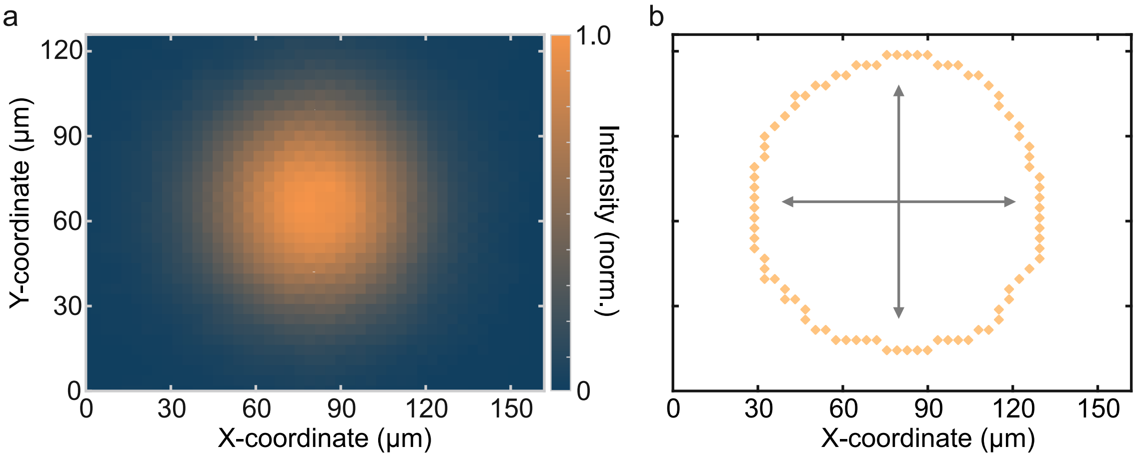

Figure 3.9: Beam Spot Size Determination. **a)** Image of the focused white light spot captured at the focal plane using a CCD camera. **b)** Position of pixels where the intensity values correspond to the beam waist definition. These positions specify the beam waist and are used to determine the beam spot diameter.

To differentiate between the pump and probe beam, let w_{pump} be the Gaussian beam waist of the pump beam, and w_{probe} the Gaussian beam waist of the probe beam. The fluence F under the probe beam spot is computed as follows:

$$F = \frac{\int_0^{2\pi} d\theta \int_0^{w_{\text{probe}}} I_0 \exp\left(\frac{-2r^2}{w_{\text{pump}}^2}\right) r\, dr}{\pi w_{\text{probe}}^2 \times f} \tag{3.11}$$

with I_0 the peak intensity of the pump beam, and f the repetition rate of the pump beam. While the probe beam also has a Gaussian profile, its effect is approximated by averaging the pump intensity over the probe area πw_{probe}^2. This is valid when the probe beam is much smaller than the pump beam, making intensity variations within the probe region negligible. I_0 cannot be measured directly, but the total pump beam intensity $I_{\text{tot}} = 2\pi \int_0^{\infty} I_0 \exp\left(-2r^2/w_{\text{pump}}^2\right) r\, dr = I_0 \times \frac{\pi w_{\text{pump}}^2}{2}$ is known, thus Equation 3.11 can then be written as:

$$F = \frac{2\pi \times \left(I_{\text{tot}} \times \frac{2}{\pi w_{\text{pump}}^2}\right) \times \frac{w_{\text{pump}}^2}{4}\left(1 - \exp\left(\frac{-2w_{\text{probe}}^2}{w_{\text{pump}}^2}\right)\right)}{\pi w_{\text{probe}}^2 \times f}$$

$$F = \frac{I_{\text{tot}}\left(1 - \exp\left(\frac{-2w_{\text{probe}}^2}{w_{\text{pump}}^2}\right)\right)}{\pi w_{\text{probe}}^2 \times f} \tag{3.12}$$

It is important to note that in this context, the spot size is defined using the beam waist. However, spot size is sometimes defined based on the full width at half maximum (FWHM) of the beam. Despite this difference in definitions, the resulting fluence calculations show negligible variation.

3.6.6 Wavelength-Dependent Time-Resolved Photoluminescence

This setup also enables TCSPC measurements combined with the advantage of spectral resolution. Instead of simultaneously detecting the wavelength-integrated PL signal as in the micro-PL setup, it is spectrally dispersed using a diffraction grating before reaching the single-photon detector. The grating and the entrance slit width of the spectrometer thereby determine the spectral resolution. A PMT, positioned behind an adjustable entrance slit, records the intensity at specified wavelengths. The TCSPC module (consisting of a detector control module DCC-100 and the TCSPC module SPC-130-EM, both from *Becker & Hickl GmbH*) then processes the signals from the PMT and the pulsed laser to construct wavelength-resolved PL decay curves, resulting in a 2D map of the time-dependent PL spectrum. Here, the temporal resolution is limited by the timing electronics of the TCSPC system. The advantage of wavelength-resolved detection comes at the cost of reduced signal intensity. Since only a narrow spectral range is measured at a given time, the overall detected intensity is significantly lower, leading to extended acquisition times. Besides analyzing PL decays at specific wavelengths or integrating the signal over the wavelength to get an averaged PL decay, this method also allows tracking the time evolution of the PL spectrum with the resolution of the TCSPC system or integrating over the total time of the TCSPC measurement to get an averaged PL spectrum. Furthermore, the cryostat enables these measurements to be performed as a function of temperature.

3.6.7 Fluorescence Upconversion Spectroscopy

While TCSPC is well-suited for tracking PL dynamics on the nanosecond and sub-nanosecond scale, processes occurring on picosecond and sub-picosecond timescales require a different approach. FLUPS meets this need by using an optical gating mechanism, allowing the time-resolved detection of PL with a resolution defined by the laser pulse width rather than timing electronics. FLUPS is based on the nonlinear optical process of SFG (schematically described in Figure 3.6 b). In this process, the PL emitted by the sample is spatially and temporally overlapped with an ultrashort gate pulse in a nonlinear birefringent crystal. When properly phase-matched, the electric fields of the PL and gate pulse interact constructively, generating an upconverted signal at the sum frequency (ω_{SF}) of the two input waves (ω_{Gate} and ω_{PL}).

$$\omega_{\mathrm{SF}} = \omega_{\mathrm{Gate}} + \omega_{\mathrm{PL}} \quad \text{or} \quad \frac{1}{\lambda_{\mathrm{SF}}} = \left(\frac{1}{\lambda_{\mathrm{Gate}}} + \frac{1}{\lambda_{\mathrm{PL}}} \right)^{-1} \tag{3.13}$$

The resulting signal, therefore, has a higher frequency than the original PL and typically falls within the near-UV or short-wavelength VIS spectral region (ca. 250 nm to 450 nm). For instance, if a sample emits at 460 nm and the gate pulse has a wavelength of 1030 nm, the upconverted signal will appear at approximately 318 nm. Figure 3.10 a shows a schematic of the upconversion process.

Since fluorescence upconversion must be achieved across the entire PL spectrum, phase-matching conditions must be adjusted for each wavelength. Given that the gate beam has a fixed wavelength (1030 nm), this adjustment can be achieved either by varying the angle of the incoming PL emission or by rotating the nonlinear crystal. Because the latter approach is significantly more practical, the setup has the nonlinear crystal mounted on a rotatable stage. It should be noted that upconversion is polarization-dependent. This means the nonlinear BBO crystal selectively phase-matches only specific polarization components (in this case, the ordinary component) of the incoming PL. As a result, the efficiency of the SFG strongly depends not only on the correct wavelength phase-matching but also on the alignment of the polarization of both the PL and the gate pulse. Additionally, since the upconverted signal falls within the UV/VIS spectral range, specialized optics are required for its manipulation. To ensure that only the desired wavelengths reach the spectrometer, a rotatable prism is used to selectively direct the upconverted photons toward the spectrometer entrance slit. Both the calibrated nonlinear crystal and the prism must be rotated in sync for each time step or delay stage position. Moreover, the spatial direction of the upconverted beam is governed by momentum conservation ($k_{\mathrm{SF}} = k_{\mathrm{Gate}} + k_{\mathrm{PL}}$), which means that both the angle and propagation direction of the input beams influence the emission direction of the upconverted light. A photograph of the upconversion region is shown in Figure 3.10 b, illustrating the beam paths and how the upconverted signal is guided to the spectrometer. Since SFG is a second-order nonlinear process, the intensity of the upconverted signal is proportional to the product of the PL intensity and the gate pulse intensity. When assuming a constant intensity for the gate beam, the sum-frequency signal is proportional to the PL intensity. The gate pulse acts as a temporal strobe, effectively slicing the PL signal into time-resolved segments. This means one can reconstruct the PL decay with femtosecond resolution by scanning the temporal delay between the PL and the gate pulse (up to the physical limit of the delay stage - 3 ns). Unlike in TCSPC, where individual photons are time-stamped, FLUPS indirectly measures PL dynamics by tracking the variation in upconverted signal intensity as a function of time delay. It is important to note that

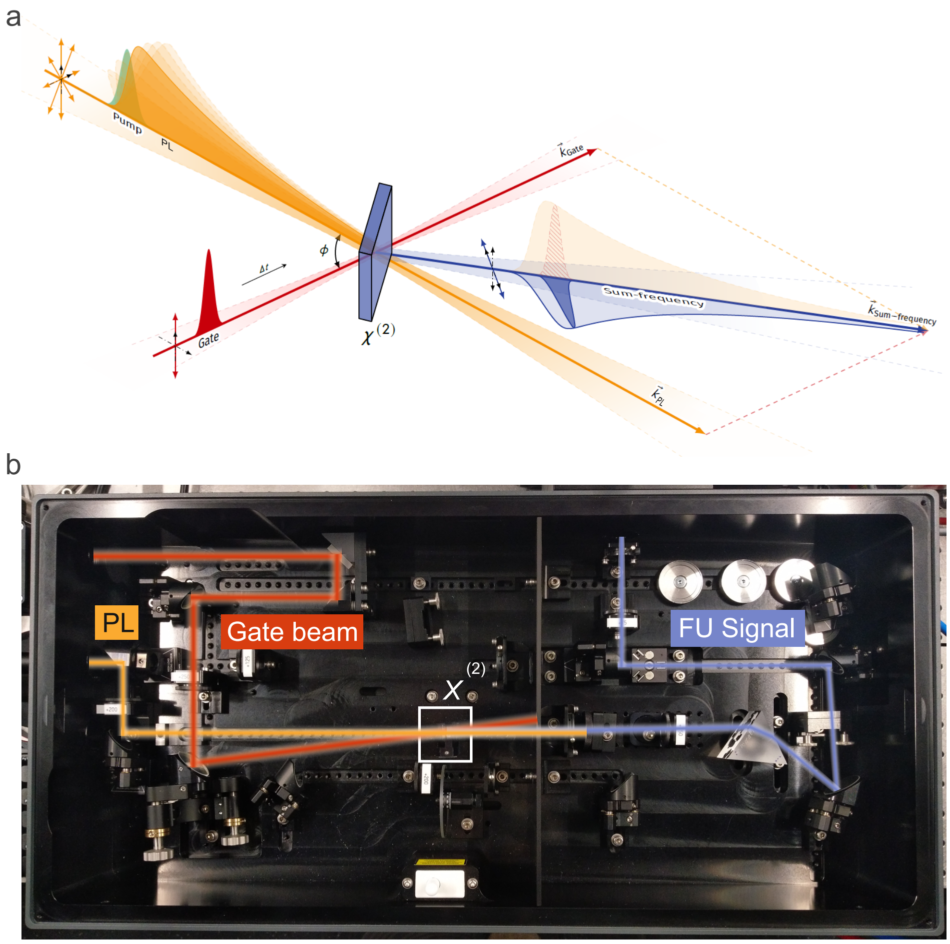

Figure 3.10: FLUPS Principle. a) Schematic illustration of the fluorescence upconversion process. A pump beam excites the sample, generating long-lived fluorescence. A gate beam is spatially and temporally overlapped with the PL in a birefringent BBO crystal, where the two interact via a second-order nonlinear process. The resulting upconverted signal emerges in a phase-matched direction, fulfilling momentum conservation. Adapted from Reference [84]. **b)** Photograph of the upconversion part within the ultrafast spectroscopy setup. The BBO crystal used for the nonlinear interaction is indicated by a white square ($X^{(2)}$). After upconversion, both the gate and the PL beam are blocked. The upconverted signal (FU signal) is then collimated, redirected by a prism and mirrors, and sent to the spectrometer entrance slit.

the intensity of the upconverted signal at different wavelengths cannot be directly compared due to several wavelength-dependent factors, including the nonlinear susceptibility $X^{(2)}$ of the upconversion crystal, phase-matching efficiency, monochromator transmission, and PMT sensitivity. Therefore, spectral calibration techniques such as normalization against steady-state PL must be applied. A detailed description of the measurement method, including the exact procedure for preparation and operation, can be found in Reference [84].

Fluorescence Upconversion Spectroscopy on Perovskite Nanocrystals

One initial goal of this work was to investigate the ultrafast dynamics of perovskite nanocrystals with different thicknesses as a function of temperature, with cryogenic fluorescence upconversion measurements on perovskite nanocrystals of different sizes and shapes. While FLUPS measurements on dispersions have already been demonstrated, thin-film measurements, especially at different temperatures down to 4 K, would have provided valuable insights into exciton dynamics.[88–90] Thin-film measurements, however, pose significant additional challenges. Firstly, the number of nanocrystals excited is much lower due to the limited film thickness, resulting in substantially weaker PL and consequently upconversion intensity. Secondly, thin films are more susceptible to degradation under laser irradiation and environmental exposure than dispersions. Consequently, it was not possible to achieve the initial goal. The following outlines the major challenges and technical difficulties encountered, as well as potential solutions that might enable successful measurements.

Challenges:

1. **Sample Degradation:** Increasing the excitation power can enhance the PL intensity, but perovskite nanocrystals are highly sensitive to photoinduced degradation and heating effects.[91,92] Photodegradation is attributed to the formation of carrier-trapping defects caused by the photoinduced desorption of surface ligands, which is exacerbated by the inherently low binding energy and highly dynamic nature of the ligand attachment to the perovskite nanocrystal surface.[62] In addition, once ligands desorb, enhanced ion mobility, a known characteristic of the soft perovskite lattice, facilitates ion migration, accelerating nanocrystal coalescence.[93] Moreover, thermal effects induced by the laser further contribute to the creation of defect states, compounding the quenching of PL.[94,95]
2. **Measurement Duration:** With this setup configuration, FLUPS requires scanning both spectral (grating) and temporal (delay stage) dimensions. As a result, a single measurement can take between 20 min and 2 h, during which the sample is continuously exposed to high-intensity laser radiation. This prolonged exposure amplifies photodegradation, further reducing measurement success.
3. **Setup Limitations:** Since the intensity of the upconverted signal is directly proportional to the PL intensity, maximizing the PL intensity at the position of the nonlinear crystal is essential. This requires efficient collection of PL from the sample, lossless pathing to the nonlinear crystal, and minimizing the PL's focal spot size while ensuring it remains larger than that of the gate beam. While setup improvements were made to optimize the first two aspects (see Subsection 3.6.3), achieving a sufficiently small focal spot proved challenging. Spatial constraints and the requirement to focus both the PL and gate beam into the crystal at a specific angle limited the extent to which the PL spot size could be reduced (see Figure 3.10 b). The main issue is that reducing the focal length of the PL focusing lens leads to the lens being closer to the crystal, which in turn blocks the gate beam. As a result, the upconversion signal intensity always remained extremely low, often barely detectable. Compounding this challenge is the deep UV wavelength of the upconverted signal for blue-emitting nanocrystals. This makes it extremely difficult to find or align the beam, adding another layer of complexity to this method.
4. **Signal Noise and Pump Beam Upconversion:** Although the pump beam was filtered out after passing through the sample using an longpass filter, its upconverted signal was occasionally detected upon interacting with the nonlinear crystal at the same angle as the PL. While the phase-matching condition was not perfectly met, the excitation wavelength was close to the PL emission of the perovskite nanocrystals, leading to residual upconverted laser radiation that partially overlapped with the upconversion signal of the perovskite nanocrystals. Although the rotating prism was intended to filter unwanted residues, it was insufficient, especially given the perovskite nanocrystals' weak upconversion signal.

Despite these challenges and limitations, the following section will present potential solutions that could improve the feasibility of FLUPS measurements in future studies.

Potential Improvements:

1. **Optimizing PL Focusing:** By reducing the beam spot size of the PL in the nonlinear crystal, the local PL intensity is increased, which directly increases the upconverted signal intensity. To achieve this, a solution is needed to position the PL focusing lens closer to the crystal, for example, by redesigning the PL or gate beam path to prevent the lens from obstructing the gate beam.

2. **Enhancing Perovskite Nanocrystal Stability:** The degradation of perovskites under high-intensity laser irradiation could be mitigated by improving their stability. Given the matter of this topic, many articles have been published to understand and improve the stability of perovskite nanocrystals.[13,96] The main strategies for improvement involve encapsulation of nanocrystals in polymer or inorganic matrices and ligand engineering. Ligand exchange has shown promising results in enhancing stability by strengthening the surface passivation of nanocrystals.[81,97] However, while ligand-based strategies could effectively reduce photodegradation, making FLUPS potentially more viable, polymer encapsulation does not provide sufficient protection against laser-induced degradation, as confirmed in Section 6.2 of this work.

3. **Upgrading the Setup:** A promising alternative to conventional FLUPS is optical Kerr-gating (OKG), recently introduced as a possible setup upgrade by *Light Conversion*. Unlike FLUPS, which requires scanning each wavelength individually, OKG enables simultaneous upconversion of the entire PL spectrum, significantly reducing acquisition time and thereby minimizing sample degradation. In this technique, PL from the sample first passes through a linear polarizer, defining its polarization. The PL then enters a Kerr medium placed between two crossed polarizers. Under normal conditions, the crossed polarizers block the emission completely. However, when a short gate pulse, polarized at 45° relative to the first polarizer, passes through the Kerr medium at the same time, it induces optical anisotropy, rotating the polarization of the PL. This rotation allows part of the PL to pass through the second polarizer and reach the spectrometer. The Kerr medium thus acts as an ultrafast optical shutter, enabling time-resolved detection of the full PL spectrum without wavelength scanning.[84]

3.7 Cavity-Enhanced Extinction Spectroscopy

The cavity-enhanced extinction spectroscopy (CEES) setup on which the equally named method is based is located in the laboratory of Qlibri GmbH at the LMU in Munich. All measurements using this technique were performed by Ines Amersdorffer, a PhD student in the research group of Prof. Dr. David Hunger at the KIT in Karlsruhe. Accordingly, the following section does not provide a detailed explanation of the method but rather provides a brief overview. A comprehensive description of the fundamental physics, the experimental setup, and the possibilities of this method can be found in References [98], [99], and [100].

Linear absorption spectroscopy is a powerful tool for probing the optical properties of nanocrystals, but its applicability quickly diminishes when the number of nanocrystals per unit area becomes too low to produce a measurable absorption signal. While many groups have already studied the PL of single nanocrystals, there is not much literature on absorption measurements of single nanocrystals.[101,102] The advantage of absorption spectroscopy is that even if the sample is not emissive in general or due to PL quenching from defect states, one can still extract information about the electronic band structure. It is important to note that CEES does not directly measure absorption but extinction, which includes both absorption and scattering. Depending on the scattering characteristics of the sample, the extinction signal can, in some cases, be interpreted as absorption.[103] CEES is based on a high-finesse optical microresonator, where two highly reflective mirrors are aligned opposite each other, creating a cavity where a standing light wave can be formed. The light bounces back and forth between the mirrors up to 200,000 times depending on the mirror coating, drastically increasing the effective interaction length with the sample. The probability that a photon gets absorbed or scattered increases with the average number of round-trips, which is quantified by a number termed the finesse of the cavity. A schematic overview of the setup is provided in Figure 3.11 a. The system consists of a broadband pulsed white light fiber laser (White Lase SC450 by *Fianium*), and a tunable filter (SuperK Varia, *NKT Photonics*) with a wavelength range from 460 nm to 2000 nm, coupled into the cavity. An APD (APD440A2 from *Thorlabs*) is used as a detector. A short open area behind the planar mirror leaves space for further optical components.

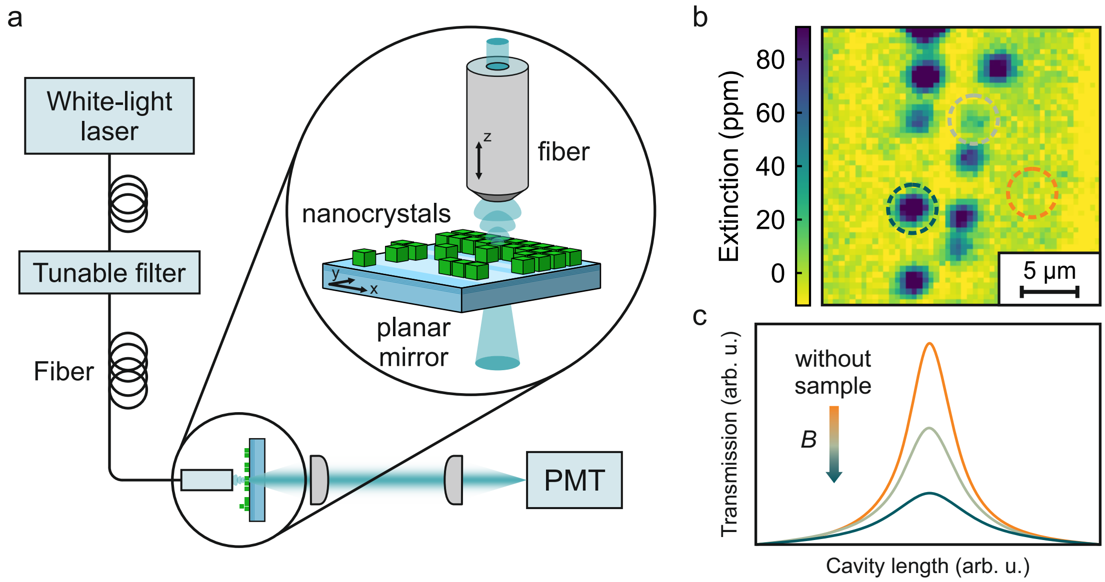

Figure 3.11: Spatially Resolved Extinction Measurement via CEES. a) Schematic of the CEES setup. The inset highlights the microcavity formed between the fiber and a movable planar mirror. After selecting a specific wavelength, the mirror is scanned laterally to generate a two-dimensional extinction map of the sample. **b)** Example of such an extinction map recorded at a fixed wavelength. The color scale indicates local extinction variations caused by absorbing particles (for example, nanocrystals) on the mirror surface. **c)** Cavity transmission spectra schematically shown for three different positions from the map in (b). Transmission is highest in regions without absorbing particles and decreases with increasing particle density.

In this setup, one of the mirrors is a concave micromirror fabricated at the end facet of a single-mode optical fiber, while the second mirror is planar and serves as the substrate on which the nanocrystals are deposited. This planar mirror does not perfectly reflect the light, and a minimal amount can leave the cavity through it. A detector placed behind the substrate then measures the transmitted light. The cavity length can be adjusted by moving the fiber in z-direction. The planar mirror can be moved in-plane, enabling the acquisition of spatially resolved extinction maps, where each scanning step corresponds to one pixel. The resolution of these maps is defined by the mode waist of the cavity mode on the surface of the planar mirror, which is around $1 - 2\,\mu\mathrm{m}$ for the cavity's geometry. By tuning the excitation wavelength across the available range and recording a full extinction map at each wavelength, a hyperspectral extinction map can be created. This approach yields a full extinction spectrum at every spatial coordinate, effectively combining spectroscopy and microscopy in a single dataset. In practice, to improve the signal-to-noise ratio, it is often advantageous to average over a small region of neighboring pixels rather than analyzing each pixel individually. To determine absolute extinction values, it is necessary to define a background region in the scan where no absorbing material is present. The empty cavity reference allows all other points to be evaluated relative to it, enabling quantitative extinction mapping (see Figure 3.11 b). This technique provides highly sensitive, spatially and wavelength resolved extinction measurements, with the ability to resolve extinction down to 0.01%, a detection limit significantly lower than that of conventional methods.[98,104] When discussing the absorption of particles smaller than the diffraction limit of light, absorption does not occur uniformly across the beam but is instead localized at a small point within the beam's profile of the light field. In such cases, the absorption and the corresponding absorption cross-section mentioned in Equation 2.12 require a different interpretation. The absorption cross-section can also be interpreted as the total power absorbed by the particle divided by the local intensity at its position.[103,105] If a Gaussian beam with an effective area defined as in Equation 3.6.5 is assumed, the following expression for the absorption cross-section holds:

$$\sigma_{\mathrm{abs}} = B\frac{\pi w_0^2}{2} \tag{3.14}$$

where B is the absorption on a single pass of the light by the particle (in ppm). This value manifests in a modification of the cavity transmission amplitude and linewidth (see Figure 3.11 c).[106] It also implies that there is an upper limit to the absorption, determined by the initial intensity inside the cavity. Once all photons get absorbed after a single pass, B can no longer increase, and saturation sets in.

4

Design Rules for Perovskite Nanocrystals: Volume-Governed Absorption Versus Shape-Controlled Auger Recombination

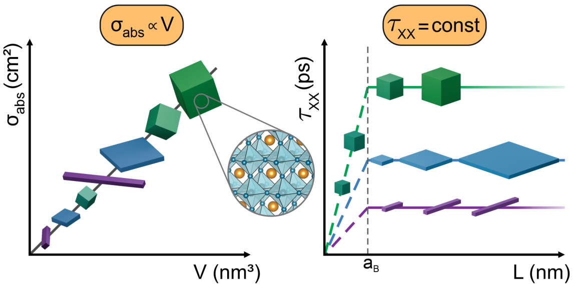

This chapter investigates the one-photon absorption cross-section and biexciton Auger lifetimes of $CsPbBr_3$ *nanocrystals, with varying dimensionality and size. Utilizing ultrafast transient absorption spectroscopy, the one-photon absorption cross-section and the biexciton Auger lifetime are measured. The resulting dataset represents the most extensive collection of measurements on the absorption cross-section of lead halide perovskite nanocrystals to date. It shows strong agreement with values reported in the literature. The universal volume scaling law of the biexciton Auger lifetime is confirmed for strongly confined nanocrystals, while deviations are observed in the weak confinement regime, where it saturates once the nanocrystal size exceeds the exciton Bohr radius. Furthermore, this saturation time depends on shape and confinement conditions, emphasizing the influence of morphology on carrier recombination dynamics. These findings provide a basis for optimizing perovskite nanocrystals for high-performance optoelectronic applications, including light-emitting diodes, lasers, and photodetectors. The results and figures presented in this chapter were published in Advanced Optical Materials in 2025.*[107]

4.1 Nanocrystal Volume Determination

Tailoring the shape and size of nanocrystals allows for control over optical properties relevant to specific applications. For instance, detectors benefit from a high one-photon absorption (OPA) cross-section, while applications such as high-power light-emitting diodes and lasers, which rely on high exciton densities and the suppression of non-radiative losses, require nanocrystals with long biexciton Auger lifetimes. Understanding how morphology influences these parameters is thus essential for guiding material design. To investigate their shape-dependent optical dynamics, nanocrystals were synthesized in three distinct morphologies (nanocubes, nanoplatelets, and nanorods), varying in edge length, thickness, and lateral size. A total of 24 nanocrystal samples were synthesized for this analysis. The nanocrystals were prepared using the three synthetic routes described in Section 3.1. Specific parameters for the LARP syntheses are provided in Table 4.1 at the end of this chapter. The nanocrystals must first be imaged to connect size and shape to their optical properties. As discussed in Subsection 3.3.1, different imaging methods are available for this purpose. Here, SEM and TEM were used to characterize the nanocrystal morphology. Figure 4.1 a shows representative images of nanocubes, 3ML nanoplatelets, and 3ML nanorods. From these images, datasets of approximately 100 nanocrystals per sample were evaluated by measuring their edge lengths (L); in the case of anisotropic shapes, the thickness (D) was also recorded. The corresponding histograms of L, shown in Figure 4.1 b, reveal that the inhomogeneity in edge length increases with decreasing dimensionality.

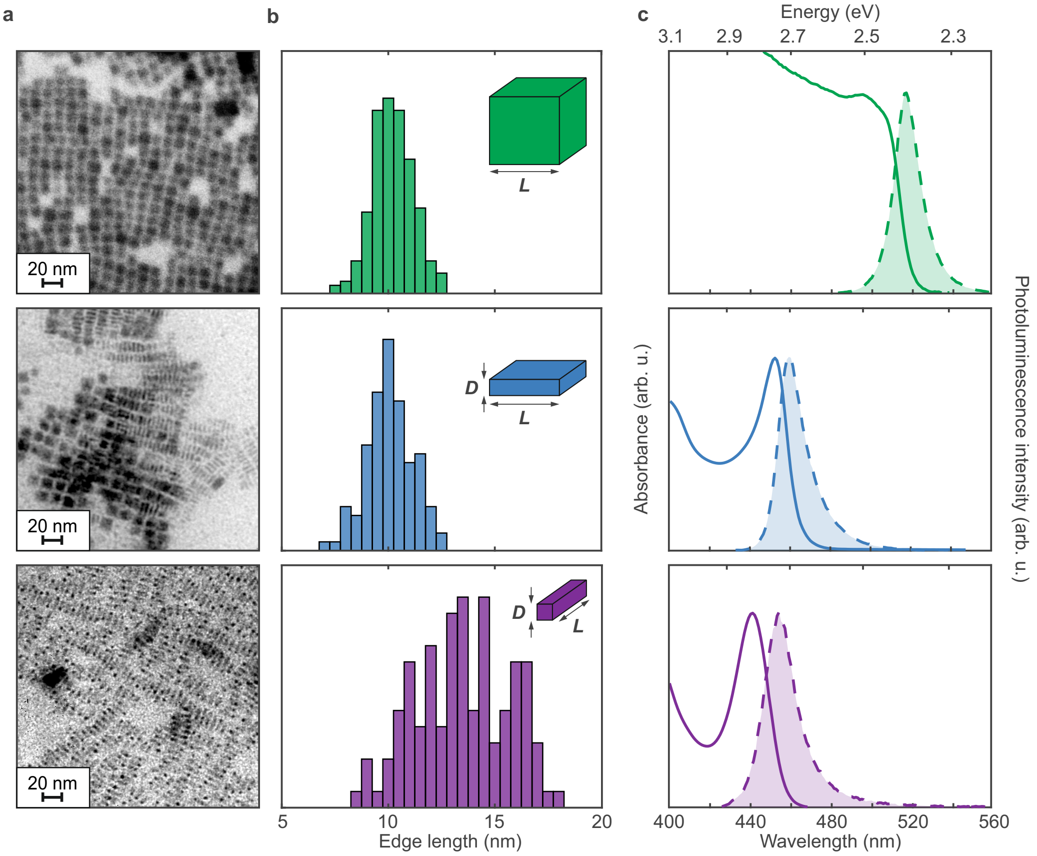

Figure 4.1: Structural and Optical Nanocrystal Characterization. **a)** Color-inverted SEM image of nanocubes (top, edge length: 10.5 ± 0.9 nm), TEM image of 3ML nanoplatelets in two orientations: standing on their edge and lying flat on the substrate (center, edge length: 10.3 ± 1.1 nm), TEM image of 3ML nanorods (bottom, edge length: 14.3 ± 1.7 nm). **b)** Corresponding histograms of their edge length distribution, with colored sketches indicating the shape of the nanocrystals. **c)** Absorption (solid) and PL (dashed) spectra of the respective samples.

Extracting the sizes of nanocrystals from SEM and TEM images comes with certain limitations. Nanocrystals are highly sensitive to electron beam irradiation, leading to rapid degradation during imaging.[108,109] This issue is particularly pronounced for thin nanoplatelets and nanorods, as they contain less material, making them more susceptible to degradation. Additionally, their thicknesses, the smallest being 1.2 nm (for 2ML), approach the resolution limit of the SEM and TEM, making accurate size determination difficult. While high-resolution TEM (HR-TEM) can partially mitigate this problem, it requires considerably more time and is more complex. HR-TEM was employed in previous studies to confirm the nanocrystal dimensions for selected thicknesses.[61,110] However, using it to image numerous samples is not ideal due to the complexity and time-consuming measurement procedure. Instead, optical characterization provides an indirect approach to size determination. As described in Subsection 2.5.2, quantum confinement significantly affects the optical properties of nanoplatelets and nanorods, leading to pronounced blue shifts in their absorption and PL spectra. Figure 4.1 c displays these spectra for nanocubes, 3ML nanoplatelets and 3ML nanorods. The weakly confined nanocubes exhibit a PL emission maximum at 518 nm (2.39 eV), consistent with their edge length of 10.5 ± 0.9 nm.[111] In contrast, the strong 1D confinement in 3ML nanoplatelets induces a blue shift of the PL peak to 459 nm (2.70 eV), while the even stronger 2D confinement in 3ML nanorods further shifts the PL emission to 454 nm (2.73 eV). Consequently, the 1s exciton absorption or PL peak position serves as a reliable indicator of the thickness of nanoplatelets and nanorods (see Figure 4.11).[54,82] When combined with SEM and TEM imaging, this approach enables accurate determination of the shape, thickness, and lateral dimensions of the nanocrystals. Ultimately, this results in a theoretical thickness determined by peak position and sample indication and a measured thickness where the measured values are extracted from the SEM and TEM images, further referred to as theoretical and measured thickness, respectively.

4.2 Fluence-Dependent Transient Absorption Spectroscopy

With the nanocrystal volume extracted from TEM and SEM imaging, each sample was subsequently measured using TAS to determine the OPA cross-section, σ_{abs}. Specifically, a femtosecond TAS setup was utilized to measure the OPA cross-section of 23 $CsPbBr_3$ nanocrystal samples with varying dimensions. Details on the setup can be found in Subsection 3.6.5. All measurements were conducted on colloidal dispersions of nanocrystals within a quartz cuvette with 2 mm path length. The *OD* at the excitation wavelength of 400 nm was maintained below 0.3 to ensure measurements remained inside the linear absorption regime. An advantage of the measurements in dispersion is that laser-induced heat dissipates quickly and does not damage the sample. A 270 fs laser pulse centered at 400 nm excites charge carriers within the electron-hole continuum of the nanocrystals, leading to time-dependent changes in the linear absorption spectrum. As shown exemplarily in Figure 4.2 a for 3ML nanoplatelets with an edge length of 10.3 ± 1.1 nm, the TA spectrum displays relative transmission variations ($\Delta T/T$). A prominent feature in this spectrum is the emergence of a photobleach signal around the 1s exciton position, which reflects a state-filling effect. Following excitation, charge carriers relax down to the 1s exciton state via phonon emission within $1-3$ ps. The occupation of the 1s exciton state results in an increase in transmission ($\Delta T/T$) at the 1s exciton peak, creating the photobleach signal that persists until the exciton state is depopulated. Figure 4.2 b shows snapshots of the wavelength-dependent TA spectra between 1 − 2000 ps. Although complex dynamics are observable, the aforementioned strong positive photobleach is the most important feature for the following analysis.

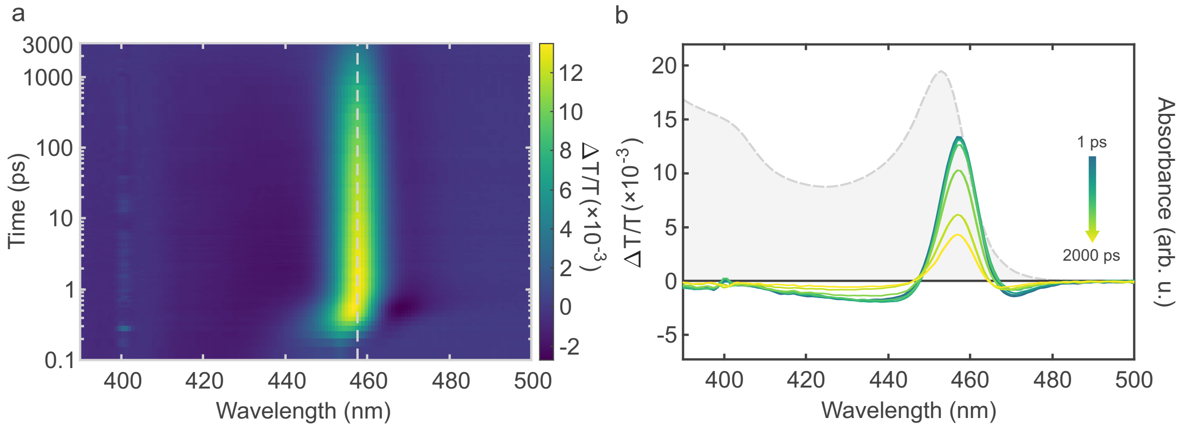

Figure 4.2: Transient Absorption Spectra. a) Representative 2D TA spectrum of 3ML nanoplatelets (edge length: 10.3 ± 1.1 nm). The exciton photobleach is marked with a dashed gray line. **b)** TA spectra of the same sample plotted against the wavelength at specific times between 1 − 2000 ps. Additionally, the steady-state linear absorption spectrum is depicted.

To better interpret the TA dynamics, their temporal evolution is considered in the next step. Figure 4.3 presents the fluence-dependent photobleach signal of 3ML nanoplatelets (edge length: 10.3 ± 1.1 nm) over time as an example. What immediately becomes evident is that the decay can be divided into three distinct temporal regions: an early-time region (up to 45 ps), an intermediate-time region (up to 400 ps), and a late-time region (up to 3000 ps). The exact boundaries of these regions are approximate, as the dynamics vary slightly between nanocrystal samples but generally fall within similar time frames. With increasing fluence, two main trends emerge: a substantial signal growth in the early-time region and fluence-independent decay dynamics in the late-time region.

Based on the assumption that photon absorption, and consequently exciton generation, follows Poissonian statistics, meaning that each nanocrystal initially absorbs a discrete number of photons, the OPA cross-section σ_{abs} can be determined.[112,113] Due to multiexciton processes happening within the first tens of picoseconds, at later times, each excited nanocrystal contains at most a single exciton. Additionally, the large spatial separation between nanocrystals in dispersion ensures that they do not interact, allowing each nanocrystal to be treated as an isolated system, eliminating any possibility of energy transfer between them.[114] Therefore, the late-time regime corresponds well to a regime of single-exciton recombination, where each exciton decays either radiatively or non-radiatively. For this reason, the analysis of σ_{abs} focuses on the late-time photobleach amplitude. TAS measurements were performed on each nanocrystal dispersion with fluences ranging from $1.5 - 141.9\,\mu\text{J}\,\text{cm}^{-2}$. The exact fluence values were determined using the method explained in detail in Equation 3.6.5. As the fluence increases, this late-time signal intensity rises and eventually saturates while its overall decay dynamics remain unchanged. This can be explained by the increasing proportion of excited nanocrystals up to a point where all nanocrystals within the excitation beam are excited, each hosting exactly one exciton. When all curves are normalized to a late-time value (2000 ps) as shown in Figure 4.4 a, the fluence-independent decay becomes more apparent. The normalized data clearly indicates that the decay behavior remains consistent across all fluences and can be accurately described by a monoexponential function, represented by a straight line which underlines the aforementioned theory of a single-exciton recombination regime.

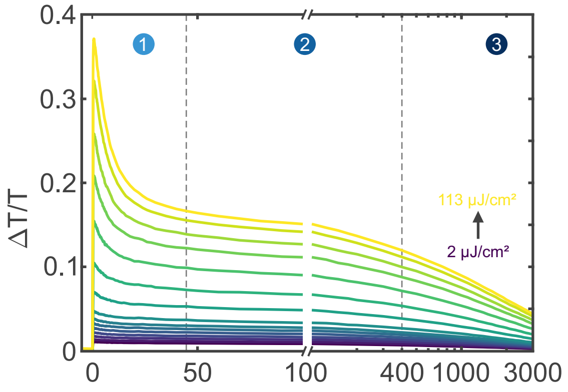

Figure 4.3: Time-Resolved Photobleach of 3ML Nanoplatelets. Time-dependent photobleach signals of 3ML nanoplatelets (edge length: 10.3 ± 1.1 nm) for different excitation fluences. The x-axis is separated at 100 ps with the first half being linear in scale and the second half logarithmic. The plot is further divided into three distinct regimes labeled from 1 (0 – 45 ps) to 3 (400 – 3000 ps).

4.3 One-Photon Absorption Cross-Section Determination

Consequently, the late-time photobleach signal is directly proportional to the exciton population in the nanocrystal ensemble and thus serves as an indicator of the number of excitons present. By combining this with the previously mentioned assumption that exciton generation follows Poisson statistics, the probability of having at least one exciton per nanocrystal can be expressed as:

$$P(N \geq 1) = 1 - P(N = 0) = 1 - \exp\left(-\langle N \rangle\right) \tag{4.1}$$

with $\langle N \rangle$ being the average number of excitons created per pulse in each nanocrystal. At any time of the measurement, the average exciton density per nanocrystal is proportional to the number of photons hitting the sample, n_{photons}. Knowing the energy of a single photon of the pump beam E_{photon} and the fluence of the pump beam F (defined as the energy per unit area and calculated as described in Equation 3.6.5), the number of photons hitting the sample under the beam spot can be computed as $n_{\text{photons}} = \frac{F}{E_{\text{photon}}}$ and it follows, $\langle N \rangle \propto \frac{F}{E_{\text{photon}}}$. That proportionality factor is defined as the OPA cross-section σ_{abs} of a single nanocrystal at the excitation wavelength:

$$\langle N \rangle = \sigma_{\text{abs}} \times \frac{F}{E_{\text{photon}}}. \tag{4.2}$$

Here, it is assumed that each absorbed photon generates a single exciton. Given the excitation wavelength and intensities used, the effects of multiple exciton generation and multiphoton absorption are expected to be negligible, validating this assumption. Furthermore, the OPA cross-section is strongly dependent on the wavelength. Subsequently, all OPA cross-sections determined in the following are for an excitation wavelength of 400 nm. To enhance the accuracy of the calculated fluence, it is considered that the fluence does not remain constant while traversing through the sample but decreases. This decrease can be expressed by the equation: $F(x) = F \times 10^{\frac{-Ax}{l}}$, where A is the absorbance of the sample (in units of OD), x represents the distance the laser beam has traveled through the sample, and l is the total path length.[115] This results in a slightly modified Equation 4.2:

$$\langle N \rangle(x) = \sigma_{\text{abs}} \times \frac{F(x)}{E_{\text{photon}}} \times 10^{\frac{-Ax}{l}} \tag{4.3}$$

As a last, step the late-time intensity of the photobleach signal ($\frac{\Delta T}{T}$) can be related to Equation 4.1 and, by combining the aforementioned equations, it can be written as:

$$\frac{\Delta T}{T} \propto \int_0^l \left(1 - \exp\left(-\sigma_{\text{abs}} \times \frac{F}{E_{\text{photon}}} \times 10^{\frac{-Ax}{l}}\right)\right) dx \tag{4.4}$$

with σ_{abs} being the only unknown in this equation, it can easily be deduced from the experimentally measured change of transmission. For that, the averaged late-time photobleach intensity is plotted against the excitation fluence, as shown in Figure 4.4 b for the 3ML nanoplatelets with an edge length of 10.3 ± 1.1 nm. The intensity is numerically fitted with Equation 4.4 and an excellent fit is achieved, which yields an OPA cross-section of $\sigma_{\text{abs}} = (1.82 \pm 0.06) \times 10^{-14}\text{cm}^2$, closely matching previous literature results of nanocrystals with similar shape and size.[116,117]

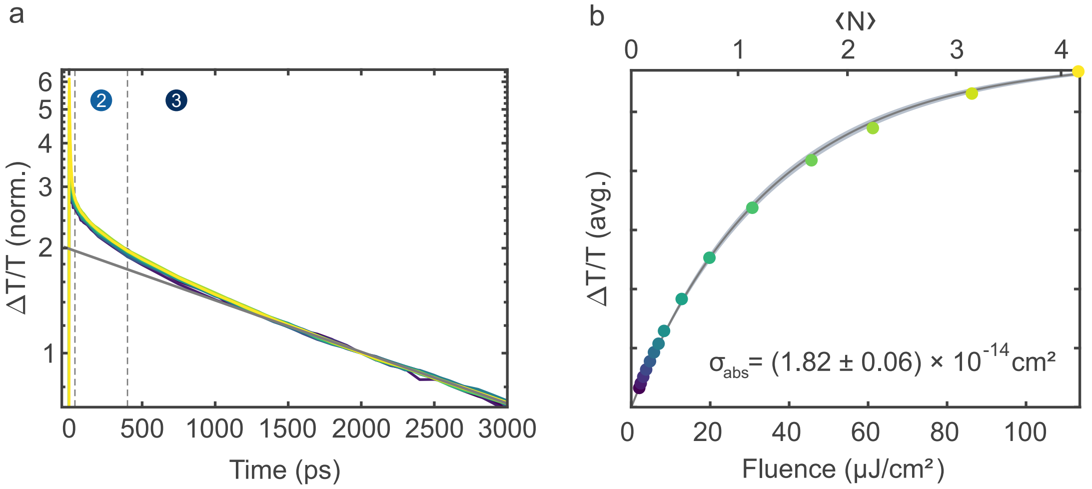

Figure 4.4: Late-Time Photobleach and OPA Cross-Section Extraction. a) Time-dependent photobleach signals of 3ML nanoplatelets (edge length: 10.3 ± 1.1 nm) for different excitation fluences and normalized at 2000 ps. A monoexponential decay (gray line) reproduces the fluence-independent behavior well. **b)** The photobleach intensity is averaged at late times (1500 – 3000 ps), and the resulting intensities are plotted against the excitation fluence. The OPA cross-section is extracted from a fit to this data.

This procedure was performed for 23 nanocrystal samples, resulting in an OPA cross-section at 400 nm for each sample. To quantify the dependence of the OPA cross-section on the nanocrystal volume (V_{NC}), the extracted OPA cross-sections are plotted against the theoretical and measured volumes (see Figure 4.5 a and Figure 4.5 b, respectively). For both the theoretical and the measured volumes, a linear dependence of the OPA cross-section can be observed. A linear fit to the data results in a slope of $(12.1 \pm 1.0) \times 10^{-17}\text{cm}^{-1}$ for theoretical and $(8.3 \pm 0.4) \times 10^{-17}\text{cm}^{-1}$ for the measured thickness of the nanocrystals. Consequently, the OPA cross-section does not depend on the dimensionality of the nanocrystals but only on their volume. This corresponds well with previous theoretical and experimental studies, including studies on CdSe nanocrystals, PbSe nanorods, and lead halide perovskite nanocrystals with different shapes and sizes.[114–116,118–121] Yet to date, these measurements constitute the most extensive data set on one type of material. These findings demonstrate that the OPA cross-section is a universal property governed solely by the nanocrystal volume, regardless of shape or dimensionality. As a result, σ_{abs} can serve as a reliable parameter for estimating nanocrystal volume without requiring detailed knowledge of optical properties or morphology. Contrarily, measuring the OPA cross-section alone allows for an estimate of nanocrystal volume, even without prior knowledge of the specific shape or dimensionality.

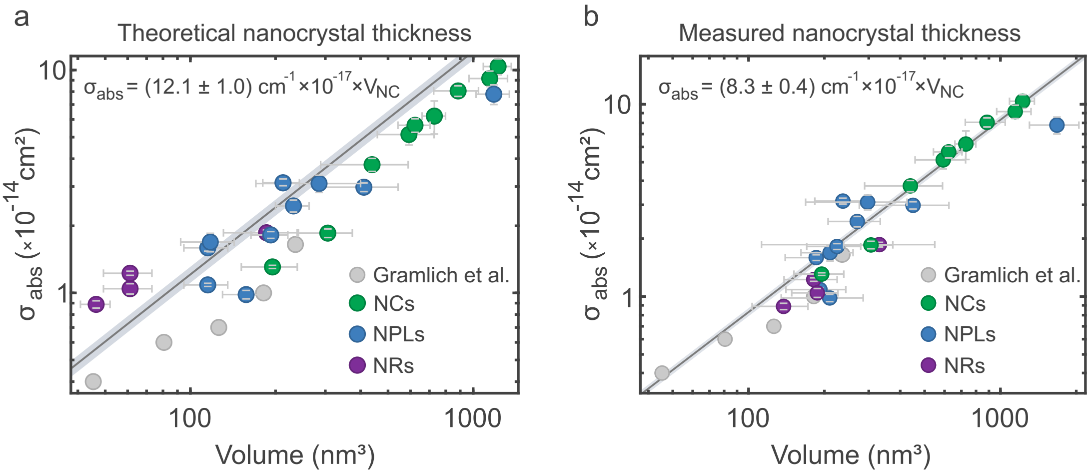

Figure 4.5: Volume-Dependent OPA Cross-Section. OPA cross-sections from nanocube, nanoplatelet, and nanorod samples (NC, NPL, and NR, respectively) versus their volumes depicted in a log-log plot. Volumes were calculated with the theoretical thicknesses (a) and the measured thicknesses (b). Literature values from Gramlich et al. are included as gray data points.[114] The dark gray line represents a linear fit to the data, with the corresponding volume dependence and slope indicated in the respective figure. V_{NC} refers to the general nanocrystal volume.

4.4 Biexciton Auger Lifetime Determination

With the late part of the signal analyzed, attention is turned to the previously mentioned signal increase of the early part, which only emerges at higher fluences and vanishes within the first few tens of picoseconds. To systematically analyze the early part of the signal, a triexponential function of the form $A_1e^{-t/\tau_1} + A_2e^{-t/\tau_2} + A_3e^{-t/\tau_3}$ is fitted to each fluence-dependent decay curve. This choice is justified by three distinct temporal regimes, each separated by at least one order of magnitude in timescale (as already described above). Applying this method allows for an accurate description of the decay dynamics across all three temporal domains. Attempts at monoexponential and biexponential fits failed to reproduce the measured dynamics, while a four-exponential model added unnecessary complexity without a plausible physical process for the fourth decay. Therefore, the triexponential model is identified as the optimal compromise between fit quality and interpretability. An example of

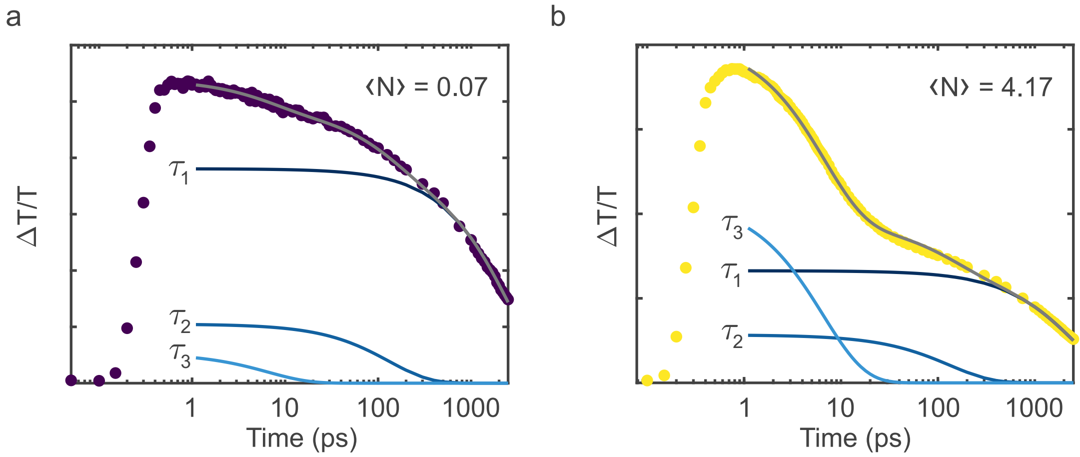

Figure 4.6: Fluence-Dependent Photobleach Dynamics in 3ML Nanoplatelets. Time-dependent exciton photobleach signals of 3ML nanoplatelets (edge length: 10.3 ± 1.1 nm) excited with low (a) and high (b) fluence. The signals are fitted with a triexponential function (gray curve), and their respective components ($A_ie^{-\frac{t}{\tau_i}}$) are depicted separately as blue curves labeled with $\tau_1 - \tau_3$.

the fit applied to the lowest and highest fluence measurements is depicted in Figure 4.6 on a semi-logarithmic scale for 3ML nanoplatelets (edge length: 10.3 ± 1.1 nm). The fit (gray curve) accurately reproduces the experimental data in both cases. Furthermore, the individual contributions of the three decay components are plotted as separate blue curves. The relative amplitudes of these components provide clear insight into how the overall decay dynamics evolve with fluence. A critical aspect to consider is the starting time of the fit. In this example, the fit begins at 1 ps, a choice dictated by the hot-carrier cooling process. This ultrafast thermalization of excited charge carriers to the band edge is already observable in Figure 4.2, where a slight red-shift in the photobleach maximum within the first picosecond indicates its presence. The hot-carrier cooling rate depends on the excess energy that charge carriers acquire during excitation.[122] Given that all measurements were conducted using 400 nm as the excitation wavelength, the excess energy increases for lower bandgap energy or comparable weaker quantum confinement. To minimize the influence of this effect on the fitting procedure, the fits were applied after charge carrier cooling has subsided. The relaxation time depends on the size and shape of the nanocrystals, necessitating different starting times: 1 ps for nanoplatelets and nanorods and 3 ps for nanocubes. Examples illustrating hot-carrier cooling at both low and high fluences are provided in Figure 4.7 a for 2ML nanoplatelets, and in Figure 4.7 b for nanocubes.

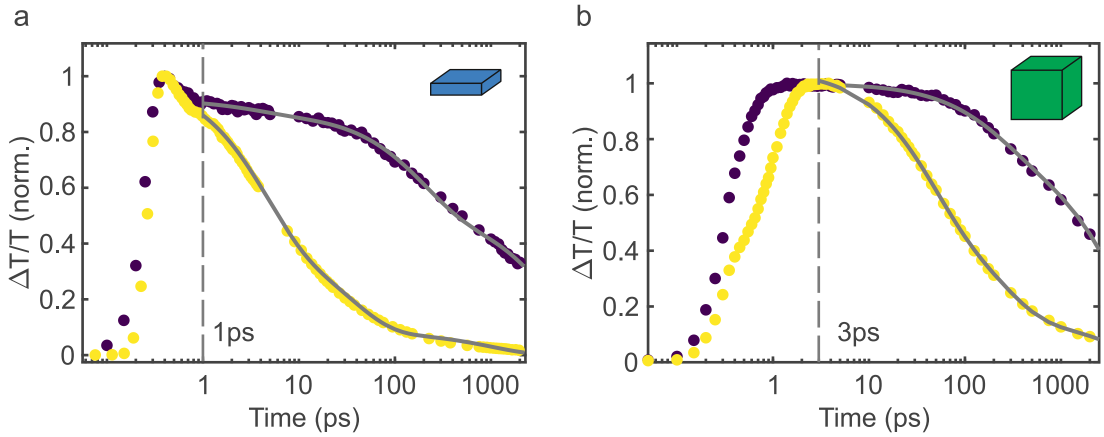

Figure 4.7: Hot-Carrier Cooling. Examples of time-dependent exciton photobleach signals of 2ML nanoplatelets (edge length: 31 ± 3 nm) (a) and nanocubes (edge length: 10.7 ± 0.7 nm) (b) excited with low (purple) and high (yellow) fluence. Dashed lines at 1 ps and 3 ps indicate the starting points of the gray fitting curves. This prevents hot-carrier cooling from influencing the fit.

By extracting the amplitudes and decay times of each exponential component and plotting them as a function of fluence, the charge carrier dynamics can be examined. For instance, Figure 4.8 a presents the fluence-dependent decay times (τ_1, τ_2, and τ_3) for 3ML nanoplatelets (edge length: 10.3 ± 1.1 nm). This data again highlights the differences in absolute decay times of each time regime. Notably, the decay times, and thus the associated decay processes, exhibit minimal dependence on fluence. Slight deviations are observed for τ_2 and τ_3 at very low fluences due to their relatively small contributions to the overall signal in this regime. Since this effect purely stems from the fitting procedure and has no physical origin, an inverse-variance weighting error estimation was performed to calculate a final mean decay time value for all three regimes. This ensures that data points with high uncertainty contribute less to the final result. Taking this into account, the calculated decay times for these 3ML nanoplatelets are $\tau_1 = 2612 \pm 21$ ps, $\tau_2 = 141 \pm 5$ ps and $\tau_3 = 6.8 \pm 0.1$ ps. Furthermore, the relative contributions of the individual decay components to the photobleach signal vary significantly with laser fluence, as illustrated in Figure 4.8 b. There, the relative amplitudes as fractions of the total amplitude sum ($A_i/(A_1 + A_2 + A_3)$) are presented. At low fluences, the slow τ_1 component dominates the overall decay, whereas the faster τ_3 component becomes more prominent at higher fluences. In contrast, the intermediate τ_2 component remains largely fluence-independent.

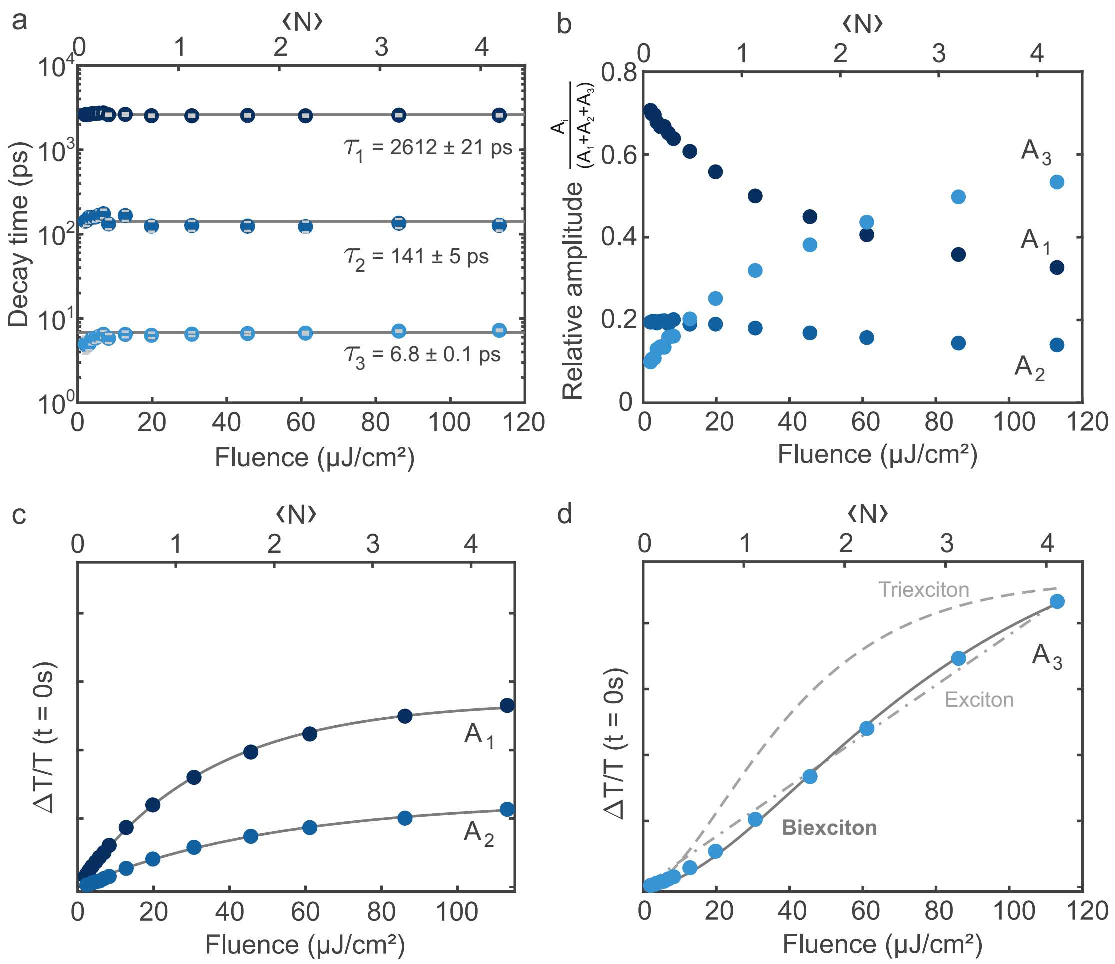

Figure 4.8: Fluence-Dependent Photobleach Analysis for 3ML Nanoplatelets. a) Extracted lifetimes from the triexponential fit of 3ML nanoplatelets (edge length: 10.3 ± 1.1 nm) for increasing fluence. The corresponding average lifetimes are depicted as gray lines. **b)** Relative amplitudes $A_1 - A_3$ extracted from the triexponential fit, normalized to the amplitude sum and plotted against the excitation fluence. **c)** The components A_1, A_2 are fitted with the Poisson probability (gray curve) of at least one exciton per nanocrystal. **d)** A_3 fitted with the Poisson probability of at least one (dash-dotted gray curve), two (gray curve) or three (dashed gray curve) excitons per nanocrystal.

To determine the nature of the individual processes, Poissonian statistics are again considered. Depending on whether single or multiple excitons are involved in these decay processes, the dependence on laser fluence should vary significantly. As shown before by Yarita et al., such amplitude curves can be fitted with Poisson statistics.[123] Following the Poisson distribution, the probability of creating at least an exciton P_X, a biexciton P_{XX} or a triexciton P_{XXX} is given by:

$$P_X(F) = 1 - e^{-\sigma_{\text{abs}} \frac{F}{E_{\text{photon}}}} \tag{4.5}$$

$$P_{XX}(F) = 1 - e^{-\sigma_{\text{abs}} \frac{F}{E_{\text{photon}}}} \left(1 + \sigma_{\text{abs}} \frac{F}{E_{\text{photon}}}\right) \tag{4.6}$$

$$P_{\mathrm{XXX}}(F) = 1 - e^{-\sigma_{\mathrm{abs}}\frac{F}{E_{\mathrm{photon}}}}\left(1 + \sigma_{\mathrm{abs}}\frac{F}{E_{\mathrm{photon}}} + \frac{\left(\sigma_{\mathrm{abs}}\frac{F}{E_{\mathrm{photon}}}\right)^2}{2}\right) \tag{4.7}$$

The excellent correlation obtained from fitting the amplitude curves of τ_1 and τ_2 to Equation 4.5 confirms their single-exciton nature (see Figure 4.8 c). When combined with prior results, this strongly suggests that the slow decay component τ_1 corresponds to simple exciton recombination, either radiative or non-radiative. Further support for this assignment is provided by the extracted τ_1 values across all samples (see Table 4.2), which show no clear dependence on nanocrystal size or shape. This aligns with the understanding that exciton recombination is influenced by multiple factors, such as surface defect density, detrapping probability, and PLQY. However, beyond identifying the nature of the process, no additional conclusions can be drawn without further investigations. The intermediate decay time τ_2 also shows single-exciton characteristics and was previously linked to charge carrier trapping, which may facilitate trion formation in perovskite nanocubes.[123] Given that trap states in nanocrystals predominantly originate from surface defects, their influence on τ_2 is expected to be significant. In prior studies on 2ML $CsPbBr_3$ nanoplatelets, a post-synthetic treatment with a $PbBr_2$-ligand solution was used to actively repair surface defects. This treatment led to the near-complete suppression of the intermediate decay component.[47] To further verify this interpretation, the extracted τ_2 values are plotted against the surface-to-volume ratio of each of the 24 nanocrystal samples, revealing a clear correlation (see Figure 4.9 a). This relationship is quantitatively supported by a Spearman correlation coefficient of $r_s = -0.91$, which provides strong evidence for the origin of the intermediate decay process.

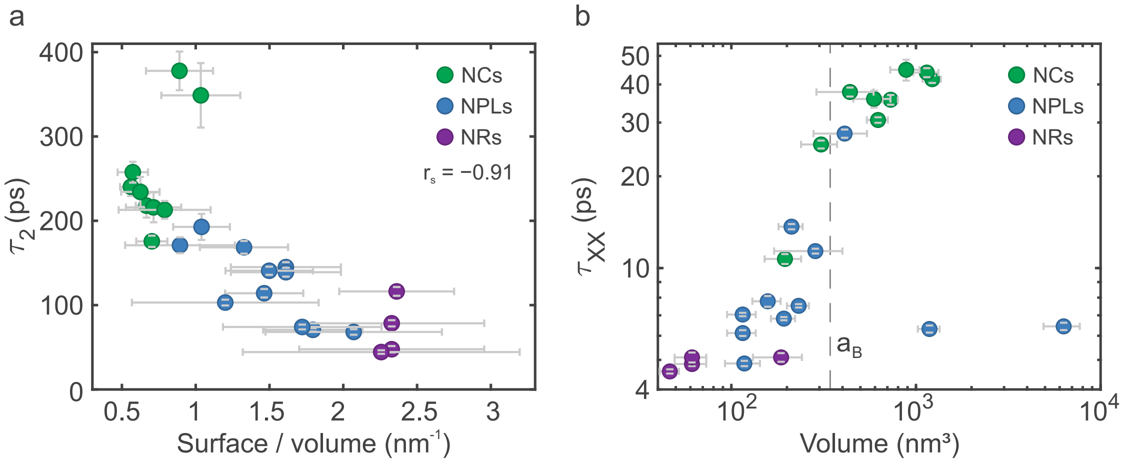

Figure 4.9: Correlation of Decay Times with Nanocrystal Dimensions. **a)** Trap-mediated decay time τ_2 plotted against the surface-to-volume ratio of all 24 nanocrystal samples. A Spearman correlation of $r_s = -0.91$ indicates a strong negative correlation, suggesting that as the surface-to-volume ratio increases, τ_2 tends to decrease. **b)** Biexciton Auger lifetime plotted against the nanocrystal volume. The nanocube, nanoplatelet, and nanorod (NC, NPL, and NR, respectively) volumes were calculated using the theoretical thicknesses.

In contrast, the amplitude trend of the fastest decay component, τ_3, reveals that it cannot be described by a single-exciton decay process (see Figure 4.8 d). Instead, among the three aforementioned probabilities P_{X}, P_{XX}, and P_{XXX}, the best fit is achieved with P_{XX}. This indicates that the decay process with the decay time τ_3 is of biexcitonic nature. The stability of the τ_3 values across the entire fluence range suggests that charge carrier dynamics remain unchanged. Even though the fluence is high enough to create $\langle N \rangle = 4.17$ excitons per nanoplatelet on average, there is no sign of higher-order multiexcitons. This was previously observed for $CsPbBr_3$ nanocubes and explained in Subsection 2.2.3 and confirms the twofold degeneracy of the band-edge states.[124–126] Furthermore, the fastest decay time, τ_3, can be exclusively connected to the biexciton Auger (or exciton-exciton annihilation) lifetime usually denoted by τ_{XX}. This analysis was performed on all 24 investigated nanocrystal samples, and all samples showed similar results in the quantitative amplitude and decay time behavior. The extracted parameters can be found in Table 4.2. As a side note, it was also tested to employ the amplitude curve of A_1 in combination with Equation 4.5 to calculate the OPA cross-section of the nanocrystal dispersion. And, indeed, the OPA cross-section extracted via the amplitude fit method $\sigma_{A_1} = (1.88 \pm 0.06) \times 10^{-14}\,\text{cm}^2$ falls within the error margin of the previously obtained value from the intensity averaging method $\sigma_{\text{avg}} = (1.82 \pm 0.06) \times 10^{-14}\,\text{cm}^2$. This simplifies the overall analysis procedure. Instead of averaging $\Delta T/T$ first, fitting it with the Poisson probability to extract an OPA cross-section, and subsequently applying the triexponential function, the function can be fitted directly with the triexponential function. This allows for the simultaneous extraction of the OPA cross-section, the decay behavior, and the individual decay times.

Following the approach used for the OPA cross-section analysis, the biexciton Auger recombination lifetime is now examined in relation to the nanocrystal volume. Since no distinct trend can be identified when τ_{XX} is plotted against volume (see Figure 4.9 b), a more systematic approach is required. As a first step, nanocubes are considered separately to eliminate shape-dependent anomalies. The corresponding data is shown in Figure 4.10 a.

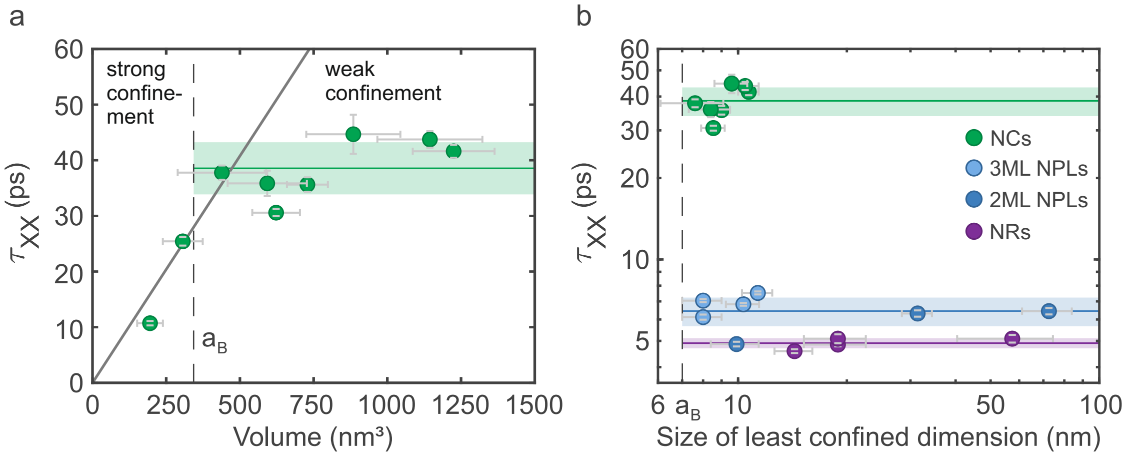

Figure 4.10: Volume and Dimensional Scaling of Biexciton Auger Lifetimes. a) Biexciton Auger lifetime of nanocubes plotted against their volume. A linear fit (gray line) confirms the universal volume scaling law for nanocubes in the strong confinement regime. The biexciton Auger lifetime saturates for nanocubes with volumes exceeding a_B^3 constituting a transition between the weak and strong confinement regimes. **b)** Biexciton Auger lifetime as a function of the size of the least confined dimension of nanocubes, 2 and 3ML nanoplatelets and 3ML nanorods (NCs, NPLs, and NRs, respectively). A saturation behavior for all three shapes can be seen. The colored lines indicate mean values of τ_{XX} with colored bands showing the respective standard deviation.

To specify a boundary between strong and weak confinement regimes, the exciton Bohr radius, a_B, serves as a reference. For $CsPbBr_3$, a_B is approximately 7 nm, corresponding to a volume of 330 nm^3.[8] A distinct difference is observed between nanocubes with edge lengths below and above this threshold. In the strong confinement regime, a linear dependence of the biexciton Auger lifetime on nanocube volume is evident, as confirmed by the linear fit (gray line). This behavior is consistent with the universal volume scaling law, which states that the biexciton Auger lifetime scales linearly with nanocrystal volume, independent of material composition. This law has been empirically validated across multiple nanocrystal systems, including lead halide perovskite nanocubes.[112,127–131] However, this trend transitions into a saturation behavior in the weak confinement regime where the biexciton Auger lifetime stays constant for larger nanocube volumes. A mean lifetime value (green line) with the corresponding standard deviation (transparent green band) illustrates the observed behavior. The extracted biexciton Auger lifetime for nanocubes in the weak confinement regime, with edge lengths ranging from 7.6 ± 1.5 nm to 10.7 ± 0.7 nm is $\tau_{\mathrm{XX}} = 38.6 \pm 4.7$ ps. This value has also been reported as the saturation limit in the literature.[120,124] The observed trend reversal in biexciton Auger lifetime relative to nanocube volume underscores the critical role of quantum confinement. The transition from a linear dependence in the strong confinement regime to saturation behavior in the weak confinement regime highlights the exciton Bohr radius as a significant boundary and demonstrates how quantum confinement influences the volume dependence of τ_{XX}. While confinement and volume are more obviously related in nanocubes, this relationship differs significantly for nanoplatelets and nanorods. Generally, τ_{XX} further decreases with decreasing volume, but not with a clear trend (see Figure 4.9 b). Moreover, the boundary of weak and strong confinement varies, as nanoplatelets have one, and nanorods have two strongly confined dimensions. This makes the volume an insufficient parameter for describing the τ_{XX} scaling across different shapes.[114,132,133] Therefore, an alternative approach is necessary to accurately describe the biexciton Auger lifetime across different nanocrystal morphologies.

To compare different morphologies and, simultaneously, edge lengths of the nanocrystal samples, the concept of a least confined dimension (LCD) is introduced. As shown in Figure 4.1 b, the size of the LCD, L_{LCD} differs depending on the dimensionality of the nanocrystal. For 3D nanocubes, all sides have the same length so that $\sqrt[3]{V_{\mathrm{NC}}} = L_{\mathrm{LCD}}$. For 2D nanoplatelets, the quantum confinement is introduced from the thickness of the nanoplatelets, and their edge length defines the size of the LCD. Finally, for 1D nanorods, as they are confined in two dimensions, $L_{\mathrm{NR}} = L_{\mathrm{LCD}}$. To systematically examine the dependence of τ_{XX} on dimensionality, Figure 4.10 b presents its variation with L_{LCD} for 3ML nanorods, 2ML and 3ML nanoplatelets, as well as nanocubes of all sizes. To maintain clarity, nanocubes with edge lengths smaller than the exciton Bohr radius (indicated by the dashed gray line) have been excluded. A key observation is that the previously identified saturation behavior in nanocubes extends to lower-dimensional structures. Notably, the biexciton Auger lifetime saturates for 2 and 3ML nanoplatelets as well as for 3ML nanorods. For nanoplatelets, this saturation occurs across edge lengths ranging from 8.0 ± 1.0 nm to 73 ± 11 nm, with $\tau_{\mathrm{XX}} = 6.5 \pm 0.8$ ps. Similarly, for 3ML nanorods with lengths between 14.3 ± 1.7 nm and 57.4 ± 17 nm, $\tau_{\mathrm{XX}} = 4.9 \pm 0.2$ ps. These findings suggest that τ_{XX} is mainly independent of the LCD. This trend aligns with the aforementioned observations where quantum confinement significantly influenced the PL and absorption spectra (Figure 4.1 c). The reduction in dimensionality from nanocubes to nanoplatelets induces a substantial decrease in τ_{XX}, yet even stronger confinement in two dimensions for nanorods leads to a negligible change. This suggests that once biexcitons are confined in one dimension, additional restriction has a diminishing impact, even when the LCD varies significantly. It is important to note that these findings are drawn based on the accessible size range, as synthesis limitations currently prevent the fabrication of significantly larger nanocubes and nanoplatelets and longer nanorods. Additionally, sedimentation is an inherent challenge in measuring larger structures, where nanocrystals gradually sink over time, altering the sample composition during the measurement. While this effect could be mitigated by continuous sample agitation, implementing such a solution would require complex modifications to the experimental setup.

4.5 Summary and Discussion

In conclusion, TAS was used to investigate exciton dynamics in $CsPbBr_3$ nanocrystals with varying size and dimensionality. The OPA cross-section and three distinct decay times were extracted from fluence-dependent photobleach signals. The OPA cross-section was found to scale linearly with nanocrystal volume, independent of nanocrystal shape, with a slope of $(12.1 \pm 1.0) \times 10^{-17}\,\mathrm{cm}^{-1}$. This universal volume scaling enables the straightforward estimation of absorption in thin films from only knowing the nanocrystals' size. Analysis of the excitonic decay dynamics revealed three distinct recombination regimes. Firstly, biexcitonic Auger recombination (τ_{XX}) occurs within the first 40 ps after excitation. Secondly, exciton trapping with potential trion formation (τ_2) dominates the intermediate time regime, with lifetimes between $40 - 400$ ps. A clear correlation with the surface-to-volume ratio supports the interpretation that this process is due to surface traps. Finally, single-exciton recombination (τ_1) occurs on nanosecond timescales ($2 - 7$ ns) and was independent of morphology, suggesting that it is influenced by many factors not investigated here.

Further investigation into biexcitonic Auger recombination revealed a saturation behavior for τ_{XX} in the weak confinement regime. This saturation depends primarily on the most strongly confined dimension, with little to no dependence on the LCD. Accordingly, nanorods exhibited the shortest biexciton Auger lifetimes of ≈ 5 ps, whereas the τ_{XX} of nanoplatelets increased with thickness from 2 to 7ML ($6 - 28$ ps), approaching the 40 ps limit observed for weakly confined nanocubes. Potential mechanisms such as weakened dielectric screening or exciton delocalization may underlie this saturation and have to be addressed in future theoretical work. The data aligns well with previous findings on CdSe and $CsPbBr_3$ systems. She et al. reported a similar saturation of τ_{XX} in CdSe nanoplatelets beyond lateral areas of $\approx 130\,\mathrm{nm}^2$, while Philbin et al. found a linear scaling of the biexciton Auger lifetime with area up to $\approx 100\,\mathrm{nm}^2$, suggesting a plateau beyond that regime.[134,135]

These results also offer valuable guidance for optimizing nanocrystals in light-emitting or light-harvesting devices. Smaller nanocrystals provide strong confinement and tunable emission but suffer from faster Auger recombination. Larger nanocrystals are beneficial for absorption-based applications if trap densities can be controlled. Intermediate, weakly confined nanocrystals could balance absorption strength, reduced non-radiative loss, and manageable trap densities, though with trade-offs in directional emission and outcoupling efficiency.

Appendix

Table 4.1: Synthesis Parameters. Detailed synthesis parameters of samples synthesized via LARP at RT.

#	V_{PbBr_2} (µL)	c_{PbBr_2} (M)	V_{Cs} (µL)	c_{Cs} (M)	Antisolvent	$V_{\mathrm{Antisolvent}}$ (µL)
1	2000	-	200	0.07	-	-
2	2000	-	200	0.08	-	-
10	1000	0.01	100	0.02	Cyclopentanone	2000
11	1500	0.01	150	0.02	Methanol	500
12	3000	0.01	150	0.02	Ethanol	2000
13	1500	0.01	150	0.02	Ethanol	2000
14	3000	0.01	150	0.02	Acetone	2000
15	300	0.045	25	0.02	Butanol	3300
16	1645	0.004	100	0.02	Cyclopentanone	1250
17	300	0.045	25	0.02	Butanol	3300
18	1500	0.01	150	0.02	Cyclopentanone	2000
19	3000	0.01	150	0.02	Methyl acetate	2000
20	2385	0.033	68	0.02	Butanol	4435
21	1500	0.01	150	0.02	Acetone	2000
22	1500	0.01	150	0.02	Acetone	2000
23	1500	0.01	150	0.02	Acetone	2000
24	1500	0.01	150	0.1	Acetone	2000

Table 4.2: Sample Parameters. Overview of parameters of all 24 investigated nanocrystal samples: nanocubes, nanoplatelets, and nanorods (NC, NPL, and NR, respectively).

#	Shape	Edge length (nm)*	Thickness (nm)*	Theoretical thickness (nm)**	$\sigma_{\text{abs}}(10^{-14}cm^2)$	τ_1 (ps)	τ_2 (ps)	τ_3 (ps)
1	NC	5.8 ± 0.8	-	-	1.31 ± 0.02	5877 ± 191	349 ± 38	10.7 ± 0.4
2	NC	6.7 ± 0.9	-	-	1.86 ± 0.08	6940 ± 234	378 ± 23	25.4 ± 0.8
3	NC	7.6 ± 1.5	-	-	3.76 ± 0.25	7500 ± 225	213 ± 11	37.8 ± 1.3
4	NC	8.4 ± 1.1	-	-	5.1 ± 0.5	4346 ± 350	216 ± 18	35.9 ± 2.3
5	NC	8.5 ± 0.6	-	-	5.65 ± 0.40	4539 ± 100	176 ± 7	30.6 ± 0.6
6	NC	9.0 ± 0.5	-	-	6.2 ± 1.1	4819 ± 335	218 ± 14	35.6 ± 1.3
7	NC	9.6 ± 1.0	-	-	8.06 ± 0.44	4836 ± 219	234 ± 18	44.7 ± 3.5
8	NC	10.5 ± 0.9	-	-	9.2 ± 0.7	3763 ± 232	258 ± 12	43.7 ± 1.5
9	NC	10.7 ± 0.7	-	-	10.4 ± 0.9	4047 ± 263	240 ± 11	41.6 ± 1.2
10	NPL	7.1 ± 0.8	4.7 ± 0.8	4.2	3.14 ± 0.11	4344 ± 71	193 ± 16	13.6 ± 0.3
11	NPL	8.0 ± 1.0	2.9 ± 0.5	1.8	1.59 ± 0.06	3422 ± 33	139 ± 5	7.0 ± 0.1
12	NPL	8.0 ± 1.0	3.0 ± 0.6	1.8	1.09 ± 0.02	3346 ± 26	145 ± 6	6.1 ± 0.1
13	NPL	8.1 ± 1.0	3.2 ± 1.0	2.4	0.98 ± 0.04	4559 ± 54	169 ± 8	7.8 ± 0.3
14	NPL	9.9 ± 1.5	2.2 ± 0.2	1.2	1.69 ± 0.16	2333 ± 27	68 ± 3	4.9 ± 0.1
15	NPL	10.3 ± 1.1	2.1 ± 0.4	1.8	1.82 ± 0.06	2612 ± 21	141 ± 5	6.8 ± 0.1
16	NPL	10.9 ± 3.1	2.5 ± 0.4	2.4	3.10 ± 0.27	5408 ± 93	103 ± 3	11.4 ± 0.2
17	NPL	11.3 ± 1.1	2.1 ± 0.4	1.8	2.46 ± 0.15	3162 ± 26	114 ± 5	7.5 ± 0.1
18	NPL	12.7 ± 4.0***	4.6 ± 1.0	4.2	2.98 ± 0.13	6076 ± 233	171 ± 10	27.6 ± 0.9
19	NPL	31 ± 3	1.7 ± 0.3	1.2	7.8 ± 0.8	2223 ± 65	71 ± 2	6.3 ± 0.2
20	NPL	73 ± 11	1.6 ± 0.2	1.2	-****	1811 ± 79	74 ± 3	6.4 ± 0.2
21	NR	14.3 ± 1.7	3.1 ± 0.3	1.8	0.89 ± 0.03	3365 ± 30	116 ± 5	4.6 ± 0.1
22	NR	18.9 ± 3.7	3.1 ± 0.3	1.8	1.23 ± 0.03	2453 ± 17	79 ± 4	4.8 ± 0.1
23	NR	18.9 ± 3.7	3.1 ± 0.3	1.8	1.05 ± 0.06	2562 ± 37	48 ± 4	5.1 ± 0.2
24	NR	57.4 ± 17	2.4 ± 1.0	1.8	1.86 ± 0.05	2919 ± 33	44 ± 2	5.1 ± 0.2

* The edge lengths and thicknesses were extracted from SEM or TEM images with sample sizes of around 100 nanocrystals.

** The theoretical thicknesses were determined according to the position of the 1s exciton absorption peaks.[54,82]

*** This sample is asymmetric and has a width of 7.7 ± 0.5 nm.

**** It was not possible to extract an OPA cross-section from this sample.

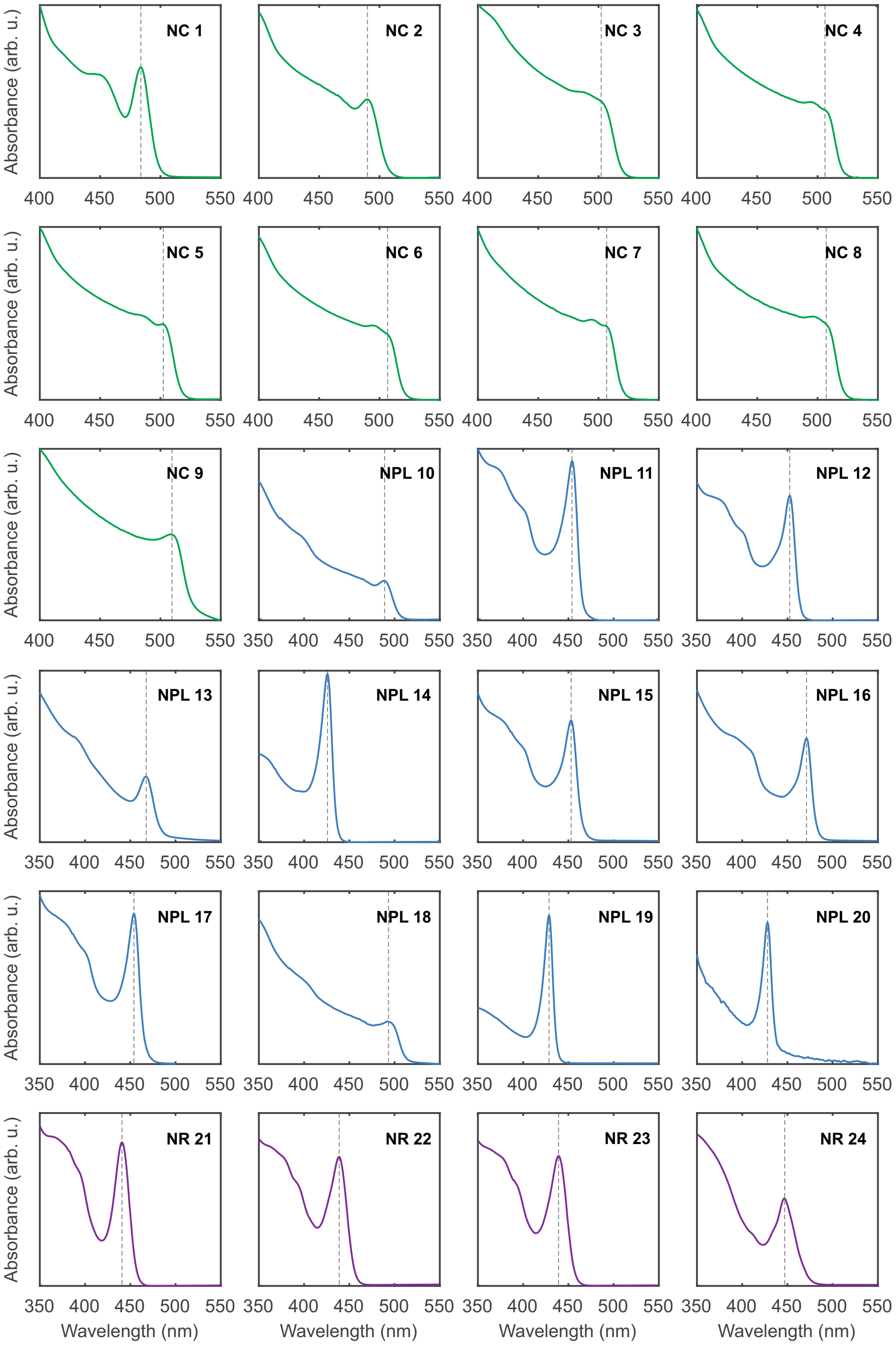

Figure 4.11: Absorption Spectra of All Investigated Samples. Linear absorption spectra of all 24 nanocrystal samples, indexed with their corresponding shape and number from Table 4.2. The dashed gray lines indicate the position of the 1s exciton absorption peak.

5

Towards Correlated Single-Particle Absorption and Photoluminescence Spectroscopy of Perovskite Nanocrystals

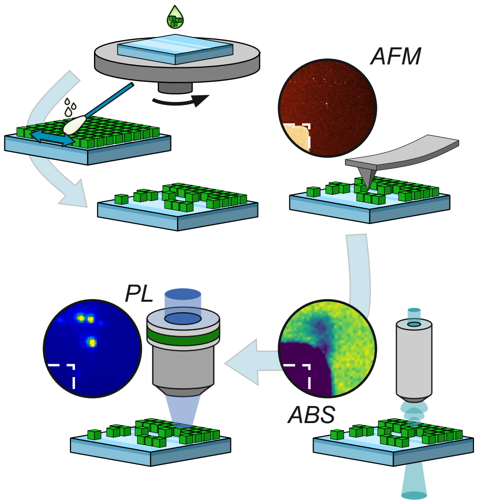

This chapter presents the first direct determination of the absorption cross-section of $CsPbBr_3$ nanocubes using CEES. To enable such measurements, a new wiping-based film preparation method was developed, producing spatially isolated nanocube clusters on DBR mirror substrates. Since SEM imaging was not feasible on these mirrors, a correlation between AFM and SEM was established, allowing the number of nanocubes per cluster to be inferred from AFM data alone. By analyzing CEES extinction data from clusters of increasing size, the absorption cross-section of a single nanocube could be extrapolated. In addition, CEES enables the study of nanocube degradation beyond the point where PL is completely quenched, offering access to study strongly degraded nanocrystals. Furthermore, low-temperature PL spectroscopy was carried out on the same sample regions, making it possible to combine AFM, CEES, and PL data on identical nanocrystal ensembles for the first time.

5.1 Measurement Preparations

Building on the ensemble-based absorption cross-section measurements via TAS in the previous chapter, this chapter shifts the focus to the direct measurement of the absorption cross-section of individual $CsPbBr_3$ nanocubes. While TAS provided an indirect method to extract the absorption cross-section of an ensemble of nanocrystals in dispersion, the approach presented here aims to directly investigate single nanocubes or small nanocube clusters, using CEES. In collaboration with Ines Amersdorffer, a PhD student in the research group of Prof. Dr. David Hunger at the KIT in Karlsruhe and Qlibri GmbH, the developers of the CEES setup located in Munich, CEES measurements were performed to obtain the absorption cross-section from spatially isolated nanocube clusters. All CEES measurements presented in the following were carried out by Ines Amersdorffer, while the sample preparation, the AFM, and the PL measurements were performed by myself. As explained in Section 3.7, to perform CEES measurements, the nanocubes must be prepared on a highly reflective mirror substrate. Here, a distributed bragg reflector (DBR) mirror with a reflectivity of $\geq 99.9\%$ for the wavelength range between 450 nm and 550 nm was used. The sample was characterized using SEM and AFM to determine the size of the nanocubes.

5.1.1 Thin Film Preparation

The goal of the film preparation was to create a sample containing either single nanocubes or well-separated nanocube clusters, such that the optical signal from each could be resolved individually within the CEES setup. The $CsPbBr_3$ nanocubes used for these measurements were synthesized via the hot-injection method described in Subsection 3.1.1. Typically, in single-crystal PL spectroscopy, nanocrystal dispersions are highly diluted and spin-coated, often with the addition of a polymer.[102,136] This not only improves the film's uniformity but also significantly enhances the stability of individual nanocrystals by forming a protective barrier against oxygen and moisture. However, the use of polymer leads to complex challenges in the deduction of absolute absorption values with CEES. Embedding nanocrystals in a polymer matrix results in a random separation between the nanocrystals and the DBR mirror surface. Since the CEES signal strongly depends on the nanocube's vertical position within the cavity, such inhomogeneity would complicate the measurement. Simple dilution of the nanocube dispersion with the corresponding solvent, followed by spin coating, also proved insufficient. Dilution leads to a homogeneous reduction in concentration, which results in a uniform but unpredictable spatial distribution of nanocubes across the substrate. Given that the spatial resolution in CEES is limited, it becomes challenging to determine the precise number of nanocubes within the fiber's detection region. To overcome this, a method was developed that does not rely on dilution alone (Figure 5.1). First, the undiluted or weakly diluted nanocube dispersion was spin-coated onto the DBR mirror via a static two-step spin coating process (40 µL, first step: 300 apm, 800 rpm for 20 s, followed by a second step with 1000 apm, 4000 rpm for 30 s) forming a homogeneous nanocube layer. Then, a cotton swab soaked in the same solvent as the dispersion (e.g., hexane or toluene) was used to gently wipe across one half of the substrate surface. This approach consistently yielded three distinct regions on the substrate: a region with a homogeneous thin film with continuous coverage, a transition region, and a region with spatially isolated nanocube clusters. The exact size and spacing of the nanocube clusters in the low-density region vary from sample to sample. This variability originates from both the addition of solvent during the wiping step, which partially redisperses and redistributes nanocubes, and from the mechanical action of the swab, which removes material. Although the spacing and sizes of the nanocube clusters in the low-density region have a certain degree of randomness, it proved to be a simple and reproducible method for creating well separated nanocube clusters suitable for CEES measurements.

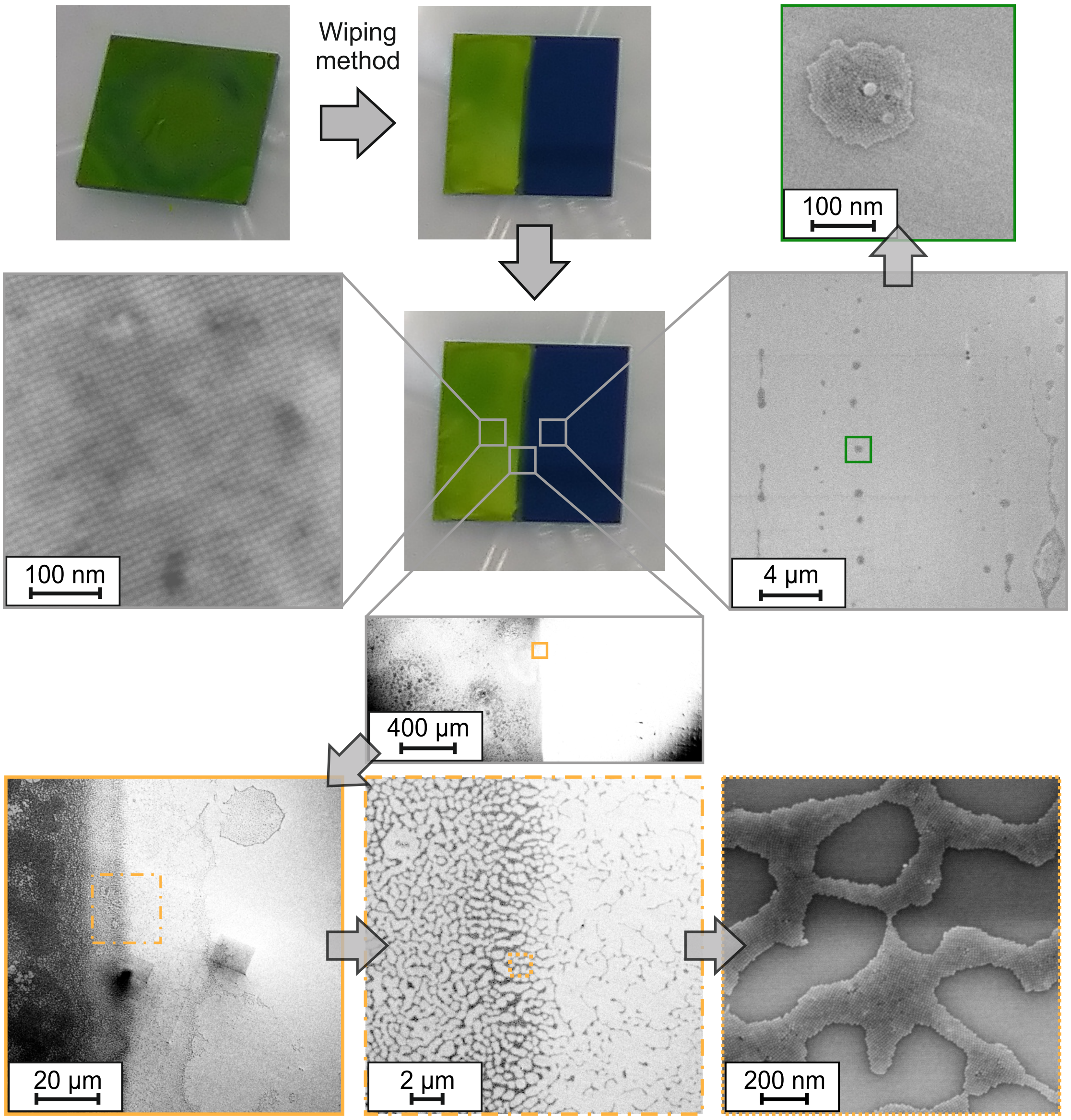

Figure 5.1: Results of the Wiping Method. Photographs of the substrate before and after wiping and SEM images of the three regions on a wiped substrate illustrate the results of the process. SEM images confirm three characteristic regions: A homogeneous thin-film region with continuous nanocrystal coverage (left), a transition region (bottom center), and a region containing spatially isolated nanocrystal clusters (right).

5.1.2 SEM–AFM Correlation

To analyze the number of nanocubes within a cluster, it was necessary to establish a quantification method that could be applied reliably to the prepared thin films. The initial idea was to count the nanocubes per cluster in SEM images. However, SEM imaging proved impractical on DBR mirror substrates due to their poor conductivity, even when coated with a conductive gold-palladium layer. As an alternative, AFM was employed, but it also came with a few limitations. The oily ligand shell

(OA-OLA) surrounding the perovskite nanocubes led to fast contamination of the AFM tip, which in turn reduced spatial resolution. This made it challenging to resolve isolated nanocubes and quantify their number in larger clusters (see Figure 5.2 a for a nanocube cluster with the height of one nanocube). A solution to this problem is to estimate the number of nanocubes within a cluster by determining its lateral area and dividing it by the effective area of a single nanocube including its ligand shell. This approach is only valid under the assumption that the nanocubes exhibit a narrow size distribution and are uniform in shape. Figure 5.2 b shows the normalized height profile of the cluster mentioned above. The smeared cluster edges made it difficult to precisely define the lateral boundaries of the cluster. The apparent cluster diameter varies strongly depending on which fraction of the maximum cluster height is used as its boundary (examples for 70%, 80%, and 90% are indicated by d_{70}, d_{80}, and d_{90}). This uncertainty in defining the diameter shows the need for a consistent definition when evaluating the number of nanocubes via AFM imaging.

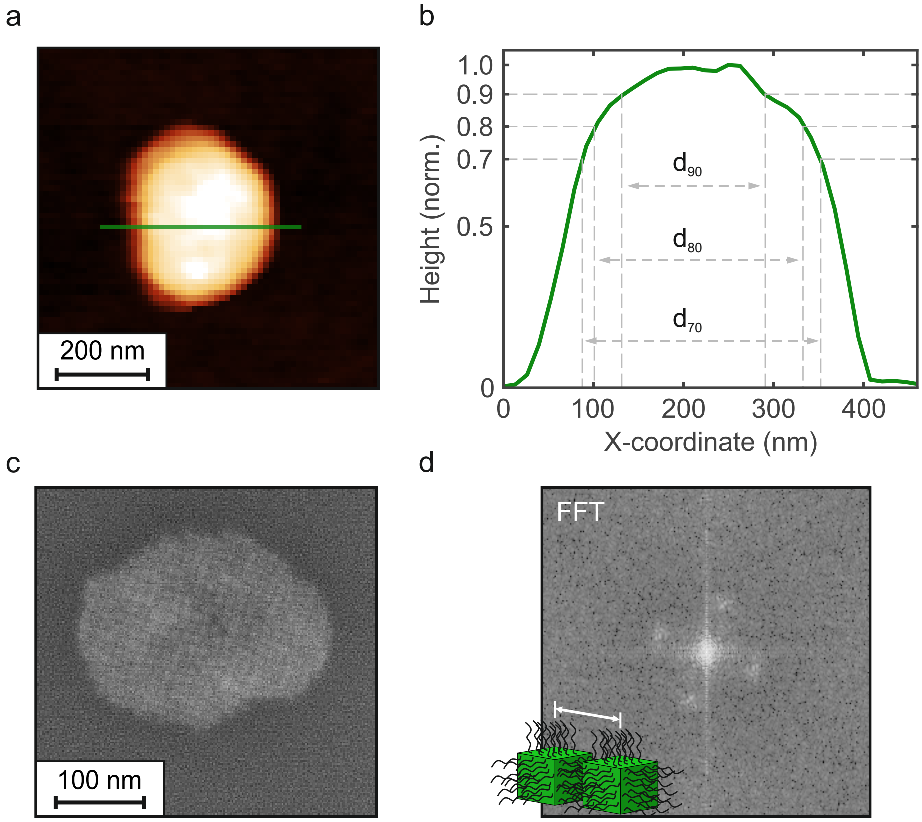

Figure 5.2: Imaging of Nanocube Clusters. **a)** AFM image of a representative nanocube cluster illustrating the rounded appearance of the cluster edges due to tip contamination. **b)** Normalized AFM height profile along the marked direction in (a). Vertical lines indicate how the apparent cluster diameter (d_{70}, d_{80}, and d_{90}) changes depending on the fraction ($70 - 90\%$ of the maximum cluster height). **c)** SEM image of a nanocube cluster with countable individual nanocubes. **d)** Fast Fourier transform of the SEM image in (c). Four distinct reflexes indicate a periodic arrangement of nanocubes along two orthogonal directions. The distance of these reflexes to the center leads to the physical distance between the centers of two nanocubes, as indicated in the schematic in the lower left corner.

A correlation technique between SEM and AFM imaging was developed to overcome this issue. For this purpose, a silicon substrate with a marker grid was prepared using the same spin coating parameters as for the DBR mirror. SEM imaging of this substrate enabled clear resolution of individual nanocubes within clusters, allowing both counting and dimensional analysis (see Figure 5.2 c, d). For the specific sample used here, the average nanocube size was determined to be 8.7 ± 1.0 nm, while the center-to-center distance, which includes the ligand shell, was 12.3 ± 0.5 nm. The nanocube size was obtained by direct measurements from SEM images, and the center-to-center distance was extracted from a fast Fourier transform analysis of the cluster.

To correlate SEM and AFM data, identical regions on the marker silicon substrate were imaged using both techniques (see Figure 5.3 a, b). SEM images provided the true number of nanocubes per cluster, while AFM images yielded the corresponding cluster height and lateral dimensions. As explained above, nanocube clusters appear rounded in AFM, with no clear lateral boundary. Therefore, the extracted diameter of a cluster depends strongly on the height fraction chosen to define it. The correlation diameter is defined as the diameter at which the number of nanocubes counted from SEM images matches the number estimated from the cluster area in AFM measurements. In other words, when plotting the two quantities against each other, the optimal correlation corresponds to a linear relationship with a slope of one. To determine this diameter, various height fractions were tested. For each assumed fraction, the corresponding cluster diameter was extracted, and the number of nanocubes was calculated based on the center-to-center distance obtained from the FFT analysis. These AFM-based estimates were then plotted against the number of cubes counted in the SEM image, and a linear fit was applied. The height fraction that resulted in the best agreement with the identity line was selected as the optimal value. This procedure was carried out for the region shown in Figure 5.3 a, b. The best match was found for a height threshold of 77% (d_{77}), where the AFM-estimated and SEM-counted nanocube numbers align closely. For illustration, the result with additional fits for d_{74} and d_{80} are shown in Figure 5.3 c. Therefore, d_{77} is used as the correlation diameter. It provides a reliable basis for estimating nanocube counts from AFM data.

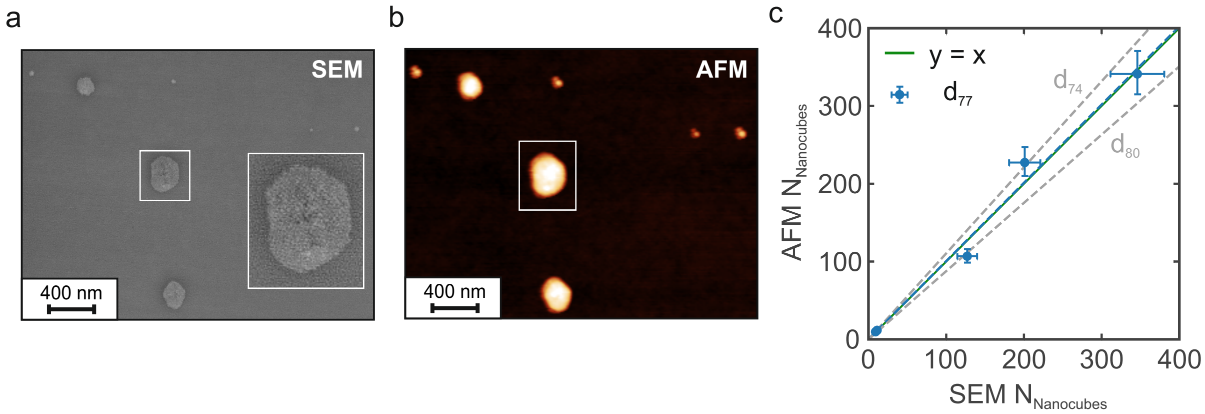

Figure 5.3: Determination of the Nanocube Number. **a)** SEM image of several nanocube clusters, with a zoom-in on the largest cluster in the center. Manual counting revealed that this cluster contains around 346 individual nanocubes. **b)** AFM image of the exact same area as in (a). The previously identified cluster is highlighted with a white rectangle. **c)** SEM-AFM correlation plot comparing the number of nanocubes estimated from AFM height profile data to the number counted in the SEM image. A fraction of 77% (d_{77}) results in the optimal correlation between the counted number of nanocubes.

With this calibration, the number of nanocubes in a cluster can be estimated solely from AFM images. This removes the need for SEM imaging of the mirror and enables nanocube estimation on DBR mirror substrates, provided a calibration has been performed on a representative sample. The following absorption measurements are based on this SEM–AFM correlation strategy, enabling reliable estimation of nanocube counts from AFM cluster profiles.

5.2 Absorption Cross-Section of Perovskite Nanocubes

The previous section demonstrated how SEM–AFM correlation can be used to estimate the number of nanocubes in a cluster using only AFM data. In the following, this capability is exploited to link information on cluster size and respective nanocube number from AFM imaging with extinction measurements and the absorption cross-section obtained via CEES. Similar to the marker silicon substrates, using marker DBR mirrors ensures that the same regions analyzed with AFM can also be relocated and investigated using CEES. In this case, AFM provides spatially resolved height maps of nanocube clusters, while CEES yields a hyperspectral extinction map of the respective area. Since these extinction maps comprise both scattering and absorption, the scattering component has to be subtracted to isolate the absorption. Furthermore, the analysis is only applied to clusters spatially well-separated from other clusters or the marker, to guarantee a clear correspondence between optical and structural data. Each cluster was first characterized via AFM to determine its size, and then measured by CEES to obtain its optical extinction spectrum. The hyperspectral extinction maps generated by CEES correspond to extinction maps, each with a selected wavelength. This is because an area on the substrate is raster-scanned at one selected wavelength at a time. By tuning the laser wavelength across its spectral range, a series of extinction maps can be constructed, thereby providing a wavelength-dependent extinction spectrum of any given point in the map.

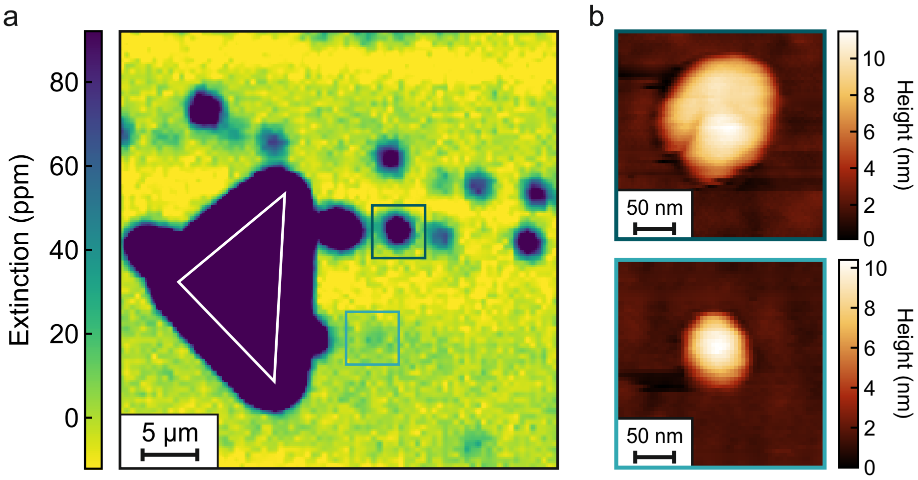

Figure 5.4: Extinction Map and CEES-AFM Correlation. **a)** Extinction map of a region that was also characterized by AFM. A triangular marker clearly illustrates the spatial resolution achievable with the CEES setup. **b)** Corresponding AFM images of the marked spots in (a). These spots exhibit varying extinction levels, which correlate with nanocube clusters of different sizes.

Figure 5.4 a shows such an extinction map at 480 nm for an area featuring the triangle-shaped marker structure and perovskite nanocube clusters. The chromium marker strongly scatters light, thus showing a strong extinction in the measurement. The actual dimensions of the triangle marker are indicated by the white triangle in the figure. This gives an estimate of the spatial resolution of the CEES setup. Figure 5.4 b presents two AFM images of the indicated spots on the extinction map, each containing a nanocube cluster. This illustrates that it was indeed possible to reliably relocate the same positions on the mirror substrate in both AFM and CEES measurements. The characteristic rounded edges of the nanocube clusters mentioned before are also visible in the AFM data. This process was repeated at various positions on the substrate, allowing a total of eight clusters of different sizes to be characterized. Figure 5.5 a presents the resulting wavelength-resolved absorption cross-section,

σ_{abs}, of these nanocube clusters ranging from 3 to 61 nanocubes. The absorption cross-section can directly be calculated from the absorption following Equation 3.14. Figure 5.5 b shows the absorption cross-section at 460 nm plotted against the number of nanocubes per cluster. As expected, larger clusters exhibit higher absorption cross-sections and even show signs of an exciton-like absorption peak. The uncertainty in nanocube count originates from the error on the nanocube size as determined from SEM. If the nanocubes are larger, less of them fit inside a cluster with defined diameter, if they are smaller the opposite is the case.

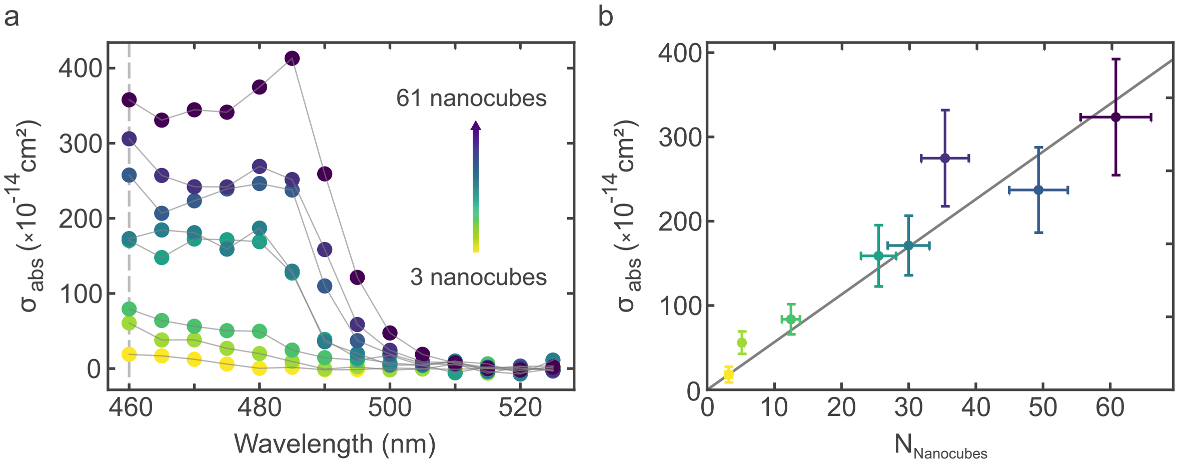

Figure 5.5: Absorption Cross-Section of Nanocube Clusters. a) Wavelength-dependent absorption cross-sections of nanocube clusters containing increasing numbers of nanocubes, derived from CEES measurements after scattering correction. **b)**. Absorption cross-section at 460 nm plotted as a function of the number of nanocubes per cluster. A linear fit (gray line) yields the single-particle absorption cross-section.

In the next step, this data can be used to estimate the absorption cross-section of a single nanocube. The data points are well-described by a linear fit, suggesting a constant absorption cross-section per nanocube. From the slope of this fit, the absorption cross-section of a single $CsPbBr_3$ nanocube is extracted: $\sigma_{\mathrm{abs}} = (5.9 \pm 0.7) \times 10^{-14}\mathrm{cm}^2$. The previous chapter investigated the absorption cross-sections of nanocrystals of varying sizes and shapes. It is, therefore, a natural next step to compare the absorption cross-section extracted here with those earlier results. Since the nanocubes used here have an edge length of 8.7 nm the value of $\sigma_{\mathrm{abs}} = (5.65 \pm 0.40) \times 10^{-14}\mathrm{cm}^2$ determined for nanocubes with an edge length of 8.5 ± 0.6 nm, is used as a comparison (see Table 4.2). Although the earlier cross-sections were determined at a fixed wavelength of 400 nm, making a direct comparison with the CEES-derived value not sensible, verifying that the values lie within the same order of magnitude is still useful. Encouragingly, the value determined here is in the same order of magnitude as the one obtained in the previous chapter, suggesting consistency between the two approaches. This agreement also supports the reliability of the CEES-derived result. To directly compare the CEES-derived absorption cross-section with the methodology based on Poisson statistics, fluence-dependent TAS measurements were performed on the colloidal dispersion of the same sample with an excitation wavelength of 460 nm. Using the same evaluation method as explained in Section 4.3, an absorption cross-section of $\sigma_{\mathrm{abs}} = 4.9 \times 10^{-14}\mathrm{cm}^2$, was extracted, which is in excellent agreement with the CEES data. Ultimately, this represented the first successful attempt to investigate the absorption cross-section of a small number of individual nanocrystals. It demonstrates that the determination of absorption cross-sections for few-nanocube ensembles is very well possible using this method. Furthermore, the results prove to be identical to the results based on a completely different measurement method.

5.3 Absorption Makes Degradation Visible

In addition to enabling the analysis of absorption cross-sections and detailed features in absorption spectra of nanocrystals, CEES also provides a unique opportunity to monitor the degradation of a few or even individual nanocrystals. PL is often the method of choice for probing stability, and numerous studies have employed time-dependent PL intensity series to track the degradation of nanocrystals.[69,91] However, PL only captures radiative recombination from the lowest excited state and thus offers a limited view of the full electronic landscape. It is insensitive to non-radiative states, such as trap states formed during degradation. As more trap states emerge over time, PL intensity typically decreases. While this quenching can be interpreted as a sign of degradation, it does not reveal the nature of the degradation process. Also, once the PL signal vanishes entirely, further insight becomes impossible. CEES, on the other hand, measures absorption and detects all optically allowed transitions, regardless of their properties. Transitions into non-radiative trap states may still contribute weakly to the extinction signal, which makes them accessible, especially at the level of individual or few-nanocrystal measurements. To investigate this, extinction measurements on the same nanocube clusters were performed two and seven days after sample preparation. The corresponding extinction maps are shown in Figure 5.6 a, b. Although this represents only a minimal time series, it already reveals clear changes in the extinction spectrum (see Figure 5.6 c). Moreover, it should be emphasized that, as mentioned earlier, measuring PL from single or very few nanocrystals remains experimentally challenging. In most PL-based studies, degradation is therefore analyzed only at the ensemble level. In contrast, CEES allows us to investigate degradation with spatial resolution down to individual nanocrystals, enabling a much more precise picture of what is happening on the microscopic scale. The overall absorption signal strongly decreases, with the original excitonic feature nearly vanishing. In the higher-energy region, however, an increased signal emerges, suggesting a possible shift of the absorption onset towards the blue. This behavior may indicate that the nanocubes have undergone fragmentation or shrinkage during degradation, leading to stronger quantum confinement and thus a blue-shifted absorption.

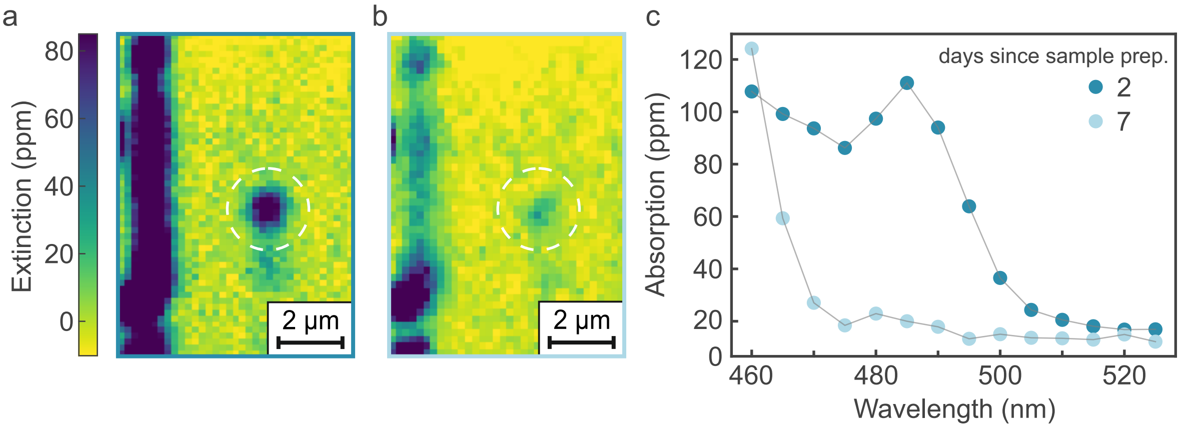

Figure 5.6: Degradation of Nanocube Cluster. a), b) Corresponding extinction maps taken after two and seven days, respectively, highlighting the disappearance of the extinction signal over time due to degradation. **c)** Absorption spectrum of a nanocube cluster measured two and seven days after sample preparation.

The limited spectral range accessible with the current setup and the available time series do not allow for a detailed analysis. Nevertheless, it clearly demonstrates the potential of CEES for monitoring degradation in nanocrystals, especially in cases where the PL intensity is strongly affected by defects. To gain more insight into the nature of these changes, low-temperature CEES measurements would be beneficial, as reduced thermal broadening improves spectral resolution. However, such conditions also suppress degradation due to vacuum and cooling. A promising approach could therefore be to store samples under ambient conditions for defined time intervals and then perform low-temperature measurements to assess degradation post hoc. Given the high sensitivity and spatial resolution of CEES, this method opens the door to more systematic studies of nanocrystal degradation. Realizing this, however, requires extended time-series datasets and carefully controlled environments. While our measurements serve primarily as a proof-of-concept, they lay the groundwork for future work aiming to unravel degradation pathways of single nanocrystals.

5.4 Complete Spectroscopic Investigation of a Nanocube Cluster

After demonstrating absorption cross-section measurements from nanocube clusters down to nearly individual nanocubes and correlating structural and optical properties using both AFM and CEES on the exact same region, this approach was taken a step further by incorporating a third measurement technique: cryogenic PL spectroscopy. This allowed for three distinct methods to be applied to the very same nanocube cluster on a DBR mirror, an achievement that has never been accomplished before (Figure 5.7). The DBR mirror was prepared using the same spin coating parameters and the wiping method. As before, the goal was to investigate the optical properties of a small number of nanocubes. The measurement series began with AFM imaging to locate and characterize nanocube clusters. This was followed by CEES measurements and finally by PL spectroscopy performed at cryogenic temperature. This sequence of methods was chosen because, without using a polymer during thin film preparation to enhance the film's stability, it cannot be assured that the cooling process leaves the sample unaffected. Temperature and long laser exposure may alter the nanocubes during low-temperature PL spectroscopy. As observed above, a sample storage of only seven days leave the sample prone to degradation, making it challenging to achieve a successful result. To prevent degradation as much as possible, the sample was stored in a vacuum for transport and between measurements. PL spectroscopy was performed using the custom-built cryogenic micro-PL setup explained in Section 3.5.

The AFM image in Figure 5.7 a shows nanocube clusters near the edge of the triangle marker, indicated in the lower left corner. The inset in the top right displays a magnified view of the central spot, and the AFM height profile of that nanocube cluster (marked by a blue line) is shown in Figure 5.7 b. The size analysis of this cluster indicates that it consists of 33 nanocubes. An extinction map at 480 nm recorded by CEES at the same location is presented in Figure 5.7 c. Due to the limited spatial resolution, this map covers a larger region, fully revealing the triangular marker. The dashed square indicates the area imaged by AFM and cryogenic PL spectroscopy, while the extinction feature marked by a white circle corresponds to the nanocube cluster of interest. The hyperspectral extinction map was acquired by scanning the excitation wavelength from 470 nm to 525 nm in steps of 5 nm. From these, an absorption spectrum was extracted, as shown for the region of interest in Figure 5.7 d. As already seen in the absorption spectra above, a clear absorption onset around 500 nm is again evident here, although a pronounced excitonic feature is not observed this time. The same sample region is shown again in Figure 5.7 e as a PL image acquired at 4 K. The sample was excited using a pulsed

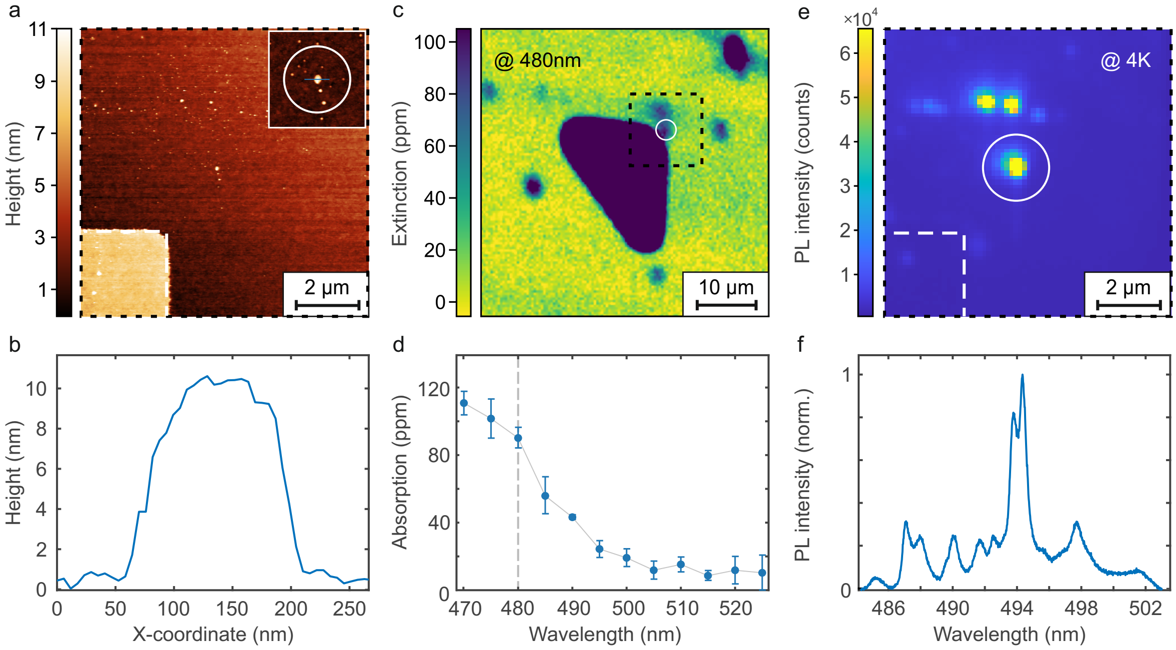

Figure 5.7: Correlated AFM, CEES and PL Measurements of a Nanocube Cluster. a) AFM image of $CsPbBr_3$ nanocubes on a mirror. Part of the triangle-shaped marker can be seen in the bottom left corner. The inset shows a zoom-in to the center of the image. The blue line in the inset shows the direction of the height profile depicted in (b). **b)** Height profile of the circled nanocube cluster. **c)** CEES image of a larger area at 480 nm. The black dashed square indicates the corresponding area in (a) and (e). The white circle corresponds to the white circle in (a) and (e). **d)** Absorption spectrum plotted against the wavelength of the spot marked with the white circle. **e)** PL image at 4 K of the same area as investigated in (a). The white circle marks the same spot as in the AFM image, and the white dashed line indicates the position of the chrome marker. **f)** PL spectrum of the spot marked by the white circle at 4 K.

laser centered at a wavelength of 410 nm. To make the weak PL signal from the nanocube cluster visible, the contrast of the PL image was adjusted. This caused the marker to be nearly invisible, so its location is indicated with a white dashed outline. The bright spots in the PL image can directly be correlated with the clusters identified in the AFM image. The PL spectrum of the central spot marked with a white circle shows several narrow peaks between 487 nm and 498 nm, with FWHMs of only a few nanometers (see Figure 5.7 f). This indicates that the cluster contains nanocubes of slightly different sizes, each emitting at a slightly different wavelength due to the size-dependent quantum confinement effect. The pronounced difference in spectral width and detail compared to the absorption spectrum can largely be explained by temperature effects. As explained in Subsection 2.5.3, homogeneous broadening is strongly suppressed at low temperatures. Therefore, the spectral width is dominated by inhomogeneous broadening, which originates from slight variations in nanocube size. Multiple sharp peaks in the PL spectrum therefore suggest that only a few dozen nanocubes contribute to the emission, further supporting the number determined by the preceding size analysis. One thing to note here is that the spectral region of the PL and the absorption do not align as would be expected for perovskite nanocrystals. As explained in Subsection 2.2.3, the PL of perovskite nanocrystals undergoes a red shift at low temperatures. This implies that these nanocubes would emit at a shorter wavelength when measured at RT. Consequently, the PL spectrum of this cluster does spectrally not align with the detected absorption spectrum. Several mechanisms could explain this discrepancy, with degradation being one of the most plausible causes. In general, nanocrystal degradation can result in either energetic or structural changes. Energetic changes mostly occur through the formation of trap states, resulting in reduced PL intensity. Structural changes of nanocrystals also result in energetic shifts of the band gap. These can manifest as a blue shift due to increased quantum confinement when the nanocrystals fragment or a red shift due to decreased quantum confinement when the nanocrystals coalesce (see Figure 3.6.7). Therefore, it is reasonable to assume that degradation has caused the spectral mismatch among the nanocubes.

5.5 Summary and Discussion

This work showed the first successful attempt at investigating the absorption cross-section of only a few nanocubes using CEES. Although the direct measurement of the absorption cross-section of a single nanocube was not achieved, it was extrapolated by analyzing clusters of increasing nanocube count. To enable these measurements, a sample preparation method was developed where the nanocube thin film was wiped using a solvent-soaked cotton swab. This resulted in isolated nanocube clusters suitable for investigation via CEES. Since DBR mirrors prevent SEM imaging, the correlation between AFM and SEM was established to confidently determine the number of nanocubes per cluster. The resulting absorption cross-section of a single $CsPbBr_3$ nanocube was found to be $\sigma_{abs} = (5.9 \pm 0.7) \times 10^{-14} cm^2$ which agrees remarkably well with previously published data obtained via fluence-dependent TAS, confirming the validity of this new method. In addition, the absorption cross-section was cross-checked using the same method as the previously published data (a Poisson-based statistical approach), again showing strong consistency with the results.

If the values obtained are similar to those from already established methods and this new approach appears more complex, it is reasonable to ask what the benefit is. The most important advantage is that CEES allows spatially and spectrally resolved measurements, making it possible to resolve individual nanocubes. In addition, it comes with the benefit that wavelength-dependent measurements are significantly faster than the traditional TAS methodology, where a fluence series has to be performed for each wavelength of interest. The advantage becomes clear when looking at the hyperspectral extinction maps that can be obtained. These provide wavelength-dependent extinction spectra for each position on the map. If such measurements are combined with low-temperature conditions, as currently being developed by Qlibri GmbH, the technique could reveal information similar to what is accessed through single-crystal PL spectroscopy. One could resolve excitonic fine structure or determine exciton binding energies of individual nanocrystals without relying on high PLQY, which has so far been a fundamental limitation of single-crystal PL spectroscopy. These results mark only the beginning of a highly promising new methodology with broad potential for further development and application. In future studies, this could be extended to other nanocrystals, including different shapes and sizes, as long as nanocrystal stability is considered and DBR mirrors with appropriate spectral coatings are available.

6

Energy Transfer in Stability-Optimized Perovskite Nanocrystals

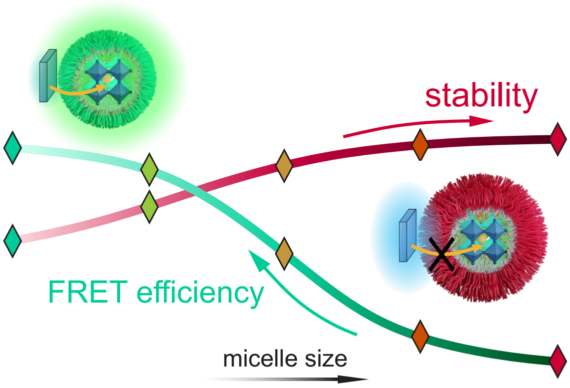

This chapter investigates the energy transfer dynamics between 2D $CsPbBr_3$ nanoplatelets and polymer-encapsulated $MAPbBr_3$ nanocrystals with varying shell thickness. The encapsulation significantly enhances the stability and longevity of the perovskite nanocrystals, which is crucial for their application in optoelectronic devices. However, the additional polymer shell impedes charge transfer, complicating device integration. Thus, FRET is employed as an exciton injection method, allowing excitation while preserving stability. By varying the polymer shell thickness, a trade-off between charge carrier injection and stability is revealed: increasing the thickness of the polymer shell enhances stability but reduces FRET efficiency. FRET efficiencies of up to 73.6% can be reached when using the shortest polymer length, indicating that high efficiency comes at the cost of lower stability. Identifying the optimal balance between these competing factors is critical for realizing tailored energy funnels that enhance carrier densities, ultimately improving the performance of perovskite nanocrystal-based optoelectronic applications. The results and all figures presented in this chapter have been published in ACS Nano Letters in 2022.[137]

6.1 Encapsulated Nanocrystals of Different Shell-Thickness

To investigate energy transfer processes in perovskite nanocrystal systems, both a donor and an acceptor species are required. In this study, 3ML $CsPbBr_3$ nanoplatelets were chosen as donors and $MAPbBr_3$ nanocrystals encapsulated in polymer micelles as acceptors. The unique advantage of this system lies in the ability to systematically vary the polymer shell thickness, providing precise control over the average interparticle distance. This setup allows for a detailed study of how shell thickness influences both the long-term stability and the energy transfer efficiency between nanocrystals.

In the first step, the micelle-encapsulated acceptor nanocrystals were synthesized using the previously reported diblock copolymer nanoreactor synthesis, described in Subsection 3.1.3. There, hybrid organic/inorganic $MAPbBr_3$ perovskite nanocrystals are formed inside diblock copolymers composed of PS and P2VP. Different polymer lengths were used for synthesis, resulting in encapsulated nanocrystals with varying shell thicknesses. In particular, five different polymer compositions with comparable P2VP monomer numbers but PS blocks ranging from 113 to 558 monomers were selected (see Figure 6.1). Accordingly, the polymer and the resulting encapsulated nanocrystals were named based on the PS block length, e.g., PS113. The resulting encapsulated nanocrystals were characterized using TEM and AFM.

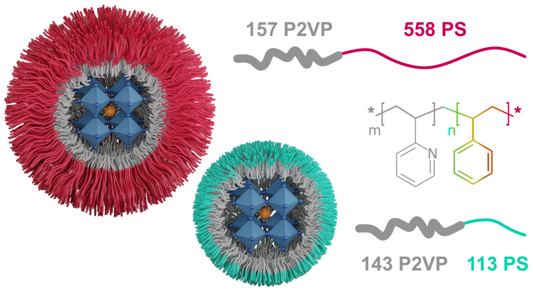

Sample	Polymer ID	#PS units	#P2VP units
PS113	P40763-S2VP	113	143
PS221	P19261-S2VP	221	133
PS327	P8408-S2VP	327	171
PS394	P10492-S2VP	394	143
PS558	P8722-S2VP	558	157

Figure 6.1: Micelle-Encapsulated Nanocrystals and Polymer Information. (Left) Schematic illustration of micelle-encapsulated perovskite nanocrystals with the thickest (PS558) and thinnest (PS113) polymer shells, along with their corresponding diblock copolymer structures. (Right) Overview of the polymers used to synthesize micelles with varying shell thicknesses.

Since the polymer exhibits low contrast in TEM images compared to the lead-containing nanocrystals, it was easily possible to extract the core sizes of the micelles from TEM images. Figure 6.2 illustrates the procedure used for this analysis. A mask was applied to the TEM images, identifying the nearly spherical cores of the encapsulated nanocrystals based on contrast differences (see Figure 6.2 a). From this mask, an average core radius was determined and plotted as a function of the P2VP block length in Figure 6.2 b. For the three shortest polymers (PS113-PS327), a linear correlation was observed between the P2VP monomer number and the core size, with core sizes ranging from 8.7 ± 1.9 nm to 12.4 ± 3.2 nm. However, the two longest polymers (PS394 and PS558) exhibited smaller core radii of 6.9 ± 1.9 nm and 7.5 ± 1.5 nm, respectively. This is attributed to two factors. Firstly, the longer polymer chains form larger shells, which hinder precursor salt diffusion into the micelle cores, slowing nanocrystal formation. Secondly, the longer polymer chains compress the micelle core, restricting nanocrystal growth. To estimate shell thickness, AFM images of dip-coated films of the encapsulated nanocrystals were analyzed. These images revealed highly monodisperse nanocrystal monolayers (Figure 6.2 c). An FFT of the AFM images resulted in the core-to-core separation distances for each polymer type.

From that core-to-core distance, the micelle radius is calculated, which is then combined with the previously determined core sizes to estimate the polymer shell thickness. The shell thickness ranged from 3.7 ± 1.8 nm (PS113) to 9.5 ± 2.2 nm (PS394). A schematic representation of the encapsulated nanocrystals is provided in Figure 6.2 e.

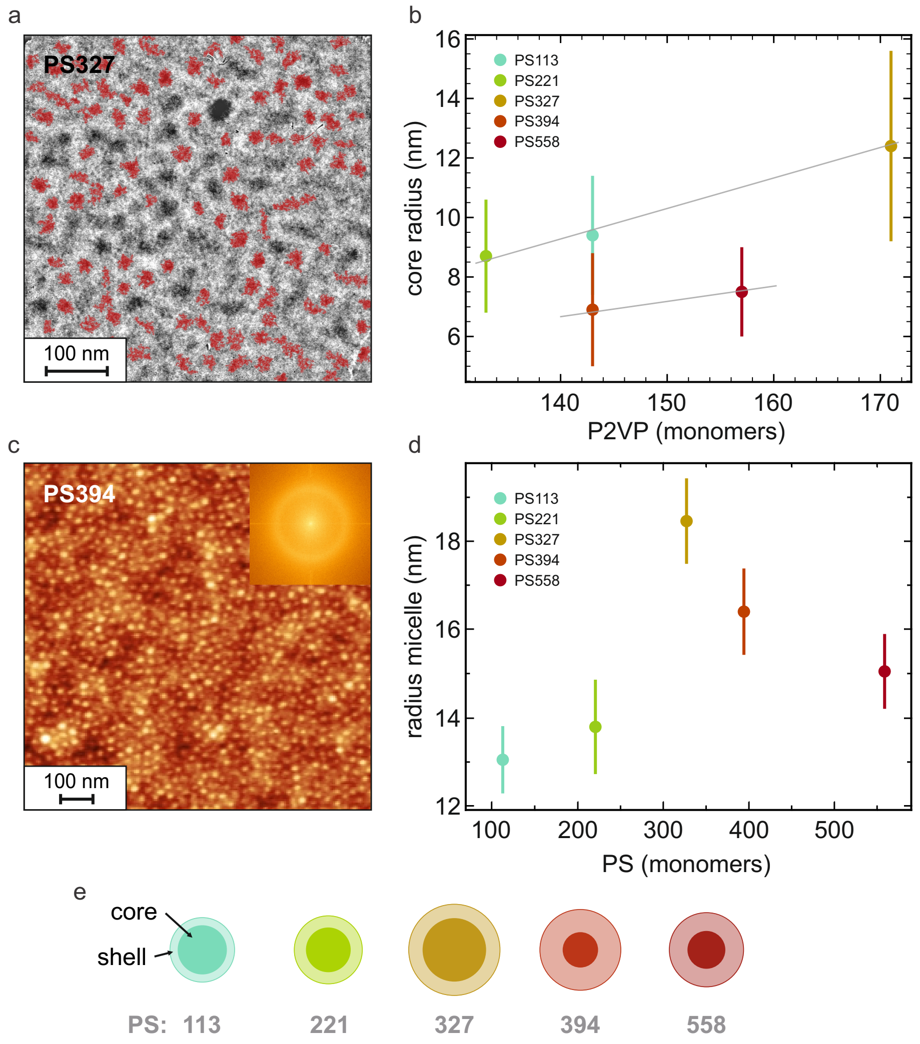

Figure 6.2: Structural Characterization of Micelle-Encapsulated Nanocrystals. a) TEM image of drop-casted micelle-encapsulated nanocrystals (PS327) with applied mask (red) used for core size analysis. **b)** Calculated average core radius of all five micelle samples with the variance indicated as the error. The gray lines constitute guides to the eye, showing a consistent trend with the number of P2VP monomers. **c)** AFM image of a drop-casted PS394 micelle film, showing spontaneous hexagonal self-assembly. The inset shows the FFT. **d)** Average micelle radius plotted as a function of PS block length for all five block copolymers. **e)** Schematic representation of the five micelle systems, illustrating relative core sizes and shell thicknesses.

Notably, the encapsulated nanocrystals exhibited minimal UV/VIS and PL spectra variations (see Figure 6.3), regardless of the polymer composition used. The PL emission maxima were between 524 nm and 525 nm for the first three micelle species and show narrow FWHM values of approximately 22 ± 1 nm (100 ± 3 meV). The last two micelle species (PS394 and PS558) exhibited slightly blue-shifted PL emission maxima at 523.4 nm and 520.3 nm, respectively. This blue shift is attributed to weak quantum confinement effects arising from restricted precursor salt diffusion and limited space in the compressed micelle cores.[138] Multiple individual crystallization centers could lead to the formation of smaller, separated nanocrystals, contributing to the overall blue shift in PL emission.

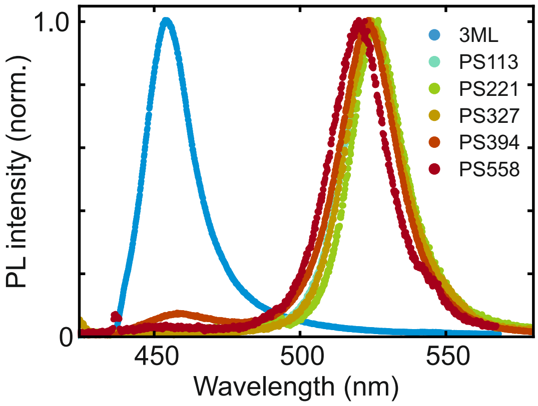

Sample	Peak position (nm)	FWHM (nm)
3ML	454.7	19.25
PS113	524.5	22.34
PS221	525.4	21.30
PS327	524.7	21.89
PS394	523.4	22.92
PS558	520.3	22.46

Figure 6.3: PL Characteristics of 3ML Nanoplatelets and Micelle-Encapsulated Nanocrystals. (Left) Normalized PL spectra of a thin film drop-casted on a silicon substrate comprising 3ML nanoplatelets (light blue) and micelle-encapsulated nanocrystals with different shell thicknesses (turquoise to red – increasing number of PS monomers). (Right) PL peak positions and FWHM for all investigated samples. Values were extracted from a Gaussian fit to the PL spectra.

6.2 Long-Term Stability of Encapsulated Nanocrystals

The primary motivation for employing polymer encapsulation was to enhance the stability of perovskite nanocrystals by shielding them from water and preventing halide ion exchange.[69] To investigate the protective abilities of micelles with different shell thicknesses, stability tests were conducted by drop casting nanocrystal dispersions (50 µL) onto 20 × 20 mm silicon dioxide glass substrates and storing them under ambient conditions (approximately 40% relative humidity, 20 °C and nearly no light) in the laboratory. Over 118 days, periodic PL measurements revealed that the PL peak position remained nearly unchanged, indicating that the crystalline structure of the encapsulated nanocrystals stayed intact (see Figure 6.4 a). However, a gradual decrease in PL intensity was observed, which can be attributed to increased non-radiative recombination of excitons, probably originating from trap states forming due to the degradation. To quantitatively compare the stability of encapsulated nanocrystals with different micelle shell thicknesses, the PL intensity was integrated over the wavelength range and normalized to its initial value on day zero. The resulting decay curves were fitted with a monoexponential function to extract a stability lifetime, τ_{stab}, defined as the time required for the integrated PL intensity to decrease to 1/e of its original value (see Figure 6.4 b). Plotting these values against the shell thickness revealed a clear trend. The polymer with the thinnest shell showed a stability lifetime of 17.6 days, which increased with shell thickness until reaching 27.5 days for the thickest polymer shell (Figure 6.4 c). Interestingly, the stability lifetime appears to saturate beyond a shell thickness of 8 nm. This saturation suggests that beyond a certain thickness, the polymer shell effectively shields the nanocrystals from environmental influences. Further increasing the shell thickness does not significantly improve stability but, as discussed above, can still be exploited to tune the size of the encapsulated nanocrystals.

Compared to a previous study on the stability of encapsulated nanocrystals, which reported that the PL intensity of PS266 micelles remained constant over more than 200 days and even persisted for 75 days days when submerged in water, the time span measured in this work appears to be quite short.[69] This discrepancy can largely be attributed to differences in film thickness, which in turn depend on the amount of nanocrystal dispersion used during drop casting. To underline that film thickness plays a significant role in stability, new PS113 and PS558 thin films were prepared using again 50 µL and,

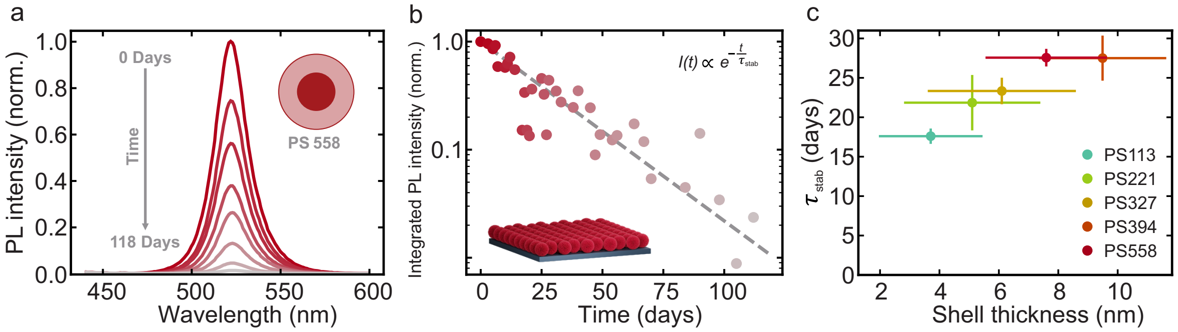

Figure 6.4: Stability of Micelle-Encapsulated Nanocrystals. a) PL spectra of a drop-casted PS558 micelle film acquired over 118 days. While the overall intensity decreases, the peak position stays constant, indicating no change in the nanocrystals inside the micelle. **b)** Integrated PL intensity of the spectra shown in a) as a function of time. As indicated, the data is fitted with a monoexponential function (gray dashed line). For comparison of the different systems, a stability lifetime, τ_{stab}, is extracted from the fit. **c)** Stability lifetime values for each of the five investigated encapsulated nanocrystal samples. The thicker the micelle shell, the higher the stability.

in addition, 200 µL as the drop cast volumes. Increasing the drop-cast volume fourfold resulted in thicker films, comparable to those in the previous study. Their PL intensity was then monitored over a period of 100 days. In stark contrast to the thinner films, no PL intensity loss was measured for the higher-volume samples, and in the case of PS558, the PL intensity even increased over time (see Figure 6.5). This increase can be explained by nanocrystal aggregation within the micelles, which may lead to the repair of surface trap states, a process that is feasible due to the absence of organic ligands typically present in conventional nanocrystals. These findings highlight that not only the individual micelle shell thickness but also the overall film thickness plays a crucial role in stabilizing nanocrystals, as each encapsulated nanocrystal layer provides additional protection to the layers beneath.

Since halide perovskite nanocrystals used in light-emitting and light-harvesting devices are exposed to both elevated temperatures and high-energy radiation, the stability of these encapsulated nanocrystals was further tested under continuous UV light illumination ($\lambda = 365$ nm) and at 60 °C to simulate real-world conditions. To further evaluate the impact of film thickness and polymer shell thickness, both 50 µL and 200 µL films comprising the shortest and longest polymer samples (PS113 and PS558) were tested.

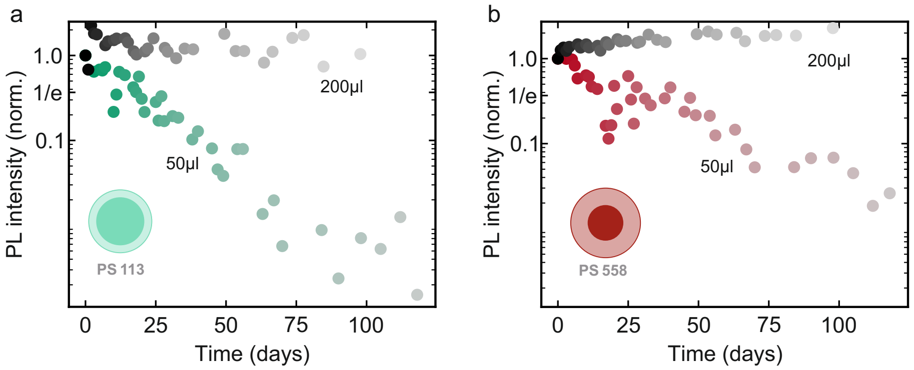

Figure 6.5: Film Thickness-Dependent Stability. Integrated PL intensity of micelle thin films over time for two different drop cast volumes: 50 µL (colored) and 200 µL (black). **a)** PS113 micelles. **b)** PS558 micelles. The film thickness greatly impacts the overall sample stability, as the PL intensity does not degrade over 100 days for thicker films.

For the stability measurements at elevated temperatures, drop-casted thin films were placed on a heat plate at 60 °C. The samples had to be removed from the heat plate for PL intensity measurements. For the first four measurements, the period between subsequent measurements was 10 min, which was successively prolonged up to 180 min. The total time on the heat plate was 910 min. Figure 6.6 a, b clearly shows that the integrated PL intensity decreases significantly faster for thinner films (50 µL) than for thicker ones (200 µL). Although the effect is less pronounced, the results indicate that the polymer shell thickness influences thermal stability. Specifically, PS113 exhibits a faster decline in PL intensity than PS558, suggesting that a thicker polymer shell provides better protection against heat-induced degradation. This behavior suggests that oxygen and moisture influence the degradation mechanism. Notably, the PL peak position remained unchanged over time (see Figure 6.6 c), indicating that the nanocrystals do not undergo significant changes in size. This suggests that the crystal structure is preserved and that the observed degradation is not structural but instead linked to the formation of trap states, which promote nonradiative recombination and cause the gradual loss of PL intensity. The PL measurements under continuous UV illumination were carried out by exposing four drop-casted thin films to 365 nm emission. Initially, a PL spectrum was recorded every five minutes, with the total duration increasing incrementally to 180 min. After an overnight exposure of 985 min, the last spectrum was taken 2000 min after the start. The results of the integrated PL intensity are depicted in Figure 6.6 d,e. In contrast to the high-temperature measurement series, no dependence on film thickness is observable, nor does the shell thickness influence the stability. However, the PL peak position reveals a blue shift for all samples (see Figure 6.6 f). This indicates a structural change of the nanocrystals within the micelles and suggests a degradation mechanism distinct from an oxygen- and moisture-driven process. Since UV radiation can penetrate the polymer shell without constraint, it is evident that neither the shell thickness nor the film thickness increases the stability against UV irradiation. The initial increase in PL intensity likely results from a photo-repair effect, in which shallow trap states are temporarily passivated. With continued UV exposure, this effect fades as the photoinduced desorption of surface ligands starts to dominate and the $MAPbBr_3$ nanocrystals begin to decompose.

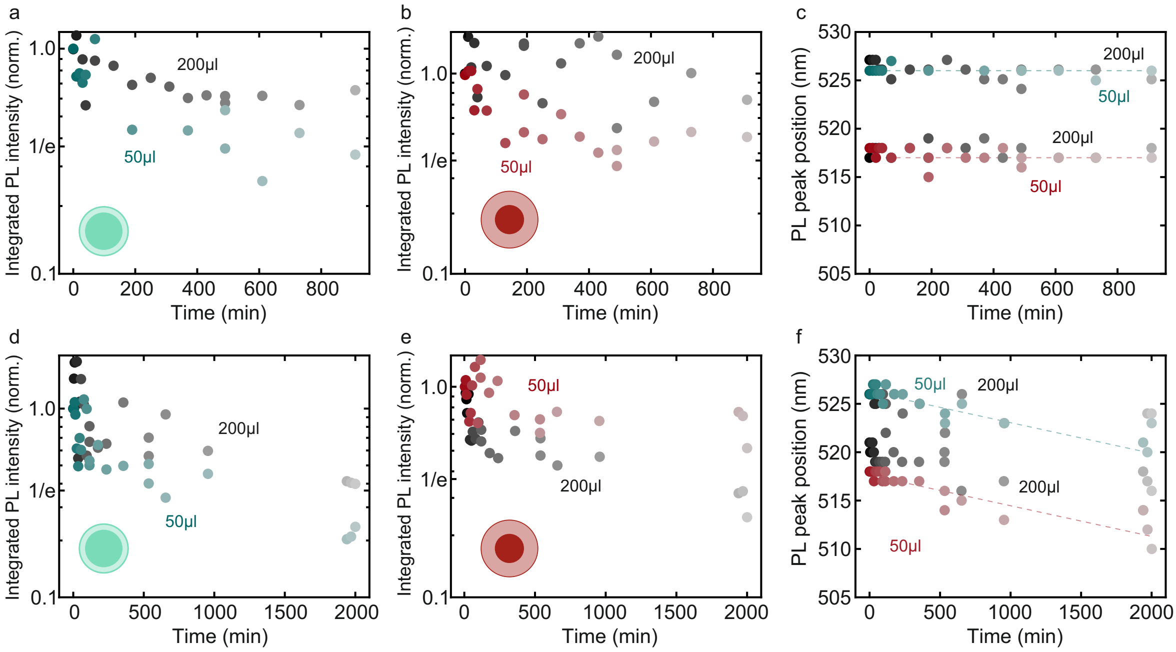

Figure 6.6: Temperature and UV Stability. Integrated PL intensity and PL peak position over time of micelle thin films for different amounts of drop cast volumes: 50 µL (colored) and 200 µL (black). At 60 °C (**a-c**) and under continuous illumination with UV light (λ = 365 nm) (**d-f**).

6.3 Energy Transfer Dynamics of Encapsulated Nanocrystals

Although the stability of encapsulated nanocrystals is significantly increased, this encapsulation comes with a downside. The polymer shell inhibits charge carrier injection due to its insulating nature. To circumvent this limitation, FRET can be employed as an alternative mechanism for injecting charge carriers, ultimately allowing the encapsulated nanocrystals to be used in optoelectronic devices. As explained in Subsection 2.6.1, FRET is a non-radiative energy transfer process that requires two participants, namely a donor and an acceptor. To ensure efficient FRET, three factors must be considered: First, a sufficient spectral overlap between the donor emission and acceptor absorption enables the energy transfer in the first place. Second, a short interparticle distance increases the transfer efficiency. And third, the relative orientation of the transition dipole moments plays a role that should not be neglected. These aspects are collectively described by the so-called Förster radius, which defines the donor–acceptor separation at which the FRET efficiency reaches 50%. Since the insulating polymer shell has to be bypassed, micelle-encapsulated nanocrystals were designated as the acceptor. As the donor, 3ML $CsPbBr_3$ nanoplatelets were selected due to their spectral overlap with the acceptor's absorption and the well-separated PL peak, allowing for optimal filter-based peak separation. This choice also eliminates potential halide ion exchange between donor and acceptor. The PL and absorption spectra of both species are presented in Figure 6.7 a.

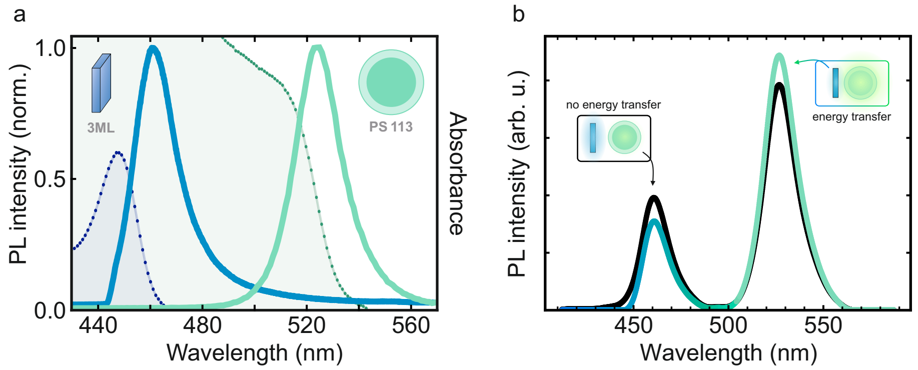

Figure 6.7: Absorption and PL spectra of Donor and Acceptor. a) Absorption (dashed lines) and PL spectra (solid lines) of 3ML nanoplatelets and PS113 micelles. **b)** Experimental PL spectrum of a 3ML nanoplatelet-PS113 micelle thin film (colored line) and a calculated PL spectrum (black curve) obtained through a weighted addition of the two individual PL spectra. The decrease (increase) in PL emission of the donor (acceptor) indicates an energy transfer process between the two nanocrystal species.

To investigate the FRET process, donor-acceptor mixtures were prepared by mixing nanocrystal dispersions in defined ratios and depositing them onto silicon substrates via drop casting. Given that the polymer shell thicknesses are within the typical Förster radius range ($5 - 10$ nm), the donor-acceptor separation can be systematically tuned by adjusting the shell thickness, and its effect on FRET efficiency can be subsequently examined.[34] For this purpose, each micelle type (PS113-PS558) was separately mixed with pure 3ML nanoplatelets. Pure donor and acceptor dispersions were also deposited as thin films to serve as reference samples. Since the exact concentration of nanocrystals in the solution was unknown, the PL intensity of the donor and the acceptor was first adjusted to comparable levels through dilution. Following this calibration, donor-acceptor mixtures were prepared in ratios ranging from 20 : 80 to 99.9 : 0.1 (acceptor:donor - A:D). Compared to the calculated spectra obtained by weighted addition of the reference spectra based on the mixing ratios, the PL spectra of the mixtures exhibited increased acceptor and decreased donor PL intensity. This deviation from the calculated spectra serves as the first indication of energy transfer (see Figure 6.7 b).

Since steady-state PL spectra alone cannot distinguish FRET from reabsorption, where photons emitted by the donor are reabsorbed by the acceptor, artificially enhancing its signal, TRPL measurements were performed to verify the presence of the FRET process. To this end, TCSPC was used to monitor the PL decay of the donor. A reduction in donor PL lifetime in the presence of an acceptor indicates an additional non-radiative decay channel, which would confirm FRET. To separate the donor and acceptor PL, optical long- and shortpass edge filters were used to selectively detect the respective PL decay (see Figure 6.8 a).

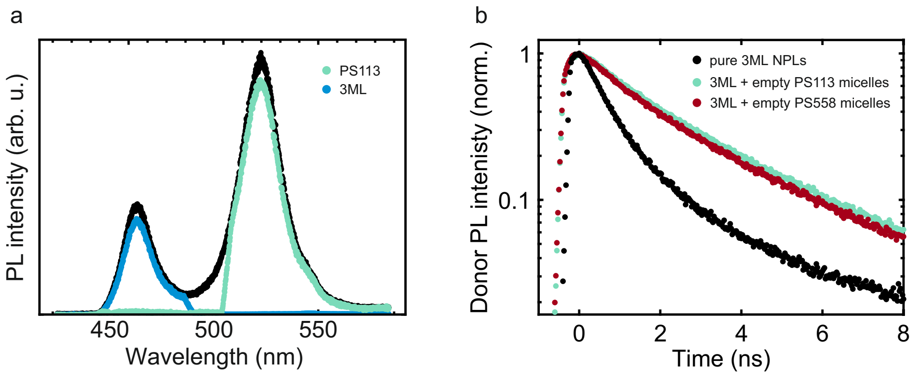

Figure 6.8: Preliminary Tests for Energy Transfer Measurements. a) PL spectrum of a mixture containing 3ML nanoplatelets and PS113 micelles, along with individual PL spectra obtained by selectively filtering out the emission of one ore the other component using optical filters. **b)** TRPL decay of 3ML nanoplatelets mixed with empty micelles (PS113 and PS558), confirming the absence of energy transfer in these control samples.

Before measuring the donor PL decay in the mixture, it is essential to evaluate the influence of the diblock copolymer on the pure donor. In dispersion, 3ML nanoplatelets show a PL decay with a lifetime of 0.9 ns, which increases to 2.1–2.3 ns when mixed with empty micelles in toluene, due to the altered dielectric environment. Importantly, this effect is independent of polymer length, as both PS113 and PS558 micelles yield nearly identical donor decay dynamics (see Figure 6.8 b). Therefore, this extended PL lifetime was used as the reference donor PL lifetime for the subsequent FRET analysis. Next, TRPL measurements were performed on both donor and acceptor PL peaks independently. Figure 6.9 shows the results for the 3ML nanoplatelet-PS113 mixture. The donor PL decay becomes progressively faster with increasing acceptor concentration, indicating an additional non-radiative decay pathway consistent with FRET. Complementary measurements of the acceptor PL decay show a corresponding increase in lifetime with higher donor concentrations. The combination of a shortened donor PL lifetime and a prolonged acceptor PL lifetime strongly supports the occurrence of FRET and allows reabsorption effects to be ruled out.

The FRET efficiency η_{FRET} can be used to compare different shell thicknesses quantitatively. As explained in detail in Subsection 2.6.1, it can be calculated from the acceptor-concentration-dependent donor PL lifetime via:

$$\eta_{\mathrm{FRET}} = 1 - \frac{\tau_{\mathrm{DA}}}{\tau_{\mathrm{D}}} \tag{6.1}$$

where τ_{D} is the PL lifetime of the pure donor, and τ_{DA} is the donor PL lifetime in the presence of the acceptor. The calculated FRET efficiencies for various donor-acceptor ratios from the 3ML nanoplatelet-PS113 mixture are presented in Figure 6.10 a. As expected, $\eta_{\mathrm{FRET}} = 0$ in the absence of acceptors.

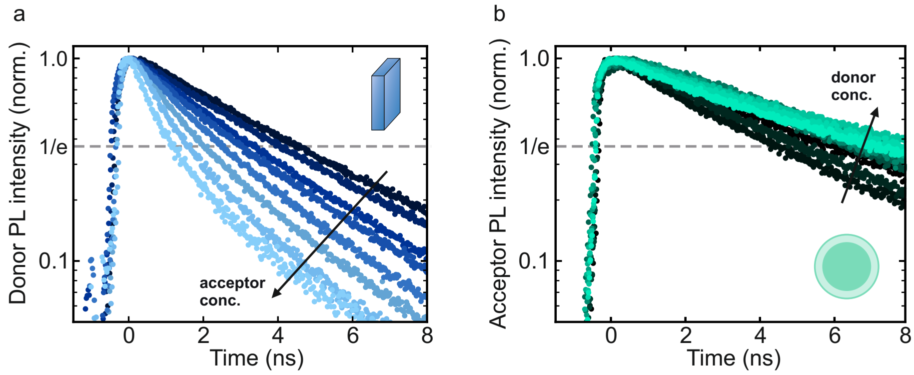

Figure 6.9: PL Decay Curves of Donor and Acceptor in Mixture. a) PL decay curves of a 3ML nanoplatelet film (black) and from mixed films with specific A:D ratios (blue). With an increasing A:D ratio, the donor decay becomes progressively faster. **b)** PL decay curves of a PS113 film (black) and from mixed films with specific A:D ratios (turquoise). With an increasing A:D ratio, the acceptor decay becomes progressively slower.

However, as the acceptor concentration increases, the efficiency rises, reaching a saturation point of approximately 73.6%, indicating that nearly all donor nanoplatelets are surrounded by acceptors and contributing to energy transfer. This efficiency range aligns well with previous reports on CdSe and $CsPbBr_3$ nanoplatelets, confirming the robustness of the observed FRET process.[55,56] This FRET efficiency was determined for all micelle systems and plotted against the micelle radius in Figure 6.10 b. A clear inverse relationship emerges. Thinner polymer shells lead to higher FRET efficiencies. This trend directly contrasts with the observed stability behavior, where thicker shells yielded better protection. Three factors mainly govern the efficiency of FRET. The spectral overlap between donor and acceptor, the orientation of their transition dipoles, and the distance between them. In this case, the spectral overlap remains essentially constant across all samples since the PL peak positions do not shift between different polymer types. The dipole orientation of drop-casted nanocrystals is random and can be considered similar for all systems. This leaves the donor-acceptor distance as the essential variable. As the shell becomes thicker, this distance increases, which in turn reduces the FRET efficiency. This trade-off highlights a central challenge in designing polymer-encapsulated nanocrystal optoelectronics: balancing long-term environmental stability with efficient charge carrier injection.

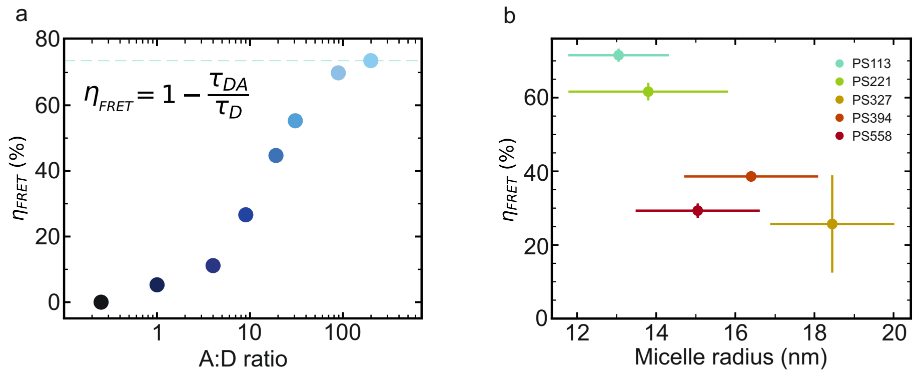

Figure 6.10: FRET Efficiencies. a) Calculated FRET efficiencies of 3ML nanoplatelet-PS113 mixtures as a function of the A:D ratio. **b)** Calculated maximum FRET efficiencies of all five nanoplatelet-encapsulated nanocrystal systems. The FRET efficiency decreases from 73.6% to 25.7% with increasing micelle radius.

6.4 Summary and Discussion

This study investigated $MAPbBr_3$ nanocrystals grown inside PS-*b*-P2VP micelles to explore how the micelle shell thickness affects both long-term stability and energy transfer efficiency. For that, specific PS-*b*-P2VP diblock copolymers were used, enabling systematic control over the polymer shell thickness by varying the length of the PS block. TEM and AFM measurements confirmed that shell thicknesses could be tuned between 3.7 and 9.5 nm while maintaining nearly constant micelle core sizes. Long-term PL stability measurements on encapsulated nanocrystals showed a strong dependence on the shell thickness: thin shells led to fast degradation, whereas increasing the shell thickness improved environmental protection. The measured stability lifetimes ranged from 17.6 days for the thinnest shells up to 27.5 days for the thickest, with a saturation of the stability effect observed for shell thicknesses beyond 8 nm. The thickness of drop-casted thin films also played a crucial role for stability, with thicker films fully preserving PL intensity over 100 days. Stress tests under real-world conditions (60 °C and constant UV illumination) revealed the underlying degradation mechanisms. Heat-induced degradation could be mitigated by thicker shells and films hinting at an oxygen- or moisture-dependent degradation mechanism. In contrast, UV-induced degradation occurred independently of shell or film thickness, suggesting a photoinduced process directly affecting the nanocrystal core. A persistent PL blueshift, indicative of structural changes within the nanocrystals, accompanied this. The energy transfer properties were studied using $CsPbBr_3$ nanoplatelets as donors in FRET experiments. By tuning the shell thickness, the donor-acceptor separation was precisely controlled, and TRPL measurements confirmed efficient FRET with up to 74% efficiency for the thinnest shells. However, transfer efficiency decreased with increasing shell thickness, as expected, due to the increased donor-acceptor distance and a FRET-based transfer mechanism. Ultimately, these findings provide a foundation for tailoring the environmental stability and functional performance of micelle-encapsulated perovskite nanocrystals, enabling their targeted use in optoelectronic and photonic applications.

7

Conclusion and Outlook

Understanding and controlling the interplay between the efficiency, tunability, and stability of nanocrystals is paramount to unlocking their full potential for optoelectronic applications. This thesis addressed these interconnected aspects from multiple experimental perspectives, providing new insights into the fundamental and practical design of lead halide perovskite nanocrystals.

In Chapter 4, the absorption cross-section, exciton trapping, and Auger recombination process in $CsPbBr_3$ nanocrystals with various sizes and shapes were investigated. The absorption cross-section was determined using TAS combined with Poisson statistics. A universal volume-scaling law was revealed, independent of nanocrystal morphology. This finding opens up a practical alternative to structural characterization, as volume can be inferred directly from absorption cross-section measurements. In addition to absorption, the decay of the photobleach signal revealed that the biexciton Auger lifetime also follows a universal volume-scaling law, at least as long as all nanocrystal dimensions are strongly confined. Upon the transition of one dimension into the weak confinement regime, a saturation behavior sets in. These findings indicate that the confined dimension controls the Auger lifetime of biexcitons. Although the origin of this saturation remains to be clarified, exciton delocalization and reduced dielectric screening potentially play a role, suggesting a clear direction for future theoretical work.

Beyond ensemble measurements, Chapter 5 focused on a more direct approach to measuring the absorption cross-section of individual nanocubes using CEES in collaboration with Qlibri GmbH. A newly developed sample preparation method, combined with AFM and SEM correlation, enabled the estimation of the number of nanocubes within individual nanocube clusters via AFM. This allowed, for the first time, the direct extraction of the absorption cross-section of one individual $CsPbBr_3$ nanocube. The technique also proved sensitive for detecting nanocrystal degradation, offering a route toward monitoring stability over time, even in the presence of PL quenching trap states. It was also possible to detect PL at the same position, correlating CEES, PL, and structural analysis on the same spot for the first time. A future CEES setup operating at cryogenic temperatures could be an exciting possibility for accessing the excitonic fine structure of a nanocrystal absorption spectrum that remains hidden at

RT. Such an experiment would arguably approach what many consider the holy grail of single-crystal spectroscopy.

Finally, Chapter 6 took a slight conceptual turn and examined energy transfer between 3ML $CsPbBr_3$ nanoplatelets and polymer-encapsulated $MAPbBr_3$ nanocrystals. The diblock copolymer shell enabled control over inter-particle spacing and environmental stability. Stability in ambient atmosphere increased with thicker polymer shells, though a saturation was observed beyond a shell thickness of 8 nm. Not only was the shell thickness important for improved stability, but the overall film thickness also strongly impacted stability in ambient conditions and at elevated temperatures. Prolonged UV irradiation, however, still posed a challenge, as it penetrated the polymer and directly affected the nanocrystals. On top of that, the insulation layer limits charge injection, and thicker shells also lower the energy transfer efficiency, as expected for a FRET-based mechanism. These results point toward a trade-off between environmental stability and functionality that must be optimized for specific device implementations.

The results highlight how the nanocrystal geometry, particularly its size and shape, significantly influences its functional performance. Nanocrystals designed for light absorption, such as photodetectors or photovoltaics, benefit from large absorption cross-sections. Emissive applications, in contrast, require long biexciton lifetimes to minimize non-radiative decay. Intermediate-sized nanocrystals under moderate confinement and encapsulated with a polymer shell, therefore, offer a promising compromise, combining efficient emission, low trap density, tunable emission, and enhanced stability. Additionally, tailoring the nanocrystal shape could enable control over optical properties such as directional emission. Altogether, the methods and insights developed in this thesis contribute to both a more fundamental understanding and a practical design strategy that meets the demands of a wide range of next-generation optoelectronic applications.

References

[1] R. Rossetti, S. Nakahara, and Louis E. Brus. "Quantum Size Effects in the Redox Potentials, Resonance Raman Spectra, and Electronic Spectra of CdS Crystallites in Aqueous Solution." In: *Journal of Chemical Physics* 79.2 (1983), pp. 1086–1088. DOI: 10.1063/1.445834 (cited on page 1).

[2] Louis E. Brus. "Electron–Electron and Electron-Hole Interactions in Small Semiconductor Crystallites: The Size Dependence of the Lowest Excited Electronic State." In: *Journal of Chemical Physics* 80.9 (1984), pp. 4403–4409. DOI: 10.1063/1.447218 (cited on page 1).

[3] Alexey I. Ekimov, Alexander L. Efros, and Alexei A. Onushchenko. "Quantum Size Effect in Semiconductor Microcrystals." In: *Solid State Communications* 56.11 (1985), pp. 921–924. DOI: 10.1016/S0038-1098(85)80025-9 (cited on page 1).

[4] Christopher B. Murray, David J. Norris, and Moungi G. Bawendi. "Synthesis and Characterization of Nearly Monodisperse CdE (E= Sulfur, Selenium, Tellurium) Semiconductor Nanocrystallites." In: *Journal of the American Chemical Society* 115.19 (1993), pp. 8706–8715. DOI: 10.1021/ja00072a025 (cited on pages 1, 28).

[5] Akihiro Kojima, Kenjiro Teshima, Yasuo Shirai, and Tsutomu Miyasaka. "Organometal Halide Perovskites as Visible-Light Sensitizers for Photovoltaic Cells." In: *Journal of the American Chemical Society* 131.17 (2009), pp. 6050–6051. DOI: 10.1021/ja809598r (cited on page 1).

[6] Martin A. Green, Anita Ho-Baillie, and Henry J. Snaith. "The Emergence of Perovskite Solar Cells." In: *Nature Photonics* 8.7 (2014), pp. 506–514. DOI: 10.1038/nphoton.2014.134 (cited on page 1).

[7] Luciana C. Schmidt, Antonio Pertegás, Soranyel González-Carrero, Olga Malinkiewicz, Said Agouram, Guillermo Mínguez Espallargas, Henk J. Bolink, Raquel E. Galian, and Julia Pérez-Prieto. "Nontemplate Synthesis of $CH_3NH_3PbBr_3$ Perovskite Nanoparticles." In: *Journal of the American Chemical Society* 136.3 (2014), pp. 850–853. DOI: 10.1021/ja4109209 (cited on pages 1, 28).

[8] Loredana Protesescu, Sergii Yakunin, Maryna I Bodnarchuk, Franziska Krieg, Riccarda Caputo, Christopher H Hendon, Ruo Xi Yang, Aron Walsh, and Maksym V. Kovalenko. "Nanocrystals of Cesium Lead Halide Perovskites ($CsPbX_3$, X= Cl, Br, and I): Novel Optoelectronic Materials Showing Bright Emission with Wide Color Gamut." In: *Nano Letters* 15.6 (2015), pp. 3692–3696. DOI: 10.1021/nl5048779 (cited on pages 1, 65).

[9] Javad Shamsi, Alexander S. Urban, Muhammad Imran, Luca De Trizio, and Liberato Manna. "Metal Halide Perovskite Nanocrystals: Synthesis, Post-Synthesis Modifications, and their Optical Properties." In: *Chemical Reviews* 119.5 (2019), pp. 3296–3348. DOI: 10.1021/acs.chemrev.8b00644 (cited on pages 2, 22).

[10] Amrita Dey, Junzhi Ye, Apurba De, Elke Debroye, Seung Kyun Ha, Eva Bladt, Anuraj S. Kshirsagar, Ziyu Wang, Jun Yin, Yue Wang, et al. "State of the Art and Prospects for Halide Perovskite Nanocrystals." In: *ACS Nano* 15.7 (2021), pp. 10775–10981. DOI: 10.1021/acsnano.0c08903 (cited on page 2).

[11] Jingyi Zhu, Yuxuan Li, Xuyang Lin, Yaoyao Han, and Kaifeng Wu. "Coherent Phenomena and Dynamics of Lead Halide Perovskite Nanocrystals for Quantum Information technologies." In: *Nature Materials* 23.8 (2024), pp. 1027–1040. DOI: 10.1038/s41563-024-01922-z (cited on page 2).

[12] Sudipta Seth, Tasnim Ahmed, Apurba De, and Anunay Samanta. "Tackling the Defects, Stability, and Photoluminescence of $CsPbX_3$ Perovskite Nanocrystals." In: *ACS Energy Letters* 4.7 (2019), pp. 1610–1618. DOI: 10.1021/acsenergylett.9b00849 (cited on pages 2, 23).

[13] Shizhe Wang, Amir Abbas Yousefi Amin, Linzhong Wu, Muhan Cao, Qiao Zhang, and Tayebeh Ameri. "Perovskite Nanocrystals: Synthesis, Stability, and Optoelectronic Applications." In: *Small Structures* 2.3 (2021), p. 2000124. DOI: 10.1002/sstr.202000124 (cited on pages 2, 51).

[14] Chuang Yang, Wenjing Hu, Jiale Liu, Chuanzhou Han, Qiaojiao Gao, Anyi Mei, Yinhua Zhou, Fengwan Guo, and Hongwei Han. "Achievements, Challenges, and Future Prospects for Industrialization of Perovskite Solar Cells." In: *Light: Science & Applications* 13.1 (2024), p. 227. DOI: 10.1038/s41377-024-01461-x (cited on page 2).

[15] *National Renewable Energy Laboratory. Best Research-Cell Efficiencies.* https://www.nrel.gov/pv/interactive-cell-efficiency. Accessed: 2025-05-28 (cited on page 2).

[16] Siegfried Hunklinger. *Festkörperphysik*. Berlin, Boston: De Gruyter Oldenbourg, 2018. DOI: 10.1515/9783110567755 (cited on pages 4, 10).

[17] Mantas Simenas, Anna Gagor, Juras Banys, and Miroslaw Maczka. "Phase Transitions and Dynamics in Mixed Three-and Low-Dimensional Lead Halide Perovskites." In: *Chemical Reviews* 124.5 (2024), pp. 2281–2326. DOI: 10.1021/acs.chemrev.3c00532 (cited on page 5).

[18] Charles Kittel. *Introduction to Solid State Physics*. Vol. 8. Wiley New York, 2004. DOI: 10.1119/1.1974177 (cited on page 6).

[19] Claus F. Klingshirn. *Semiconductor Optics*. Springer Science & Business Media, 2012. DOI: 10.1007/978-3-642-28362-8 (cited on page 6).

[20] Laura M. Herz. “Charge-Carrier Dynamics in Organic-Inorganic Metal Halide Perovskites.” In: *Annual Review of Physical Chemistry* 67.1 (2016), pp. 65–89. DOI: 10.1146/annurev-physchem-040215-112222 (cited on pages 8, 13).

[21] Mujtaba Hussain, Muhammad Rashid, Faisal Saeed, and A.S. Bhatti. “Spin–Orbit Coupling Effect on Energy Level Splitting and Band Structure Inversion in $CsPbBr_3$.” In: *Journal of Materials Science* 56.1 (2021), pp. 528–542. DOI: 10.1007/s10853-020-05298-8 (cited on pages 8, 9).

[22] T. Umebayashi, K. Asai, T. Kondo, and A. Nakao. “Electronic Structures of Lead Iodide Based Low-Dimensional Crystals.” In: *Physical Review B* 67.15 (2003), p. 155405. DOI: 10.1103/PhysRevB.67.155405 (cited on page 8).

[23] Federico Brivio, Alison B. Walker, and Aron Walsh. “Structural and Electronic Properties of Hybrid Perovskites for High-Efficiency Thin-Film Photovoltaics from First-Principles.” In: *APL Materials* 1.4 (2013). DOI: 10.1063/1.4824147 (cited on page 8).

[24] Adam D. Wright, Carla Verdi, Rebecca L. Milot, Giles E. Eperon, Miguel A. Pérez-Osorio, Henry J. Snaith, Feliciano Giustino, Michael B. Johnston, and Laura M Herz. “Electron–Phonon Coupling in Hybrid Lead Halide Perovskites.” In: *Nature Communications* 7.1 (2016), p. 11755. DOI: 10.1038/ncomms11755 (cited on pages 9, 14).

[25] Moritz Gramlich, Carola Lampe, Jan Drewniok, and Alexander S. Urban. “How Exciton–Phonon Coupling Impacts Photoluminescence in Halide Perovskite Nanoplatelets.” In: *Journal of Physical Chemistry Letters* 12.46 (2021), pp. 11371–11377. DOI: 10.1021/acs.jpclett.1c03437 (cited on pages 9, 15).

[26] M. Ibrahim Dar, Gwénolé Jacopin, Simone Meloni, Alessandro Mattoni, Neha Arora, Ariadni Boziki, Shaik Mohammed Zakeeruddin, Ursula Rothlisberger, and Michael Grätzel. “Origin of Unusual Bandgap Shift and Dual Emission in Organic-Inorganic Lead Halide Perovskites.” In: *Science Advances* 2.10 (2016), e1601156. DOI: 10.1126/sciadv.1601156 (cited on page 9).

[27] Marina R. Filip, Giles E. Eperon, Henry J. Snaith, and Feliciano Giustino. “Steric Engineering of Metal-Halide Perovskites with Tunable Optical Band Gaps.” In: *Nature Communications* 5.1 (2014), p. 5757. DOI: 10.1038/ncomms6757 (cited on page 9).

[28] Jung-Hoon Lee, Nicholas C. Bristowe, June Ho Lee, Sung-Hoon Lee, Paul D. Bristowe, Anthony K. Cheetham, and Hyun Myung Jang. “Resolving the Physical Origin of Octahedral Tilting in Halide Perovskites.” In: *Chemistry of Materials* 28.12 (2016), pp. 4259–4266. DOI: 10.1021/acs.chemmater.6b00968 (cited on page 9).

[29] Rohit Prasanna, Aryeh Gold-Parker, Tomas Leijtens, Bert Conings, Aslihan Babayigit, Hans-Gerd Boyen, Michael F. Toney, and Michael D. McGehee. “Band Gap Tuning via Lattice Contraction and Octahedral Tilting in Perovskite Materials for Photovoltaics.” In: *Journal of the American Chemical Society* 139.32 (2017), pp. 11117–11124. DOI: 10.1021/jacs.7b04981 (cited on page 9).

[30] Riley E. Brandt, Jeremy R. Poindexter, Prashun Gorai, Rachel C. Kurchin, Robert L.Z. Hoye, Lea Nienhaus, Mark W.B. Wilson, J. Alexander Polizzotti, Raimundas Sereika, Raimundas Zaltauskas, Lana C. Lee, Judith L. MacManus-Driscoll, Moungi Bawendi, Vladan Stevanovic, and Tonio Buonassisi. “Searching for “Defect-Tolerant” Photovoltaic Materials: Combined Theoretical and Experimental Screening.” In: *Chemistry of Materials* 29.11 (2017), pp. 4667–4674. DOI: 10.1021/acs.chemmater.6b05496 (cited on pages 9, 11).

[31] Jacky Even, Laurent Pedesseau, Jean-Marc Jancu, and Claudine Katan. “Importance of Spin–Orbit Coupling in Hybrid Organic/Inorganic Perovskites for Photovoltaic Applications.” In: *Journal of Physical Chemistry Letters* 4.17 (2013), pp. 2999–3005. DOI: 10.1021/jz401532q (cited on page 9).

[32] Jun Kang and Lin-Wang Wang. “High Defect Tolerance in Lead Halide Perovskite $CsPbBr_3$.” In: *Journal of Physical Chemistry Letters* 8.2 (2017), pp. 489–493. DOI: 10.1021/acs.jpclett.6b02800 (cited on page 11).

[33] Quinten A. Akkerman, Gabriele Rainò, Maksym V. Kovalenko, and Liberato Manna. “Genesis, Challenges and Opportunities for Colloidal Lead Halide Perovskite Nanocrystals.” In: *Nature Materials* 17.5 (2018), pp. 394–405. DOI: 10.1038/s41563-018-0018-4 (cited on page 11).

[34] Joseph R. Lakowicz. *Principles of Fluorescence Spectroscopy*. Springer, 2006. DOI: 10.1007/978-0-387-46312-4 (cited on pages 12, 89).

[35] Mark Fox. *Optical Properties of Solids*. Vol. 3. Oxford University Press, 2010 (cited on pages 12, 13, 16).

[36] Lazaro A. Padilha, John T. Stewart, Richard L. Sandberg, Wan Ki Bae, Weon-Kyu Koh, Jeffrey M. Pietryga, and Victor I. Klimov. “Carrier Multiplication in Semiconductor Nanocrystals: Influence of Size, Shape, and Composition.” In: *Accounts of Chemical Research* 46.6 (2013), pp. 1261–1269. DOI: 10.1021/ar300228x (cited on page 13).

[37] Chris de Weerd, Leyre Gomez, Antonio Capretti, Delphine M. Lebrun, Eiichi Matsubara, Junhao Lin, Masaaki Ashida, Frank C.M. Spoor, Laurens D.A. Siebbeles, Arjan J. Houtepen, et al. “Efficient Carrier Multiplication in $CsPbI_3$ Perovskite Nanocrystals.” In: *Nature Communications* 9.1 (2018), p. 4199. DOI: 10.1038/s41467-018-06721-0 (cited on page 13).

[38] Yu Peter and Manuel Cardona. *Fundamentals of Semiconductors: Physics and Materials Properties*. Springer Science & Business Media, 2010. DOI: 10.1007/978-3-642-00710-1 (cited on pages 13–15, 23).

[39] Prakriti Pradhan Joshi, Sebastian F. Maehrlein, and Xiaoyang Zhu. “Dynamic Screening and Slow Cooling of Hot Carriers in Lead Halide Perovskites.” In: *Advanced Materials* 31.47 (2019), p. 1803054. DOI: 10.1002/adma.201803054 (cited on page 14).

[40] Mingjie Li, Jianhui Fu, Qiang Xu, and Tze Chien Sum. “Slow Hot-Carrier Cooling in Halide Perovskites: Prospects for Hot-Carrier Solar Cells.” In: *Advanced Materials* 31.47 (2019), p. 1802486. DOI: 10.1002/adma.201802486 (cited on page 14).

[41] Xianzhong Zhou and Ziyang Zhang. “Electron–Phonon Coupling in $CsPbBr_3$.” In: *AIP Advances* 10.12 (2020). DOI: 10.1063/5.0017149 (cited on page 14).

[42] Christoph Wolf and Tae-Woo Lee. “Exciton and Lattice Dynamics in Low-Temperature Processable $CsPbBr_3$ Thin-Films.” In: *Materials Today energy* 7 (2018), pp. 199–207. DOI: 10.1016/j.mtener.2017.09.010 (cited on page 14).

[43] Claudiu M. Iaru, Annalisa Brodu, Niels J.J. van Hoof, Stan E.T. Ter Huurne, Jonathan Buhot, Federico Montanarella, Sophia Buhbut, Peter C.M. Christianen, Daniël Vanmaekelbergh, Celso de Mello Donega, et al. “Fröhlich Interaction Dominated by a Single Phonon Mode in $CsPbBr_3$.” In: *Nature Communications* 12.1 (2021), p. 5844. DOI: 10.1038/s41467-021-26192-0 (cited on page 15).

[44] Meghnad N. Saha. “On a Physical Theory of Stellar Spectra.” In: *Proceedings of the Royal Society of London. Series A, Containing Papers of a Mathematical and Physical Character* 99.697 (1921), pp. 135–153. DOI: 10.1098/rspa.1921.0029 (cited on page 16).

[45] Valerio D’innocenzo, Giulia Grancini, Marcelo J.P. Alcocer, Ajay Ram Srimath Kandada, Samuel D. Stranks, Michael M. Lee, Guglielmo Lanzani, Henry J. Snaith, and Annamaria Petrozza. “Excitons Versus Free Charges in Organo-Lead Tri-Halide Perovskites.” In: *Nature Communications* 5.1 (2014), p. 3586. DOI: 10.1038/ncomms4586 (cited on page 16).

[46] Andrey L. Rogach. *Semiconductor Nanocrystal Quantum Dots*. Springer, 2008. DOI: 10.1007/978-3-211-75237-1 (cited on page 21).

[47] Bernhard J. Bohn, Yu Tong, Moritz Gramlich, May Ling Lai, Markus Döblinger, Kun Wang, Robert L. Z. Hoye, Peter Müller-Buschbaum, Samuel D. Stranks, Alexander S. Urban, Lakshminarayana Polavarapu, and Jochen Feldmann. “Boosting Tunable Blue Luminescence of Halide Perovskite Nanoplatelets through Postsynthetic Surface Trap Repair.” In: *Nano Letters* 18.8 (2018), pp. 5231–5238. DOI: 10.1021/acs.nanolett.8b02190 (cited on pages 21, 23, 24, 29–31, 64).

[48] Joseph S. Manser, Jeffrey A. Christians, and Prashant V. Kamat. “Intriguing Optoelectronic Properties of Metal Halide Perovskites.” In: *Chemical Reviews* 116.21 (2016), pp. 12956–13008. DOI: 10.1021/acs.chemrev.6b00136 (cited on page 21).

[49] Hao A. Nguyen, Grant Dixon, Florence Y. Dou, Shaun Gallagher, Stephen Gibbs, Dylan M. Ladd, Emanuele Marino, Justin C. Ondry, James P. Shanahan, Eugenia S. Vasileiadou, et al. “Design Rules for Obtaining Narrow Luminescence from Semiconductors Made in Solution.” In: *Chemical Reviews* 123.12 (2023), pp. 7890–7952. DOI: 10.1021/acs.chemrev.3c00097 (cited on page 21).

[50] Jasmina A. Sichert, Yu Tong, Niklas Mutz, Mathias Vollmer, Stefan Fischer, Karolina Z. Milowska, Ramon García Cortadella, Bert Nickel, Carlos Cardenas-Daw, Jacek K. Stolarczyk, Alexander S. Urban, and Jochen Feldmann. “Quantum Size Effect in Organometal Halide Perovskite Nanoplatelets.” In: *Nano Letters* 15.10 (2015), pp. 6521–6527. DOI: 10.1021/acs.nanolett.5b02985 (cited on page 22).

[51] Hua Zhu, Tara Šverko, Juanye Zhang, David B. Berkinsky, Weiwei Sun, Chantalle J. Krajewska, and Moungi G. Bawendi. “One-Dimensional Highly-Confined $CsPbBr_3$ Nanorods with Enhanced Stability: Synthesis and Spectroscopy.” In: *Nano Letters* 22.20 (2022), pp. 8355–8362. DOI: 10.1021/acs.nanolett.2c03458 (cited on page 22).

[52] Dandan Zhang, Yi Yu, Yehonadav Bekenstein, Andrew B. Wong, A. Paul Alivisatos, and Peidong Yang. “Ultrathin Colloidal Cesium Lead Halide Perovskite Nanowires.” In: *Journal of the American Chemical Society* 138.40 (2016), pp. 13155–13158. DOI: 10.1021/jacs.6b08373 (cited on page 22).

[53] Quinten A. Akkerman, Tan P.T. Nguyen, Simon C. Boehme, Federico Montanarella, Dmitry N. Dirin, Philipp Wechsler, Finn Beiglböck, Gabriele Rainò, Rolf Erni, Claudine Katan, et al. “Controlling the Nucleation and Growth Kinetics of Lead Halide Perovskite Quantum Dots.” In: *Science* 377.6613 (2022), pp. 1406–1412. DOI: 10.1126/science.abq3616 (cited on page 22).

[54] Clara Otero-Martínez, Junzhi Ye, Jooyoung Sung, Isabel Pastoriza-Santos, Jorge Pérez-Juste, Zhiguo Xia, Akshay Rao, Robert L.Z. Hoye, and Lakshminarayana Polavarapu. “Colloidal Metal-Halide Perovskite Nanoplatelets: Thickness-Controlled Synthesis, Properties, and Application in Light-Emitting Diodes.” In: *Advanced Materials* 34.10 (2022), p. 2107105. DOI: 10.1002/adma.202107105 (cited on pages 22, 57, 69).

[55] Burak Guzelturk, Murat Olutas, Savas Delikanli, Yusuf Kelestemur, Onur Erdem, and Hilmi Volkan Demir. “Non-radiative Energy Transfer in Colloidal CdSe Nanoplatelet Films.” In: *Nanoscale* 7.6 (2015), pp. 2545–2551. DOI: 10.1039/c4nr06003b (cited on pages 22, 25, 91).

[56] Andreas Singldinger, Moritz Gramlich, Christoph Gruber, Carola Lampe, and Alexander S. Urban. “Nonradiative Energy Transfer between Thickness-Controlled Halide Perovskite Nanoplatelets.” In: *ACS Energy Letters* 5.5 (2020), pp. 1380–1385. DOI: 10.1021/acsenergylett.0c00471 (cited on pages 22, 25, 91).

[57] Jiangtao Hu, Liang-shi Li, Weidong Yang, Liberato Manna, Lin-wang Wang, and A. Paul Alivisatos. "Linearly Polarized Emission from Colloidal Semiconductor Quantum Rods." In: *Science* 292.5524 (2001), pp. 2060–2063. DOI: 10.1126/science.1060810 (cited on page 22).

[58] Chengxi Zhang, Jiayi Chen, Sheng Wang, Lingmei Kong, Simon W. Lewis, Xuyong Yang, Andrey L. Rogach, and Guohua Jia. "Metal Halide Perovskite Nanorods: Shape Matters." In: *Advanced Materials* 32.46 (2020), p. 2002736. DOI: 10.1002/adma.202002736 (cited on page 22).

[59] Qianpeng Zhang, Daquan Zhang, Zebing Liao, Yang Bryan Cao, Mallem Kumar, Swapnadeep Poddar, Junchao Han, Ying Hu, Hualiang Lv, Xiaoliang Mo, et al. "Perovskite Light-Emitting Diodes with Quantum Wires and Nanorods." In: *Advanced Materials* (2024), p. 2405418. DOI: 10.1002/adma.202405418 (cited on page 22).

[60] Changjiu Sun, Yuanzhi Jiang, Li Zhang, Keyu Wei, and Mingjian Yuan. "Toward the Controlled Synthesis of Lead Halide Perovskite Nanocrystals." In: *ACS Nano* 17.18 (2023), pp. 17600–17609. DOI: 10.1021/acsnano.3c05609 (cited on page 22).

[61] Kilian Frank, Nina A. Henke, Carola Lampe, Tizian Lorenzen, Benjamin März, Xiao Sun, Sylvio Haas, Olof Gutowski, Ann-Christin Dippel, Veronika Mayer, et al. "Antisolvent Controls the Shape and Size of Anisotropic Lead Halide Perovskite Nanocrystals." In: *Nature Communications* 15.1 (2024), p. 8952. DOI: 10.1038/s41467-024-53221-5 (cited on pages 22, 30, 57).

[62] Jonathan De Roo, Maria Ibáñez, Pieter Geiregat, Georgian Nedelcu, Willem Walravens, Jorick Maes, Jose C. Martins, Isabel Van Driessche, Maksym V. Kovalenko, and Zeger Hens. "Highly Dynamic Ligand Binding and Light Absorption Coefficient of Cesium Lead Bromide Perovskite Nanocrystals." In: *ACS Nano* 10.2 (2016), pp. 2071–2081. DOI: 10.1021/acsnano.5b06295 (cited on pages 23, 50).

[63] Sara R. Smock, Yunhua Chen, Aaron J. Rossini, and Richard L. Brutchey. "The Surface Chemistry and Structure of Colloidal Lead Halide Perovskite Nanocrystals." In: *Accounts of Chemical Research* 54.3 (2021), pp. 707–718. DOI: 10.1021/acs.accounts.0c00741 (cited on page 23).

[64] Stephanie Ten Brinck, Francesco Zaccaria, and Ivan Infante. "Defects in Lead Halide Perovskite Nanocrystals: Analogies and (Many) Differences with the Bulk." In: *ACS Energy Letters* 4.11 (2019), pp. 2739–2747. DOI: 10.1021/acsenergylett.9b01945 (cited on page 23).

[65] He Huang, Maryna I. Bodnarchuk, Stephen V. Kershaw, Maksym V. Kovalenko, and Andrey L. Rogach. "Lead Halide Perovskite Nanocrystals in the Research Spotlight: Stability and Defect Tolerance." In: *ACS Energy Letters* 2.9 (2017), pp. 2071–2083. DOI: 10.1021/acsenergylett.7b00547 (cited on page 23).

[66] Congyang Zhang, Wanbin Li, and Liang Li. "Metal Halide Perovskite Nanocrystals in Metal–Organic Framework Host: Not Merely Enhanced Stability." In: *Angewandte Chemie* 133.14 (2021), pp. 7564–7577. DOI: 10.1002/anie.202006169 (cited on page 24).

[67] Stepan Demchyshyn, Janina Melanie Roemer, Heiko Groiß, Herwig Heilbrunner, Christoph Ulbricht, Dogukan Apaydin, Anton Böhm, Uta Rütt, Florian Bertram, Günter Hesser, et al. "Confining Metal-Halide Perovskites in Nanoporous Thin Films." In: *Science Advances* 3.8 (2017), e1700738. DOI: 10.1126/sciadv.1700738 (cited on page 24).

[68] Chengxi Zhang, Jiayi Chen, Lingmei Kong, Lin Wang, Sheng Wang, Wei Chen, Rundong Mao, Lyudmila Turyanska, Guohua Jia, and Xuyong Yang. "Core/Shell Metal Halide Perovskite Nanocrystals for Optoelectronic Applications." In: *Advanced Functional Materials* 31.19 (2021), p. 2100438. DOI: 10.1002/adfm.202100438 (cited on page 24).

[69] Verena A. Hintermayr, Carola Lampe, Maximilian Löw, Janina Roemer, Willem Vanderlinden, Moritz Gramlich, Anton X. Böhm, Cornelia Sattler, Bert Nickel, Theobald Lohmüller, and Alexander S. Urban. "Polymer Nanoreactors Shield Perovskite Nanocrystals from Degradation." In: *Nano Letters* 19.8 (2019), pp. 4928–4933. DOI: 10.1021/acs.nanolett.9b00982 (cited on pages 24, 29, 31, 78, 86).

[70] David L. Dexter. "A Theory of Sensitized Luminescence in Solids." In: *Journal of Chemical Physics* 21.5 (1953), pp. 836–850. DOI: 10.1063/1.1699044 (cited on page 25).

[71] Shawn Irgen-Gioro, Muwen Yang, Suyog Padgaonkar, Woo Je Chang, Zhengyi Zhang, Benjamin Nagasing, Yishu Jiang, and Emily A. Weiss. "Charge and Energy Transfer in the Context of Colloidal Nanocrystals." In: *Chemical Physics Reviews* 1.1 (2020). DOI: 10.1063/5.0033263 (cited on page 25).

[72] Theodor Förster. "Zwischenmolekulare Energiewanderung und Fluoreszenz." In: *Annalen der Physik* 437.1-2 (1948), pp. 55–75. DOI: 10.1002/andp.19484370105 (cited on page 25).

[73] Andrey L. Rogach, Thomas A. Klar, John M. Lupton, Andries Meijerink, and Jochen Feldmann. "Energy Transfer with Semiconductor Nanocrystals." In: *Journal of Materials Chemistry* 19.9 (2009), pp. 1208–1221. DOI: 10.1039/B812884G (cited on page 25).

[74] Kenta Furuta, Minoru Fujii, Hiroshi Sugimoto, and Kenji Imakita. "Energy Transfer in Silicon Nanocrystal Solids Made from All-Inorganic Colloidal Silicon Nanocrystals." In: *Journal of Physical Chemistry Letters* 6.14 (2015), pp. 2761–2766. DOI: 10.1021/acs.jpclett.5b01067J (cited on page 25).

[75] Andrey L. Rogach. "Fluorescence Energy Transfer in Hybrid Structures of Semiconductor Nanocrystals." In: *Nano Today* 6.4 (2011), pp. 355–365. DOI: 10.1016/j.nantod.2011.06.001 (cited on page 26).

[76] Abhishek Kumar Soni, Rashmi Joshi, and Raghumani Singh Ningthoujam. “Hot Injection Method for Nanoparticle Synthesis: Basic Concepts, Examples and Applications.” In: *Handbook on Synthesis Strategies for Advanced Materials: Volume-I: Techniques and Fundamentals* (2021), pp. 383–434. DOI: 10.1007/978-981-16-1807-9_13 (cited on page 28).

[77] Hitoshi Kasai, Hari Singh Nalwa, Hidetoshi Oikawa, Shuji Okada, Hiro Matsuda, Nobutsugu Minami, Atsushi Kakuta, Katsumichi Ono, Akio Mukoh, and Hachiro Nakanishi Hachiro Nakanishi. “A Novel Preparation Method of Organic Microcrystals.” In: *Japanese Journal of Applied Physics* 31.8A (1992), p. L1132. DOI: 10.1143/JJAP.31.L1132 (cited on page 29).

[78] George C. Papavassiliou, Georgia Pagona, Nikos Karousis, George A. Mousdis, Ioannis Koutselas, and Anastasia Vassilakopoulou. “Nanocrystalline/Microcrystalline Materials Based on Lead-Halide Units.” In: *Journal of Materials Chemistry* 22.17 (2012), pp. 8271–8280. DOI: 10.1039/C2JM15783G (cited on page 29).

[79] Yu Tong, Eva Bladt, Meltem F. Aygüler, Aurora Manzi, Karolina Z. Milowska, Verena A. Hintermayr, Pablo Docampo, Sara Bals, Alexander S. Urban, Lakshminarayana Polavarapu, and Jochen Feldmann. “Highly Luminescent Cesium Lead Halide Perovskite Nanocrystals with Tunable Composition and Thickness by Ultrasonication.” In: *Angewandte Chemie* 55.44 (2016), pp. 13887–13892. DOI: 10.1002/anie.201605909 (cited on page 29).

[80] Theobald Lohmüller, Daniel Aydin, Marco Schwieder, Christoph Morhard, Ilia Louban, Claudia Pacholski, and Joachim P. Spatz. “Nanopatterning by Block Copolymer Micelle Nanolithography and Bioinspired Applications.” In: *Biointerphases* 6.1 (2011), MR1–MR12. DOI: 10.1116/1.3536839 (cited on page 29).

[81] Maryna I. Bodnarchuk, Simon C. Boehme, Stephanie Ten Brinck, Caterina Bernasconi, Yevhen Shynkarenko, Franziska Krieg, Roland Widmer, Beat Aeschlimann, Detlef Günther, Maksym V. Kovalenko, et al. “Rationalizing and Controlling the Surface Structure and Electronic Passivation of Cesium lead Halide Nanocrystals.” In: *ACS Energy Letters* 4.1 (2018), pp. 63–74. DOI: 10.1021/acsenergylett.8b01669 (cited on pages 29, 51).

[82] Nina Henke, Leo Luber, Ioannis Kouroudis, Jonathan Paul, Alexander Schuhbeck, Lukas Rescher, Tizian Lorenzen, Veronika Mayer, Knut Müller-Caspary, Bert Nickel, Allessio Gagliardi, and Alexander S. Urban. “Synthesizer: Machine Learning-Guided Perovskite Nanocrystal Optimization.” In: (2025). DOI: 10.21203/rs.3.rs-6411699/v1 (cited on pages 30, 57, 69).

[83] Jonathan Mooney and Patanjali Kambhampati. “Get the Basics Right: Jacobian Conversion of Wavelength and Energy Scales for Quantitative Analysis of Emission Spectra.” In: *Journal of Physical Chemistry Letters* 4.19 (2013), pp. 3316–3318. DOI: 10.1021/jz401508t (cited on page 34).

[84] *Harpia User Manual.* Last accessed 05 May 2025. 2024 (cited on pages 38, 46, 49, 51).

[85] *Orpheus-HP User Manual.* Last accessed 28 April 2025. 2024 (cited on pages 38, 40, 41).

[86] *Carbide CB3 User Manual.* Last accessed 12 April 2025. 2024 (cited on page 39).

[87] Patrick Haußmann. “Automation of Cryogenic Spectroscopy of Lead Halide Perovskite Nanocrystal Dispersions.” MA thesis. Ludwig-Maximilians-Universität München, June 2025 (cited on page 43).

[88] Brener R.C. Vale, Etienne Socie, Andrés Burgos-Caminal, Jefferson Bettini, Marco A. Schiavon, and Jacques-E. Moser. “Exciton, Biexciton, and Hot Exciton Dynamics in $CsPbBr_3$ Colloidal Nanoplatelets.” In: *Journal of Physical Chemistry Letters* 11.2 (2019), pp. 387–394. DOI: 10.1021/acs.jpclett.9b03282 (cited on page 49).

[89] Etienne Socie, Brener R.C. Vale, Aaron T. Terpstra, Marco A. Schiavon, and Jacques-E. Moser. “Resonant Band-Edge Emissive States in Strongly Confined $CsPbBr_3$ Perovskite Nanoplatelets.” In: *Journal of Physical Chemistry C* 125.26 (2021), pp. 14317–14325. DOI: 10.1021/acs.jpcc.1c01353 (cited on page 49).

[90] Etienne Christophe Socie. “Ultrafast Carrier and Quasiparticle Dynamics in Strongly Confined Perovskite Nanoplatelets.” PhD thesis. EPFL, 2022. DOI: 10.5075/epfl-thesis-9826 (cited on page 49).

[91] Clara Otero-Martínez, Nadesh Fiuza-Maneiro, and Lakshminarayana Polavarapu. “Enhancing the Intrinsic and Extrinsic Stability of Halide Perovskite Nanocrystals for Efficient and Durable Optoelectronics.” In: *ACS Applied Materials & Interfaces* 14.30 (2022), pp. 34291–34302. DOI: 10.1021/acsami.2c01822 (cited on pages 50, 78).

[92] Ji Li, Li Wang, Xi Yuan, Baoxue Bo, Haibo Li, Jialong Zhao, and Xin Gao. “Ultraviolet Light Induced Degradation of Luminescence in $CsPbBr_3$ Perovskite Nanocrystals.” In: *Materials Research Bulletin* 102 (2018), pp. 86–91. DOI: 10.1016/j.materresbull.2018.02.021 (cited on page 50).

[93] Yue Wang, Xiaoming Li, Sivaramapanicker Sreejith, Fei Cao, Zeng Wang, Mihaiela Corina Stuparu, Haibo Zeng, and Handong Sun. “Photon Driven Transformation of Cesium Lead Halide Perovskites from Few-Monolayer Nanoplatelets to Bulk Phase.” In: *Advanced Materials* 28.48 (2016), pp. 10637–10643. DOI: 10.1002/adma.201604110 (cited on page 50).

[94] Yiming Zhao, Charl Riemersma, Francesca Pietra, Rolf Koole, Celso de Mello Donegá, and Andries Meijerink. “High-Temperature Luminescence Quenching of Colloidal Quantum Dots.” In: *ACS Nano* 6.10 (2012), pp. 9058–9067. DOI: 10.1021/nn303217q (cited on page 50).

[95] Xi Yuan, Xuemin Hou, Ji Li, Chaoqun Qu, Wenjin Zhang, Jialong Zhao, and Haibo Li. “Thermal Degradation of Luminescence in Inorganic Perovskite $CsPbBr_3$ Nanocrystals.” In: *Physical Chemistry Chemical Physics* 19.13 (2017), pp. 8934–8940. DOI: 10.1039/D1CP02119B (cited on page 50).

[96] Ke Xing, Sheng Cao, Xi Yuan, Ruosheng Zeng, Haibo Li, Bingsuo Zou, and Jialong Zhao. “Thermal and Photo Stability of All Inorganic Lead Halide Perovskite Nanocrystals.” In: *Physical Chemistry Chemical Physics* 23.32 (2021), pp. 17113–17128. DOI: 10.1039/D1CP02119B (cited on page 51).

[97] Franziska Krieg, Stefan T. Ochsenbein, Sergii Yakunin, Stephanie Ten Brinck, Philipp Aellen, Adrian Süess, Baptiste Clerc, Dominic Guggisberg, Olga Nazarenko, Yevhen Shynkarenko, Sudhir Kumar, Chih-Jen Shih, Ivan Infante, and Maksym V. Kovalenko. “Colloidal $CsPbX_3$ (X= Cl, Br, I) Nanocrystals 2.0: Zwitterionic Capping Ligands for Improved Durability and Stability.” In: *ACS Energy Letters* 3.3 (2018), pp. 641–646. DOI: 10.1021/acsenergylett.8b00035 (cited on page 51).

[98] Matthias Mader, Jakob Reichel, Theodor W. Hänsch, and David Hunger. “A Scanning Cavity Microscope.” In: *Nature Communications* 6.1 (2015), p. 7249. DOI: 10.1038/ncomms8249 (cited on pages 51, 53).

[99] Thomas Hümmer, Jonathan Noe, Matthias S. Hofmann, Theodor W. Hänsch, Alexander Högele, and David Hunger. “Cavity-Enhanced Raman Microscopy of Individual Carbon Nanotubes.” In: *Nature Communications* 7.1 (2016), p. 12155. DOI: 10.1038/ncomms12155 (cited on page 51).

[100] Florian Sigger, Ines Amersdorffer, Alexander Hötger, Manuel Nutz, Jonas Kiemle, Takashi Taniguchi, Kenji Watanabe, Michael Förg, Jonathan Noe, Jonathan J. Finley, Alexander Högele, Alexander W. Holleitner, Thomas Hümmer, David Hunger, and Christoph Kastl. “Ultra-Sensitive Extinction Measurements of Optically Active Defects in Monolayer MoS_2.” In: *Journal of Physical Chemistry Letters* 13.44 (2022), pp. 10291–10296. DOI: 10.1021/acs.jpclett.2c02386 (cited on page 51).

[101] Mark J. Fernée, Philippe Tamarat, and Brahim Lounis. “Spectroscopy of Single Nanocrystals.” In: *Chemical Society Reviews* 43.4 (2014), pp. 1311–1337. DOI: 10.1039/C3CS60209E (cited on page 52).

[102] Gabriele Rainò, Georgian Nedelcu, Loredana Protesescu, Maryna I. Bodnarchuk, Maksym V. Kovalenko, Rainer F. Mahrt, and Thilo Stöferle. “Single Cesium Lead Halide Perovskite Nanocrystals at Low Temperature: Fast Single-Photon Emission, Reduced Blinking, and Exciton Fine Structure.” In: *ACS Nano* 10.2 (2016), pp. 2485–2490. DOI: 10.1021/acsnano.5b07328 (cited on pages 52, 72).

[103] Craig F. Bohren and Donald R. Huffman. *Absorption and Scattering of Light by Small Particles.* John Wiley & Sons, 2008. DOI: 10.1002/9783527618156 (cited on pages 52, 53).

[104] Ursula Wurstbauer, Bastian Miller, Eric Parzinger, and Alexander W. Holleitner. “Light–Matter Interaction in Transition Metal Dichalcogenides and their Heterostructures.” In: *Journal of Physics D: Applied Physics* 50.17 (2017), p. 173001. DOI: 10.1088/1361-6463/aa5f81 (cited on page 53).

[105] Lukas Novotny and Bert Hecht. *Principles of Nano-Optics.* Cambridge University Press, 2012. DOI: 10.1017/CBO9780511813535 (cited on page 53).

[106] Thomas Hümmer. “Cavity-Enhanced Hyperspectral Raman and Absorption Microscopy.” PhD thesis. Ludwig-Maximilians-Universität München, July 2019. DOI: 10.5282/edoc.24669 (cited on page 53).

[107] Andreas Singldinger, Patrick Haußmann, Gauthier Debuisschert, Nina A. Henke, Jonathan Paul, Leo Luber, Patrick Ganswindt, Anna Abfalterer, and Alexander S. Urban. “Design Rules for Perovskite Nanocrystals: Volume-Governed Absorption Versus Shape-Controlled Auger Recombination.” In: *Advanced Optical Materials* (2025), p. 2501137. DOI: 10.1002/adom.202501137 (cited on page 55).

[108] Zhiya Dang, Javad Shamsi, Francisco Palazon, Muhammad Imran, Quinten A. Akkerman, Sungwook Park, Giovanni Bertoni, Mirko Prato, Rosaria Brescia, and Liberato Manna. “In Situ Transmission Electron Microscopy Study of Electron Beam-Induced Transformations in Colloidal Cesium Lead Halide Perovskite Nanocrystals.” In: *ACS Nano* 11.2 (2017), pp. 2124–2132. DOI: 10.1021/acsnano.6b08324 (cited on page 57).

[109] Xuanyu Chen and Zhiwei Wang. “Investigating Chemical and Structural Instabilities of Lead Halide Perovskite Induced by Electron Beam Irradiation.” In: *Micron* 116 (2019), pp. 73–79. DOI: 10.1016/j.micron.2018.09.010 (cited on page 57).

[110] Stefan Martin, Nina A. Henke, Carola Lampe, Markus Döblinger, Kilian Frank, Patrick Ganswindt, Bert Nickel, and Alexander S. Urban. “Fine-Tuning Blue-Emitting Halide Perovskite Nanocrystals.” In: *Advanced Optical Materials* 12.8 (2024), p. 2301009. DOI: 10.1002/adom.202301009 (cited on page 57).

[111] Junzhi Ye, Deepika Gaur, Chenjia Mi, Zijian Chen, Iago López Fernández, Haitao Zhao, Yitong Dong, Lakshminarayana Polavarapu, and Robert L.Z. Hoye. “Strongly-Confined Colloidal Lead-Halide Perovskite Quantum Dots: From Synthesis to Applications.” In: *Chemical Society Reviews* (2024). DOI: 10.1039/D4CS00077C (cited on page 57).

[112] Victor I. Klimov, Alexander A. Mikhailovsky, D.W. McBranch, Catherine A. Leatherdale, and Moungi G. Bawendi. “Quantization of Multiparticle Auger Rates in Semiconductor Quantum Dots.” In: *Science* 287.5455 (2000), pp. 1011–1013. DOI: 10.1126/science.287.5455.1011 (cited on pages 58, 66).

[113] Sascha Feldmann, Mahesh K. Gangishetty, Ivona Bravić, Timo Neumann, Bo Peng, Thomas Winkler, Richard H. Friend, Bartomeu Monserrat, Daniel N. Congreve, and Felix Deschler. “Charge Carrier Localization in Doped Perovskite Nanocrystals Enhances Radiative Recombination.” In: *Journal of the American Chemical Society* 143.23 (2021), pp. 8647–8653. DOI: 10.1021/jacs.1c01567 (cited on page 58).

[114] Moritz Gramlich, Bernhard J. Bohn, Yu Tong, Lakshminarayana Polavarapu, Jochen Feldmann, and Alexander S Urban. "Thickness-Dependence of Exciton–Exciton Annihilation in Halide Perovskite Nanoplatelets." In: *Journal of Physical Chemistry Letters* 11.13 (2020), pp. 5361–5366. DOI: 10.1021/acs.jpclett.0c01291 (cited on pages 58, 60, 61, 66).

[115] J. Puthenpurayil, O. H. Cheng, T. Qiao, D. Rossi, and D. H. Son. "On the Determination of Absorption Cross Section of Colloidal Lead Halide Perovskite Quantum Dots." In: *Journal of Chemical Physics* 151.15 (2019), p. 154706. DOI: 10.1063/1.5126039 (cited on pages 59, 60).

[116] S. L. G. Alvarez, C. B. Riel, M. Madani, M. Abdellah, Q. Zhao, X. Zou, T. Pullerits, and K. Zheng. "Morphology-Dependent One- and Two-Photon Absorption Properties in Blue Emitting $CsPbBr_3$ Nanocrystals." In: *Journal of Physical Chemistry Letters* 13.22 (2022), pp. 4897–4904. DOI: 10.1021/acs.jpclett.2c00710 (cited on page 60).

[117] F. Y. Zhang, Y. C. Liu, S. Q. Wei, J. S. Chen, Y. Zhou, R. X. He, T. Pullerits, and K. B. Zheng. "Microscopic Morphology Independence in Linear Absorption Cross-Section of $CsPbBr_3$ Nanocrystals." In: *Science China-Materials* 64.6 (2021), pp. 1418–1426. DOI: 10.1007/s40843-020-1555-1 (cited on page 60).

[118] C. A. Leatherdale, W. K. Woo, F. V. Mikulec, and M. G. Bawendi. "On the Absorption Cross Section of CdSe Nanocrystal Quantum Dots." In: *Journal of Physical Chemistry B* 106.31 (2002), pp. 7619–7622. DOI: 10.1021/jp025698c (cited on page 60).

[119] L. A. Padilha, J. T. Stewart, R. L. Sandberg, W. K. Bae, W. K. Koh, J. M. Pietryga, and V. I. Klimov. "Aspect Ratio Dependence of Auger Recombination and Carrier Multiplication in PbSe Nanorods." In: *Nano Letters* 13.3 (2013), pp. 1092–9. DOI: 10.1021/nl304426y (cited on page 60).

[120] J. A. Castaneda, G. Nagamine, E. Yassitepe, L. G. Bonato, O. Voznyy, S. Hoogland, A. F. Nogueira, E. H. Sargent, C. H. Cruz, and L. A. Padilha. "Efficient Biexciton Interaction in Perovskite Quantum Dots Under Weak and Strong Confinement." In: *ACS Nano* 10.9 (2016), pp. 8603–9. DOI: 10.1021/acsnano.6b03908 (cited on pages 60, 66).

[121] Thi Phuc Tan Nguyen, Steven A. Blundell, and Claude Guet. "One-photon Absorption by Inorganic Perovskite Nanocrystals: A Theoretical Study." In: *Physical Review B* 101.19 (2020), p. 195414. DOI: 10.1103/PhysRevB.101.195414 (cited on page 60).

[122] Verena A. Hintermayr, Lakshminarayana Polavarapu, Alexander S. Urban, and Jochen Feldmann. "Accelerated carrier relaxation through reduced coulomb screening in two-dimensional halide perovskite nanoplatelets." In: *ACS Nano* 12.10 (2018), pp. 10151–10158. DOI: 10.1021/acsnano.8b05029 (cited on page 62).

[123] N. Yarita, H. Tahara, T. Ihara, T. Kawawaki, R. Sato, M. Saruyama, T. Teranishi, and Y. Kanemitsu. "Dynamics of Charged Excitons and Biexcitons in $CsPbBr_3$ Perovskite Nanocrystals Revealed by Femtosecond Transient-Absorption and Single-Dot Luminescence Spectroscopy." In: *Journal of Physical Chemistry Letters* 8.7 (2017), pp. 1413–1418. DOI: 10.1021/acs.jpclett.7b00326 (cited on pages 63, 64).

[124] N. S. Makarov, S. Guo, O. Isaienko, W. Liu, I. Robel, and V. I. Klimov. "Spectral and Dynamical Properties of Single Excitons, Biexcitons, and Trions in Cesium-Lead-Halide Perovskite Quantum Dots." In: *Nano Letters* 16.4 (2016), pp. 2349–2362. DOI: 10.1021/acs.nanolett.5b05077 (cited on pages 65, 66).

[125] Janardhanakurup Aneesh, Abhishek Swarnkar, Vikash Kumar Ravi, Rituraj Sharma, Angshuman Nag, and K.V. Adarsh. "Ultrafast Exciton Dynamics in Colloidal $CsPbBr_3$ Perovskite Nanocrystals: Biexciton Effect and Auger Recombination." In: *Journal of Physical Chemistry C* 121.8 (2017), pp. 4734–4739. DOI: 10.1021/acs.jpcc.7b00762 (cited on page 65).

[126] E. H. Oriel, D. N. Dirin, K. Shcherbak, M. I. Bodnarchuk, M. V. Kovalenko, L. X. Chen, and R. D. Schaller. "Intraband Cooling and Auger Recombination in Weakly to Strongly Quantum-Confined $CsPbBr_3$ Perovskite Nanocrystals." In: *Journal of Physical Chemistry Letters* (2024), pp. 6062–6068. DOI: 10.1021/acs.jpclett.4c00941 (cited on page 65).

[127] Richard D. Schaller and Victor I. Klimov. "High Efficiency Carrier Multiplication in PbSe Nanocrystals: Implications for Solar Energy Conversion." In: *Physical Review Letters* 92.18 (2004), p. 186601. DOI: 10.1103/PhysRevLett.92.186601 (cited on page 66).

[128] Anshu Pandey and Philippe Guyot-Sionnest. "Multicarrier Recombination in Colloidal Quantum Dots." In: *Journal of Chemical Physics* 127.11 (Sept. 2007), p. 111104. DOI: 10.1063/1.2786068 (cited on page 66).

[129] I. Robel, R. Gresback, U. Kortshagen, R. D. Schaller, and V. I. Klimov. "Universal Size-Dependent Trend in Auger Recombination in Direct-Gap and Indirect-Gap Semiconductor Nanocrystals." In: *Physical Review Letters* 102.17 (2009), p. 177404. DOI: 10.1103/PhysRevLett.102.177404 (cited on page 66).

[130] Yulu Li, Tao Ding, Xiao Luo, Zongwei Chen, Xue Liu, Xin Lu, and Kaifeng Wu. "Biexciton Auger Recombination in Mono-Dispersed, Quantum-Confined $CsPbBr_3$ Perovskite Nanocrystals Obeys Universal Volume-Scaling." In: *Nano Research* 12.3 (2018), pp. 619–623. DOI: 10.1007/s12274-018-2266-7 (cited on page 66).

[131] Yulu Li, Xiao Luo, Tao Ding, Xin Lu, and Kaifeng Wu. "Size-and Halide-Dependent Auger Recombination in Lead Halide Perovskite Nanocrystals." In: *Angewandte Chemie* 132.34 (2020), pp. 14398–14401. DOI: 10.1002/ange.202004668 (cited on page 66).

[132] Q. Li and T. Lian. "Area- and Thickness-Dependent Biexciton Auger Recombination in Colloidal CdSe Nanoplatelets: Breaking the Universal Volume Scaling Law." In: *Nano Letters* 17.5 (2017), pp. 3152–3158. DOI: 10.1021/acs.nanolett.7b00587 (cited on page 66).

[133] Q. Li, Y. Yang, W. Que, and T. Lian. “Size- and Morphology-Dependent Auger Recombination in $CsPbBr_3$ Perovskite Two-Dimensional Nanoplatelets and One-Dimensional Nanorods.” In: *Nano Letters* 19.8 (2019), pp. 5620–5627. DOI: 10.1021/acs.nanolett.9b02145 (cited on page 66).

[134] Chunxing She, Igor Fedin, Dmitriy S. Dolzhnikov, Peter D. Dahlberg, Gregory S. Engel, Richard D. Schaller, and Dmitri V. Talapin. “Red, Yellow, Green, and Blue Amplified Spontaneous Emission and Lasing Using Colloidal CdSe Nanoplatelets.” In: *ACS Nano* 9.10 (2015), pp. 9475–9485. DOI: 10.1021/acsnano.5b02509 (cited on page 67).

[135] John P. Philbin, Alexandra Brumberg, Benjamin T. Diroll, Wooje Cho, Dmitri V. Talapin, Richard D. Schaller, and Eran Rabani. “Area and Thickness Dependence of Auger Recombination in Nanoplatelets.” In: *Journal of Chemical Physics* 153.5 (2020). DOI: 10.1063/5.0012973 (cited on page 67).

[136] Hendrik Utzat, Weiwei Sun, Alexander E.K. Kaplan, Franziska Krieg, Matthias Ginterseder, Boris Spokoyny, Nathan D. Klein, Katherine E. Shulenberger, Collin F. Perkinson, Maksym V. Kovalenko, and Moungi G. Bawendi. “Coherent Single-Photon Emission from Colloidal Lead Halide Perovskite Quantum Dots.” In: *Science* 363.6431 (2019), pp. 1068–1072. DOI: 10.1126/science.aau7392 (cited on page 72).

[137] Michèle G. Greiner, Andreas Singldinger, Nina A. Henke, Carola Lampe, Ulrich Leo, Moritz Gramlich, and Alexander S. Urban. “Energy Transfer in Stability-Optimized Perovskite Nanocrystals.” In: *Nano Letters* 22.16 (2022), pp. 6709–6715. DOI: 10.1021/acs.nanolett.2c02108 (cited on page 83).

[138] Michal Baranowski and Paulina Plochocka. “Excitons in Metal-Halide Perovskites.” In: *Advanced Energy Materials* 10.26 (2020), p. 1903659. DOI: 10.1002/aenm.201903659 (cited on page 85).

The author acknowledges the use of large language models to improve spelling, grammatical correctness, and clarity. The use was strictly limited to text editing, and no data analysis or interpretation was performed using these tools.

List of Figures

List of Tables

List of Abbreviations

A:D	Acceptor to Donor Ratio
API	Application Programming Interfaces
CB	Conduction Band
CBM	Conduction Band Minimum
CEES	Cavity-Enhanced Extinction Spectroscopy
CCD	Charge-Coupled Device
CMC	Critical Micelle Concentration
DBR	Distributed Bragg Reflector
DFT	Density Functional Theory
DOS	Density of States
FA	Formamidinium
FFT	Fast Fourier Transform
FLUPS	Fluorescence Upconversion Spectroscopy
FRET	Förster Resonance Energy Transfer
FWHM	Full-Width at Half-Maximum
HE	Heavy Electrons
HR-TEM	High-Resolution Transmission Electron Microscopy
LARP	Ligand Assisted Reprecipitation
LCD	Least Confined Dimension
LE	Light Electrons
LP	Longpass
MA	Methylammonium
ML	Monolayer
OA	Oleic Acid
OD	Optical Density
ODE	Octadecene
OLA	Oleylamine
OKG	Optical Kerr-Gating
OPA	Optical Parametric Amplifier
OPA	One-Photon Absorption
OSC	Oscillator
PCF	Photonic Crystal Fiber
PL	Photoluminescence
PLQY	Photoluminescence Quantum Yield
PS	Polystyrene
P2VP	Poly(2-Vinylpyridine)
RT	Room Temperature
SHG	Second Harmonic Generation
SHI	Second Harmonic Idler
SHS	Second Harmonic Signal
SO	Split-Off
SPAD	Single-Photon Avalanche Diode
SEM	Scanning Electron Microscopy
S-C	Stretcher-Compressor
TAS	Transient Absorption Spectroscopy
TCSPC	Time-Correlated Single Photon Counting
TEM	Transmission Electron Microscopy
TRPL	Time-Resolved Photoluminescence

UV	Ultraviolet
VB	Valence Band
VBM	Valence Band Maximum
VIS	Visible (spectrum/region)
WLG	White Light Generation

Acknowledgments

This work would not have been possible without the support, encouragement, and kindness of many people along the way.

First of all, **Alexander Urban**, it's hard to believe it's been over seven years since I was in your optoelectronics lecture back in the 'Mathebau'. And I am genuinely so happy that your open and incredibly kind way of teaching motivated me to ask you for a master thesis in your group. After a short walk to Amalienstraße, I was also convinced by the ideas and topics of your research. In those early days, the group was still new and small, and being there felt more like hanging out with friends than actually working. Thanks to your thoughtful selection of people, you've managed to keep that wonderful atmosphere alive to this day. I honestly can't thank you enough for giving me the chance to join your group and for offering me a PhD position after I completed my master thesis. And now, this chapter also comes to an end. My time in your group has had a really positive impact on my life, and I will always remember it with a big smile. Thank you for everything, and let us definitely stay in touch. I'm excited to see what you'll build in the future. I might be your longest running team member so far. Let's see if anyone can beat that.

As one of the first members of the Nanospectroscopy group, I had the chance to grow with it from the very beginning. I'm incredibly grateful to **Moritz Gramlich** and **Carola Lampe**, who helped me so much in the early days when I had no idea what I was doing. I still remember how Moritz and I achieved the first successful TCSPC measurement with the group's very first optical setup. At the time, this was a real eureka moment. Now, in the new building, it's one of the most routine measurements to perform. Caro introduced Good Food Friday as a way to escape the Mensa now and then, and even though I'm a Mensa fan and always will be, I enjoyed getting, for example, Vietnamese food. **Michael Lichtenegger** and **Ulrich Leo** started their PhDs a few months before me and **Nina Henke** joined around a year later as a PhD. Michi, you always had a good joke up your sleeve, and even in the final weeks of your PhD, your paper pipeline was full to the brim. The "Schreib mer zam" spirit still sticks with me today. With Nina, I finally found someone who whistles earworms just as often as I do and who is also a fellow Potterhead. And whenever I had any problem in the chemistry lab, I learned from you that "abzentrifugieren" always helps. You should definitely include that in your perovskite cookbook! Without Ulrich, there would never have been a group LAN party, and he was always ready for some 3D printing action. I'm happy that some of our hobbies also overlap outside of the institute. **Patrick Ganswindt** was the next PhD student who joined the group. After a short settling-in period, you quickly became someone the office just wouldn't be the same without. I still don't know how you managed to create memes within seconds that perfectly capture the situation. And it was great to have someone who could make the daily struggles of thesis writing and PhD life genuinely funny. Your humor is really one of a kind. I would definitely enjoy being colleagues with you again someday, whether in Hellabrunn or at Jeol. When **Anna Abfalterer** joined the group as a postdoc, she immediately brightened up the office with her friendly and funny nature and her random questions like, "Can you tell me how many different words there are in Abfalterer?". Maybe one day we'll meet again for a Jause and an Amaretto Spritz. I know how much you're carrying on your shoulders. PhDs are finishing and the laser lab is full of amazing setups waiting for your attention. But knowing you, I honestly can't think of anyone better suited to handle that. I wish all of you the best in the future.

A special thank you also goes to **Jan Drewniok**, **Andreas Bornschlegl**, and **Stefan Martin**. I'm still happy every single time I meet with you, and we laugh about the 'golden days' at the institute. I wouldn't know where I would have gotten food from if it hadn't been for Drewnioks Delivery Service™, and I am looking forward to being beaten by you again at go-karting and countless more discussions about Formula 1. And Borni, I will never forget that day in December when "The Day After Tomorrow" hit Munich, and we prepared to stay the weekend at the institute and went bouldering afterward. Perhaps we can repeat this in the future, but let's keep it to just bouldering. Stefan, I always

appreciated your kind and funny nature, the walks to the Mensa, where you introduced me to the world of One Piece, and our bouldering sessions. I wish the three of you all the best and continued success with your PhDs.

I would also like to thank all the students who contributed to my work, as well as those I had the privilege to supervise over the years. Without you, my research wouldn't be what it is. Thank you to **Michèle Greiner**, **Patrick Haußmann**, **Daphne Benedikt**, **Kilian Steiniger**, **Michael Seilbeck**, **Youlin Zhang**, **Gauthier Debuisschert**, **Matthias Okur**, **Christoph Gruber**, **Jonathan Paul**, and **Leo Luber**. And of course, all the other members of the Nanospec group helped shape it into what it was: a friendly, open team of amazing people where you could always count on help. So thank you to everyone who has been part of the group over the years.

Furthermore, I want to thank the Qlibri team for the great collaboration: **Thomas Hümmer**, **Jonathan Noé** and especially **Ines Amersdorffer**. Even though our research project faced many problems and challenges, I think we made a great team. Ines, I wish you all the best for the rest of your PhD and thank you again for the Gummibaum. It is still thriving on the window sill.

Matthias Kestler also deserves my special thanks. He followed my steps and decided to start both a master thesis and a PhD at the Nano Institute. We've been friends from our very first semester at LMU and it was always great to grab a coffee and discuss deep physics, stocks, or whatever else came up. Thank you, and good luck with the rest of your PhD!

And last but certainly not least, I would like to thank my family. My parents, **Ingrid** and **Paul** who have always supported me, been there for me, and given me the courage and confidence to take this step and accomplish everything that came with it. My sister **Barbara**, who was always there with an open ear, gave me advice and helped me, especially with all sorts of difficult life decisions. And I want to thank **Christine**, the most important person in my life. You have supported me every single day, whether it was related to my work or to any other problem I faced. Without your support, I probably wouldn't have made it this far.